

Medizinische Fakultät  
der  
Universität Duisburg-Essen

Aus der Abteilung für Hochfeld- und Hybride MR-Bildgebung

**Development and evaluation of new methods  
to improve attenuation correction  
in PET/MR hybrid imaging**

Inaugural – Dissertation  
zur  
Erlangung des Doktorgrades  
der Naturwissenschaften in der Medizin  
durch die Medizinische Fakultät  
der Universität Duisburg-Essen

Vorgelegt von  
**Mark Oehmigen**  
aus Greifswald

2019

Diese Dissertation wird über DuEPublico, dem Dokumenten- und Publikationsserver der Universität Duisburg-Essen, zur Verfügung gestellt und liegt auch als Print-Version vor.

**DOI:** 10.17185/duepublico/71796

**URN:** urn:nbn:de:hbz:464-20200618-133824-1

Alle Rechte vorbehalten.

Dekan: Herr Univ.-Prof. Dr. med. J. Buer  
1. Gutachter: Herr Univ.-Prof. Dr. rer. medic. Dipl.-ing. H. H. Quick  
2. Gutachter: Herr Univ.-Prof. Dr. med. Ch. Rischpler

Tag der mündlichen Prüfung: 07. Mai 2020

## List of publications

Publications which are part of this thesis:

1. **Oehmigen M**, Lindemann ME, Gratz M, Kirchner J, Ruhlmann V, Umutlu L, Blumhagen JO, Fenchel M, Quick HH.  
“Impact of improved attenuation correction featuring a bone atlas and truncation correction on PET quantification in whole-body PET/MR.”  
Published in: Eur J Nucl Med Mol Imaging. 2018 Apr;45(4):642-653 (Impact Factor 7.28).
2. **Oehmigen M**, Lindemann ME, Gratz M, Neji R, Hammers A, Sauer M, Lanz T, Quick HH.  
“A dual-tuned  $^{13}\text{C}/\ ^1\text{H}$  head coil for PET/MR hybrid neuroimaging: Development, attenuation correction, and first evaluation.”  
Published in: Med Phys. 2018 Nov;45(11):4877-4887 (Impact Factor 2.61).
3. **Oehmigen M**, Lindemann ME, Lanz T, Kinner S, Quick HH.  
“Integrated PET/MR breast cancer imaging: Attenuation correction and implementation of a 16-channel RF coil.”  
Published in: Med Phys. 2016 Aug;43(8), 4808- 4820 (Impact Factor 2.61).

<b>Table of content</b>	
List of publications	<b>3</b>
<b>Zusammenfassung der Doktorarbeit</b>	<b>5</b>
<b>Abstract of the dissertation</b>	<b>8</b>
<b>Background</b>	<b>10</b>
Basics of positron emission tomography	10
Hybrid imaging	12
Attenuation correction	14
Hardware attenuation correction in PET/MR	15
<b>Aims of the Thesis</b>	<b>18</b>
Aims of the thesis	18
<b>Introduction</b>	<b>20</b>
Introduction Study 1	20
Introduction Study 2	22
Introduction Study 3	24
<b>Materials and Methods</b>	<b>27</b>
Material and Methods Study 1	27
Materials and Methods Study 2	35
Materials and Methods Study 3	43
<b>Results</b>	<b>51</b>
Results Study 1	51
Results Study 2	56
Results Study 3	61
<b>Discussion and Conclusion</b>	<b>69</b>
Discussion and Conclusion Study 1	69
Discussion and Conclusion Study 2	72
Discussion and Conclusion Study 3	75
<b>Summary</b>	<b>80</b>
<b>Zusammenfassung</b>	<b>81</b>
References	82
List of abbreviation	88
Acknowledgments	89
Curriculum Vitae	90

# Zusammenfassung der Doktorarbeit

## Hintergrund und Ziele

Die kombinierte Positron-Emissions-Tomographie (PET) und Magnetresonanztomographie (MRT), kurz PET/MR-Hybridbildgebung, vereint synergistisch die Vorteile beider bildgebenden Modalitäten. Die MRT bietet exzellenten Weichteilkontrast, die exakte Darstellung von kleinsten Gewebestrukturen und Gefäßen und eine hohe räumliche Auflösung und dies gänzlich ohne Strahlenbelastung. Mit der PET lassen sich kleinste Mengen eines radioaktiven Tracers im Körper detektieren und damit Karzinome, Raumforderungen und entzündlichen Strukturen nachweisen und lokalisieren. Mit der PET/MR-Hybridbildgebung lassen sich also in einer Untersuchung kombinierte Bildgebungsinformationen über die Anatomie (MRT) und den dazu gehörigen Stoffwechsel (PET) gewinnen.

Eine grundlegende physikalisch/technische Herausforderung bei der PET/MR- und bei der PET/Computertomographie (PET/CT) -Hybridbildgebung ist die Abschwächung der PET-signalgebenden Photonen auf dem Weg aus dem Patientenkörper hin zu den PET-Detektoren. Diese Photonen werden durch menschliches Gewebe aber auch durch technische Bauteile (z.B. MRT Hochfrequenz (HF) Empfangsspulen) geschwächt. Um den Signalverlust durch Photonenschwächung zu korrigieren muss in der PET-Bildgebung eine Schwächungskorrektur (attenuation correction, AC) erfolgen, damit die Aktivitätsverteilung im Körper korrekt errechnet, abgebildet und quantifiziert werden kann.

In der PET/CT erfolgt die AC durch Umrechnung der vorliegenden CT-Daten. In der PET/MR liegen jedoch keine CT-Daten vor; daher muss die AC der Patientengewebe hier basierend auf MRT-Daten erfolgen. Hierzu existieren heute etablierte Methoden zur MR-basierten AC von Patientengewebe. Die AC von HF-Spulen und Hardwarekomponenten kann jedoch nicht MR-basiert erfolgen, da in der MRT-Bildgebung Strukturen aus Kunststoffen und Metallen nicht detektierbar sind. Zur AC von HF-Spulen und Hardwarekomponenten in der PET/MR werden zunächst CT-basierte 3-dimensionale (3D) Datensätze (Templates) dieser Bauteile angefertigt. Diese können dann von den CT-Schwächungswerten zu PET-Schwächungswerten umgerechnet werden und als virtuelle Platzhalter während der Rekonstruktion der PET-Daten zur AC herangezogen werden.

Das Ziel dieser Arbeit war es, neue Methoden der Schwächungskorrektur für verschiedene klinische Anwendungen in der PET/MR-Hybridbildgebung zu entwickeln und

für ihren Einsatz in der klinischen Diagnostik zu evaluieren. Hierzu wurden insgesamt drei Studien durchgeführt, die sich mit der Verbesserung der AC von Patientengeweben, mit der AC einer neuen HF-Kopfspule sowie mit der AC einer neuen HF-Brustspule befassen.

## **Material und Methoden**

Im ersten Teil der Arbeit wurde eine neue Version der MR-basierten Schwächungskorrektur von Patientengeweben in einer retrospektiven Studie an n= 50 Patienten systematisch evaluiert. Im Gegensatz zu den bisher etablierten Methoden zur MR-basierten AC liefert die neue Version zusätzlich eine modellbasierte Knochendetektion, sowie eine Erweiterung des Bildfeldes (HUGE Methode), welches ansonsten in der MRT-Bildgebung limitiert ist und daher zu einer fehlerhaften AC im Bereich der Arme des Patienten führen kann.

In der zweiten Studie wurde eine Zwei-Kern-HF-Kopfspule für die C<sup>13</sup>- und H<sup>1</sup>-Neurobildgebung untersucht und in die PET/MR-Hybridbildgebung integriert. Hierzu wurde ein CT-basiertes 3D AC-Modell für die HF-Kopfspule erstellt. Mithilfe von Phantomexperimenten und einer Patientenstudie wurden die HF-Kopfspule und das AC-Modell evaluiert.

In der dritten Studie wurde eine 16-Kanal HF-Brustspule für die PET/MR-Hybridbildgebung optimiert und ebenfalls mit einem geeigneten CT-basierten 3D AC-Modell in die PET/MR-Hybridbildgebung integriert. Die Funktionalität der optimierten HF-Brustspule wurde mithilfe von Phantomen und in einer Patientenstudie evaluiert.

## **Ergebnisse**

In der Patientenstudie an n= 50 Patienten wurden insgesamt 99 Läsionen detektiert und deren Aktivität bestimmt (standardized uptake value, SUV). Durch die Verwendung der neuen AC-Methode stieg der gemessene durchschnittliche SUV-Wert gemittelt über alle 99 Läsionen um 4,4 % an. Für knochen nahe Tumore und Läsionen konnte ein Anstieg des SUV-Wertes von bis zu 35 % gemessen werden.

In der zweiten Studie zeigte die neue HF-Kopfspule in Phantommessungen eine globale mittlere Schwächung der PET Signale von 9 % und lokale Schwächung von 1 % bis 25 %. Das angefertigte CT-basierte 3D AC-Modell konnte die globale mittlere Schwächung auf 0,5 % senken. Die erfolgreiche Durchführung der Schwächungskorrektur konnte ebenfalls in der zugehörigen Patientenstudie demonstriert werden.

In der dritten Studie wurde für die neue 16-Kanal HF-Brustspule in Phantommessungen ein durchschnittlicher PET-Signalverlust um 13 % festgestellt. Lokale Schwächungen reichten von 0 % bis zu 24 % Signalverlust. Die Hardware-Schwächungskorrektur mithilfe des angefertigten CT-basierten 3D AC-Modells konnte die

mittlere Schwächung auf 0,5 % senken. Die erfolgreiche Durchführung der Schwächungskorrektur konnte hier ebenfalls in der Patientenstudie demonstriert werden.

## **Schlussfolgerung**

Die entwickelten und evaluierten Methoden dieser Arbeit dienen jeweils der Verbesserung der Schwächungskorrektur und damit der Erweiterung des Einsatzspektrums der PET/MR-Hybridbildgebung. Die Erweiterung der MR-basierten Schwächungskorrektur um die atlasbasierte Knochendetektion und um eine Verzeichniskorrektur (HUGE-Methode) wurde klinisch validiert. Eine neu entwickelte HF-Kopfspule und eine neu entwickelte HF-Brustspule wurden mittels CT-basierter 3D AC-Modelle erfolgreich in die PET/MR-Hybridbildgebung integriert und sind nun beide als neue Produktpulen kommerziell erhältlich.

# Abstract of the dissertation

## **Background and Aims**

Combined positron-emission-tomography (PET) and magnet resonance (MR) imaging, called PET/MR hybrid imaging, conjuncts the advantages of both imaging modalities. While MR provides excellent soft tissue contrast, exact depicting of smallest tissue structures and vessels, as well as a high spatial resolution, without applying any radiation exposure, PET can detect smallest amounts of radioactive tracers in the human body and with that detect and localize carcinoma, lesions and inflammatory processes. With PET/MR hybrid imaging image information about anatomy (MR) and according metabolism (PET) can be acquired simultaneously.

A basic physical/technical challenge for hybrid PET/MR and PET/computed tomography (PET/CT) is the attenuation of PET photons on their way from tracer accumulation in within the patient body to the PET detectors located outside. Photons are attenuated by human tissues and by technical hardware components (e.g. MR radiofrequency (RF) coils). To compensate the signal loss of the attenuated photons in PET imaging, an attenuation correction (AC) must be performed, to calculate, depict and quantify the tracer activity distribution in the patient correctly.

For PET/CT AC is performed by an established conversion of the acquired CT transmission data. For PET/MR, however, no CT data exist, therefore, AC of patient tissues must be performed on basis of MR data. For this purpose, several methods for MR-based AC of patient tissue have been established. However, AC of RF coils and hardware components in PET/MR cannot be performed on basis of the MR data, because polymers and metals are not detectable with MR imaging. For AC of RF coils and hardware components in PET/MR, CT-based three-dimensional (3D) templates of the components are generated. The CT attenuation coefficients are then converted to PET attenuation coefficients and serve as virtual 3D maps for AC during reconstruction of PET data.

The aim of this thesis was to develop new attenuation correction methods for several clinical applications in PET/MR hybrid imaging and to evaluate their use in clinical diagnostics. Therefore, three studies were realized, which dealt with: 1. the improvement of patient tissue AC; 2. an AC for a new RF head coil, and 3. an AC for a new RF breast coil.

## Material and Methods

In the first part of the thesis a new version of MR-based attenuation correction for patient tissue was systematically evaluated in a retrospective study with  $n=50$  patients. In contrast to the established methods for MR-based AC, the new AC version adds model-based bone detection and an extension of field of view (HUGE method), which otherwise is limited in MR imaging and, thus, leads to truncation and incorrect AC of the patient arms.

In the second study, a dual-tuned RF head coil for  $C^{13}$ - and  $H^1$ - neuroimaging was examined and integrated in PET/MR hybrid imaging. Therefore, a CT-based 3D AC template of the RF head coil was generated. With phantom experiments and a patient study, the RF head coil and the AC template were evaluated.

The third study dealt with the optimization of a 16-channel RF breast coil for PET/MR hybrid imaging and the integration of a suitable CT-based 3D AC template. The functionality of the optimized RF breast coil was evaluated with phantoms and a patient study.

## Results

For the patient study with  $n=50$  patients, overall 99 lesions were detected and the standardized uptake values (SUV) were determined. When applying the new AC method, the measured mean SUV overall of 99 lesions increased by 4.4 %. Tumors and lesions near to bone structures experienced an increase of SUV up to 35 %.

In the second study, the new RF head coil causes a global mean PET signal attenuation of 9 % and a local attenuation between 1 % and 25 %. The generated CT-based 3D AC templates could decrease the global mean attenuation to 0.5 %. The successful attenuation correction could also be demonstrated with the dedicated patient study.

The third study showed a mean PET signal loss of 13 % for the new 16-channel RF breast coil in phantoms. Local attenuation ranged from 0 % up to 24 %. The hardware attenuation correction with the CT-based 3D AC template decreased the mean attenuation to 0.5 %. The successful applied attenuation correction was verified in a patient study.

## Conclusion

All developed and evaluated methods of this thesis improve attenuation correction and thereby enlarge the spectrum of clinical applications in PET/MR hybrid imaging. The expansion of MR-based attenuation correction with additional atlas-based bone detection and the truncation correction (HUGE method) were clinically validated. A newly developed RF head coil and RF breast coil were both successfully integrated into PET/MR hybrid imaging by using CT-based 3D AC templates.

# Background

By combining diagnostic imaging modalities with molecular imaging systems, multiple advantages from both systems come in to play for diagnosis. The development goes from standalone positron emission tomography (PET) systems, over a combination with computed tomography (CT) resulting in PET/CT [Beyer et al. 2000], or magnetic resonance (MR) imaging leading to PET/MR imaging [Quick et al. 2011].

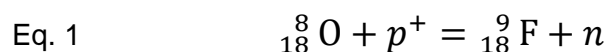
## Basics of positron emission tomography

Introduced in the 1970s for cardiac, neurological and oncological imaging, PET shows its advantages in metabolism and functional imaging.

Positron emission tomography for diagnosis mainly depicts physiological processes and biochemical reactions in the human body. The positron is the antiparticle of the electron, with the same mass, but with a positive electrical charge and is displayed with  $\beta^+$  [Mayer-Kuckuk T. 1994].

When proton rich nuclides decay ( $\beta^+$  decay), a proton is converted into a neutron, a positron and an electron neutrino. Although the mass of the element is unaffected, the nuclear charge number is decreased, so the proton rich element decays to its predecessor in the periodic system.

An example for a radiopharmaceutical frequently used for PET is  $^{18}\text{F}$  Fluor ( $^{18}\text{F}$ ). Natural Fluor  $_{19}^9\text{F}$  has 9 protons and 10 neutrons and is stable, with no radioactive decay. To synthesize radioactive Fluor, heavy oxygen isotopes  $_{18}^8\text{O}$  with 8 protons and 10 neutrons are used. A cyclotron accelerates protons with 15 MeV and targets the heavy oxygen isotope (Equation 1).



As a result, radioactive  $^{18}\text{F}$  Fluor is produced, and a neutron which is captured inside the cyclotron. The half life time of  $^{18}\text{F}$  Fluor is 109.8 minutes [Phelps et al. 2004]

When the  $^{18}\text{F}$   $\beta^+$  decays, it will convert back into oxygen isotope. The emitted positron  $\beta^+$  travels through matter (patient, air, phantoms, water, etc.) and will be annihilated by any electron. The “travel distance” of the positron can be up to several millimeters, which

later leads to a blurring of the images, because the emission and annihilation location do not match exactly. When the positron  $\beta^+$  and electron  $\beta^-$  “meet” and annihilate each other, the mass of both particles is converted into energy and two photons are emitted. If the kinetic energy of  $\beta^+$  is negligible, the angle of the both photons will be  $180^\circ$  (with a variation in the kinetic energy, the angle will vary a little) [Hendee et al. 2002]. The energy of the photons is 511 keV each. This can be calculated by using the theory of relativity (Equation 2).

$$\text{Eq. 2} \quad E = m c^2$$

$m = \text{mass of electron and positron (each } 9.1 \cdot 10^{-31} \text{ kg)}$

$c = \text{speed of light } 3 \cdot 10^8 \text{ m/s}$

$$E = 2 * 9.1 \cdot 10^{-31} \text{ kg} \times (3 \cdot 10^8 \text{ m/s})^2$$

$$E = 1.638 \cdot 10^{-13} \frac{\text{m}^2}{\text{s}^2} \text{ kg}$$

$$E = 1.638 \cdot 10^{-13} \text{ Nm}$$

$$E = 1.638 \cdot 10^{-13} \text{ J}$$

Converting joule into elektrovolt:

$1,602 \cdot 10^{-19} \text{ J}$  corresponds to 1 eV

$$1,638 \cdot 10^{-13} \text{ J} \div 1,602 \cdot 10^{-19} \text{ J} = 1,022,472 \text{ eV}$$

The total energy of 1.02 MeV is split into 2 photons

$$1,022,472 \text{ eV} \div 2 \approx 511,235 \text{ eV} \approx \mathbf{511 \text{ keV}}$$

To use radioactive  $^{18}\text{F}$  as a tracer in the human body, it must be attached to biological molecules, resulting in a radiopharmaceutical.  $^{18}\text{F}$  is attached to glucoses by several synthesizing steps; the direct bombardment in the cyclotron would destroy the glucoses.

$^{18}\text{F}$  replaces a hydroxyl group in the glucose, leading from normal  $\text{C}_6\text{H}_{12}\text{O}_6$  to radioactively marked glucose  $\text{C}_6\text{H}_{11}\text{FO}_5$ . The marked fluorodeoxyglucose ( $^{18}\text{F}$ -FDG) can be injected intravenous into the patient and is distributed by the blood stream. Body regions with a higher physiological demand of glucoses, like the heart and brain [Buck et al. 2004], and regions with a pathological consumption such as tumors and metastases will have a higher concentration of  $^{18}\text{F}$ -FDG [Cairns et al. 2011]. Other regions; which also accumulated the radiotracer; are the kidneys, urethra and the bladder.

Inside the cells,  $^{18}\text{F}$ -FDG is phosphorylated by the enzyme hexokinase into FDG-6-phosphat. Unlike Glucose-6-phosphat, it cannot be metabolized anymore, due to the varying structure. This results in an even higher concentration (metabolic trapping) in the specific body region. Unless  $^{18}\text{F}$  is transformed to oxygen by the  $\beta^+$  decay, the glucose with the heavy oxygen isotope can be metabolized in the citric acid cycle. The emitted positron  $\beta^+$  is annihilated by surrounding electrons  $\beta^-$ , leading then to two opposite emitted annihilation photons (or  $\gamma$ -rays each with 511 keV energy).

To obtain image information from the two  $180^\circ$  annihilation photons, PET detectors for the energy level of 511 keV are built in a ring structure around the patient [Kuwert et al. 2008]. The patient is lying inside the gantry; positron  $\beta^+$  emission inside the human cells causes annihilation photons, which are then detected by two opposing PET detectors. The detectors consist of scintillators and photomultiplier tubes (PMT), which are able to detect single photons and create a signal for further image processing. Under the conditions, that the photons always appear double-paired and in a  $180^\circ$  angle; if a PMT detects a photon, a narrow enough chosen time window (several nanoseconds) ensures, that the next event detected (coincidence) is probably the corresponding annihilation photon. The list of PET detectors, which detected an event and at which time, is saved in a data file called *list mode* which is the bases for PET raw data. The line on which the photons travelled, and which virtually connects the two PET detectors is called coincidence line or *line-of-response* (LOR). The positive detection of the photons is called a *true event*. Also, *random* and *scatter* events occur and can be detected and lead to noise in the reconstructed PET image. The random and scatter events in PET images must be corrected, using special correction methods. The sum of the LOR will form the sinogram data file, which is processed and reconstructed into PET images. Simply put, the more coincidence lines cross each other in a certain part of the body, the more likely  $\beta^+$  emission comes from this region, which is a sign for locally increased glucose consumption.

## Hybrid imaging

With the introduction of the first clinical PET/CT by Townsend et al. [Beyer et al. 2000], patient examinations could be acquired by two diagnostic imaging modalities simultaneously. Hybrid imaging with PET/CT combines two imaging modalities. PET detects and visualizes metabolic information and pathologic processes by accumulation of a specific radiotracer in the tissue. By combining PET data acquisition with the high spatial resolution of CT imaging, PET/CT hybrid imaging provides synergies that supersede stand-alone PET system.

Compared to PET/CT hybrid imaging, the combination of PET and MR was technically more challenging since the strong static and time-varying magnetic fields, which are used for MR imaging, may influence PET components and detectors. MR imaging uses a strong static magnetic field  $B_0$ , local magnetic fields (gradients) and the principle of relaxations of spins for image formation [Haacke et al. 1999]. Some initial approaches to PET/MR hybrid imaging separated an MR and a PET/CT system in two different rooms, while the patient rests on the same patient table (GE Healthcare) [Veit-Haibach et al. 2013]. Another initial approach is a rotating patient table and a PET and MR facing each other at a distance of about 3 m (Philips Healthcare) [Zaidi et al. 2011]. In these first two approaches, the patient transfer between the two modalities leads to a sequential scan, with an inherent delay of several minutes, increasing the potential for patient motion between scans and also increasing overall examination times. The first integrated whole-body PET/MR system, which simultaneously and independently could acquire PET and MR data, was announced and introduced in year 2010 [Delso et al. 2011] (Biograph mMR, Siemens Healthcare GmbH, Erlangen, Germany) and was first installed in the Institute of Medical Physics (IMP), Erlangen in the year 2010 [Quick et al. 2011; Quick 2014].

There are several technical challenges to fit a PET detector ring into the 70 cm bore of a 3T MR system. By integrating the PET detector, the MR patient bore is further narrowed down in diameter. With a circumferential thickness of the PET detector ring of 5 cm, the PET/MR system features a remaining patient bore with 60 cm inner diameter.

The PMT and scintillators in conventional PET detectors emit radiofrequencies which can be shielded to minimize their disturbing influence on the RF coils of the MR system. This PET detector technique featuring conventional PMT detectors was used in hybrid systems which scan MR and PET in sequential mode as described above [Zaidi et al. 2011; Veit-Haibach et al. 2013]. However, for full integration of a PET detector ring into the isocenter of an MR system another challenge with PMT detectors comes into play. PMT detectors are using cascades of electrons to enhance signals; these do not work in the strong magnetic fields of an MR system. MR compatible alternatives for PMT were necessary for realization of an integrated PET/MR. Semi conductive detectors, e.g. avalanche photodiodes (APD), are compatible to high magnetic field strength and can detect single photons in an MR environment [Pichler et al. 2006]. APDs first have been used in animal scanners [Catana et al. 2006] and have then been used to design a prototype human brain PET/MR imaging insert [Schlemmer et al. 2008; Herzog et al. 2011].

## Attenuation correction

When annihilation photons are emitted from regions and lesions located in the human body, they travel through different body parts and tissues before they finally reach the PET detectors surrounding the patient. Thus, photons are proportionally absorbed by different patient tissues or scattered [Allisy-Roberts et al. 2008]. This ultimately leads to reduced PET signal, to decreasing image quality and to a bias in radiotracer quantification; the more photons are attenuated in human tissues. The PET signal loss is caused by the difference of emitted photons and detected photons. Images with no attenuation correction (NAC) must be corrected to attenuation corrected (AC) images to determine and compensate the loss of PET signal in every location of the patient. Photon attenuation is described by the Lambert-Beer's Law, which shows the relation of photon energy loss by travelling through material (Equation 3).

$$\text{Eq. 3} \quad I = I_{(0)}e^{-\mu\rho x}$$

$I_{(0)}$  = Initial photon intensity

$\mu$  = material absorption coefficient

$\rho$  = material density

$x$  = thickness of the material

The photon intensity decreases exponentially with the travel distance through specific material. Crucial for the attenuation correction is the linear attenuation coefficient (LAC) [ $\text{cm}^{-1}$ ] or also called  $\mu$ -values. The photons are influenced by the different  $\mu$ -values and the distance through the object [Kinahan et al. 2003]. Factors which come into play for calculating  $\mu$ -values are the initial photon energy, the density of the object and the atomic number of the material. To calculate the attenuation of the photons, by their path through the material, a three-dimensional map with  $\mu$ -values ( $\mu$ map) has to be generated, which depicts the attenuation of the photons on their path to the detector. Such 3D  $\mu$ maps contain LAC information for every object inside the PET field-of-view (FOV) and, therefore, the photon attenuation can be corrected.

To correct the photon attenuation in former stand-alone PET systems,  $^{68}\text{Ge}$  rod sources were used as a 511 keV transmission source, to gather attenuation information about the patient and material inside the PET field-of-view. The transmission data of the 511 keV energy sources was then used for attenuation correction and for improving the image quality of the PET data.

Since both modalities in PET/CT hybrid imaging are using photons for image acquisition (CT with an energy level range from 80-140 keV; PET with an energy level of 511 keV), the  $^{68}\text{Ge}$  rod sources for photon attenuation correction from former stand-alone PET systems were replaced by synergistically using the transmission data from the CT modality. Image data from the CT component can also be used and converted for photon attenuation in PET. Thus, CT imaging in PET/CT provides high spatial resolution anatomic imaging data and, additionally, transmission data for AC of PET data.

In modern PET/CT systems the CT data are used for generating  $\mu$ maps [Kinahan et al. 1998]. The attenuating data from the CT Hounsfield units (HU) are equivalent to spatial distribution of the LAC in the PET. The CT data given in HU with 140 keV energy level are converted using a bilinear conversion curve into 511 keV LAC PET energy level for attenuation correction [Carney et al. 2006; Paulus et al. 2013]. With this method, patient tissue and hardware materials and components can be attenuation corrected.

Beyond the above-mentioned challenges in hardware integration, attenuation correction in PET/MR hybrid imaging is a challenge on its own [Zaidi 2007; Beyer et al. 2008]. In contrast to PET/CT, where HU can be converted into LAC by a simple and straightforward mathematical operation, no CT data and thus HU information is available. Instead, the available MR data has to be used for attenuation correction; however, there is no physical correlation between the proton spin, which is the bases for MR signal and the PET LAC information. One approach for MR-based attenuation correction is MR-based signal segmentation and subsequent tissue classification. Here, a MR sequence separates fat and water images and an image segmentation algorithm divides the intensity values of the resulting MR images into four classes, background air, lung, fat and soft tissue. Each of the four classes has its own static LAC [Martinez-Möller et al. 2009]. This provides the basic human tissue  $\mu$ map. Other approaches to obtain a more precise human  $\mu$ map are CT-based atlas maps that also provide attenuation values for bone structures [Paulus et al. 2015], pattern recognition algorithms [Navalpakkam et al. 2013] or extending the MR FOV to provide a means for truncation correction [Blumhagen et al. 2013]. All these improvements aim towards generating more precise human  $\mu$ maps in PET/MR hybrid imaging.

## **Hardware attenuation correction in PET/MR**

Unlike PET/CT, where the photons are used for attenuation correction (patient tissues and hardware components), in PET/MR the MR data can only be used, to gather information for patient  $\mu$ maps. However, hardware components, like the patient table and radiofrequency coils also attenuate the annihilation photons. The attenuation of photons due to hardware

components and associated materials (electronic components, ceramics, metals, etc.) may be even higher than attenuation due to patient tissues. Nevertheless, such materials have a very low proton density and a very short T2\* relaxation time, which makes the hardware components nearly invisible for MR imaging. This means, that hardware components cannot be displayed in PET/MR imaging. Consequently, no data from the actual PET/MR scan can directly be used or segmented for hardware AC.

To correct for hardware components, the use of CT-based 3D templates of the respective hardware component was suggested [Delso et al. 2010; MacDonald et al. 2011; Tellmann et al. 2011; Paulus et al. 2012; Quick et al. 2013; Paulus et al. 2014; Paulus et al. 2016; Boellaard et al. 2015; Paulus and Quick 2016]. For this, the CT data for each hardware component is acquired once and beforehand of further PET/MR examinations. This is a practicable solution for hardware components with rigid structures and with a known position during the PET/MR scan [Quick et al. 2013; Quick 2014].

The CT-based data of each respective hardware component undergoes several post-processing steps to result in a valid 3D attenuation template that then can be used for AC in PET data reconstruction. The following post-processing steps are necessary: cropping the 3D data set, thresholding the HU scale, converting the HU to LAC by using the suggested bilinear conversion curves, filtering the high resolution 3D CT-based template with a Gaussian filter to match the lower resolution of the PET data and, finally, positioning and matching the virtual 3D hardware  $\mu$ map with the real position of the respective hardware component as placed on the PET/MR system patient table. This straightforward method is applied for the patient table of the PET/MR system, for RF coils provided by the vendor, and also has to be applied to every customized and additional hardware component that is used in PET/MR. Whenever a new RF coil is designed and used for PET/MR imaging, the entire cascade of  $\mu$ map generation steps as listed above has to be repeated [Quick 2014; Paulus et al. 2016].

The finalized hardware  $\mu$ maps are then installed on the PET/MR system and are selected automatically, when the designated RF coil is in use. The selection of the  $\mu$ map is done by a linking to the coil files and plug IDs, which means, that RF coils are identified by the operating software of the PET/MR system, when they are used by the customer. When, for example, the spine array RF coil is connected; the plug ID is recognized by the operating system and within the RF coil files the link to the respective deposited  $\mu$ map is noted. Most hardware components like the spine array RF coil or the patient table have larger dimension (e.g. patient table up to 240 cm), whereas the PET FOV for each bed position is only 25.8 cm in axial direction. To select the right section of the  $\mu$ map for hardware AC, the position of the patient table in the matching isocenter of MR and PET is essential for a correct selection of the section of the hardware  $\mu$ map.

For hardware components with a variable position or for flexible structures such as flexible RF body coils [Kartmann et al. 2013], the application of a 3D CT-based  $\mu$ map template is harder to realize since the exact position of flexible RF coils during a PET/MR examination is not known. Attempts with MR-visible markers and post-processing steps to match  $\mu$ maps onto the position are still an active field of research for hardware attenuation correction in hybrid PET/MR [Kartmann et al. 2013].

# Aims of the Thesis

## Aims of the thesis

The overarching aim of this thesis was to develop and evaluate new methods to improve attenuation correction in PET/MR. The following three main parts of the thesis all deal with three different projects and studies that all aim at improving attenuation correction in PET/MR.

In the first part of the thesis new features of human tissue attenuation correction were examined and evaluated in a larger patient study. The previous version of human tissue attenuation correction, as installed on the Siemens Biograph mMR PET/MR system, generated standard MR-based AC maps with only four tissue compartments (background air, lung tissue, fat and soft tissue). Bone information was missing, and due to the limited field-of-view (FOV) in MR imaging, the MR-based AC maps were frequently truncated along the patient's arms. Consequently, these body parts could not be correctly considered in AC of the according PET data. The new AC version (VE11, SP2, Siemens Healthcare GmbH) was first evaluated by our research group at the University Hospital Essen and provides increased spatial resolution, CT-based bone information from an atlas-based bone model, and a new method to increase the lateral FOV in MR imaging, called HUGE ( $B_0$  Homogenization using gradient enhancement). The quantitative impact of the new AC features was examined for a larger group of patients and was systematically investigated in this study.

In the second study of the thesis a dual-tuned birdcage RF head coil initially designed for MR-only use (Rapid Biomedical GmbH, Rimpar) was redesigned for its use in combined PET/MR hybrid imaging. Shape and materials of the RF head coil were selected to match the requirements for a PET compatible and low attenuating design. For integration of the new dual-tuned RF head coil on the Siemens Biograph mMR PET/MR system an according hardware  $\mu$ map was generated by acquisition of a CT-based  $\mu$ map template model of the RF coil. The combination of RF coil and hardware AC was then tested and validated in phantom experiments and was then verified in a patient study to demonstrate clinical use of the dual-tuned RF head coil in PET/MR hybrid imaging.

In the third study, a new 16-channel RF coil for breast imaging was developed and evaluated. Basis for the PET/MR compatible design was a prototype RF breast coil (Rapid Biomedical GmbH, Rimpar), which was adapted and further improved by choosing

low attenuating materials and a PET compatible design for combined PET/MR hybrid imaging. A CT-based  $\mu$ map was generated for hardware attenuation correction of the new RF coil. The performance of the RF breast coil and according AC was tested and validated in phantom experiments and in a subsequent patient study. The implementation of the hardware  $\mu$ map on the Biograph mMR PET/MR system enabled automated hardware attenuation correction, when the 16-channel breast RF coil is used for clinical examinations.

The work described in this thesis resulted in altogether three scientific articles. All three articles have been published in peer-reviewed international journals with impact factor (EJNMMI and Med Phys). Each of the following three main parts of this thesis comprises one of the three scientific articles.

# Introduction

## Introduction Study 1

Attenuation correction (AC) in positron emission tomography (PET) is an essential step to provide accurate and quantitative PET images. With the successful introduction of whole-body hybrid imaging systems, combining PET with computed tomography (CT) [Beyer et al. 2000] or magnetic resonance (MR) imaging [Delso et al. 2011], new possibilities are opened up to perform AC other than using rod-source (511 keV) transmission scans. In hybrid PET/CT systems, CT images providing Hounsfield Units (HU) can directly be transformed to linear attenuation coefficients (LACs) at 511 keV [Carney et al. 2006], the PET photon energy, by using a bilinear conversion [Kinahan et al. 1998]. In PET/MR hybrid imaging, however, PET AC is a methodological challenge [Keereman et al. 2013; Bezrukov et al. 2013], since MR images, providing mainly proton densities and relaxation times, cannot directly be converted to attenuation coefficient maps ( $\mu$ maps) at 511 keV.

In routine whole-body PET/MR hybrid imaging, segmentation-based methods, based on a fast three-dimensional (3D) MR Dixon VIBE sequence with Dixon fat/water separation are used to generate  $\mu$ maps of the patient tissues. This method provides up to four tissue classes including background air, fat, lung, and soft tissue [Martinez-Möller et al. 2009; Schulz et al. 2011]. Due to its short acquisition time and easy implementation, this method is in wide use for clinical PET/MR studies [Drezezga et al. 2012; Wiesmüller et al. 2013; Quick et al. 2013], but has certain limitations compared to CT-based AC [Beyer et al. 2016; Boellaard et al. 2015]. Due to the lack of signal from compact bone in MR images, the 4-compartment segmentation sets the LAC of bone equal to the LAC of soft tissue, leading to a systematic underestimation of PET quantitative metrics i.e. Bq/mL or standard uptake values (SUV) [Beyer et al. 2016]. Another limitation of MR-based AC is the constrained MR imaging field-of-view (FOV), leading to a truncation of the MR-based  $\mu$ map [Beyer et al. 2016; Boellaard et al. 2015; Nuyts et al. 2013].

Regarding the attenuation correction of bone in whole-body PET/MR, several groups have quantitatively evaluated the effect of replacing LACs of bones with a LAC of soft tissue in PET AC  $\mu$ maps. The calculated quantitative effect in these studies ranged from about 6 % to 14 % [Martinez-Müller et al. 2009; Schulz et al. 2011; Samarin et al. 2012; Hofmann et al. 2011], up to 30 % for single bone lesions [Samarin et al. 2012]. Recently, Paulus et

al. evaluated a prototype model-based method for including the LAC of major bone as a 5<sup>th</sup> compartment to the 4-compartment  $\mu$ maps in whole-body PET/MR data sets [Paulus et al. 2015]. The identical bone model-based prototype approach was recently also evaluated for PET/MR imaging of the brain [Koesters et al. 2016]. In both studies, the PET quantification bias due to the inclusion of bone LAC to the MR-based  $\mu$ maps could significantly be reduced to a residual bias of only a few percent [Paulus et al. 2015; Koesters et al. 2016].

Regarding truncation correction, several methods have been explored to complement the truncated MR-based information in AC by estimating the patient's outer contour from non-AC PET images [Delso et al. 2010]. Another approach uses joint estimation of emission and transmission data using the maximum likelihood estimation of an activity and attenuation (MLAA) iterative image reconstruction method [Nuyts et al. 2013; Bal et al. 2011], which is implemented in the currently available PET/MR systems [Beyer et al. 2016]. The quantitative bias on PET quantification caused by truncation of the  $\mu$ map was estimated to range between 15 and 20 % on average [Nuyts et al. 2013; Delso et al. 2010]. Both methods for truncation correction rely on PET information and may be limited in cases, where the radiotracer does not provide unspecific uptake in the patient's tissues and blood pool to derive the outer contours from PET images [Boellaard et al. 2015]. A fully MR-based method for truncation correction has been proposed by Blumhagen et al. [Blumhagen et al. 2013]. This method (B0 Homogenization Using Gradient Enhancement, HUGE) [Blumhagen et al. 2013] achieves an extension of the MR-based left-to-right field-of-view (FOV) from typically 50 cm to 60 cm. Thus, truncation artifacts in the  $\mu$ map along the patient's arms are reduced, and the bias in PET quantification is significantly reduced [Blumhagen et al. 2014].

Both novel features, bone-model and HUGE truncation correction, in independent studies have demonstrated the potential to improve attenuation correction in whole-body PET/MR applications. Improved versions of both techniques are now available as product software for the Biograph mMR PET/MR system (Siemens Healthcare GmbH, Erlangen, Germany). Thus, the aim of this study was to evaluate and quantify the impact of both novel features on PET quantification in whole-body PET/MR. The methods for attenuation correction were tested in a collective of 51 patients with oncologic findings. The standard Dixon-based  $\mu$ map served as a reference for each patient. Multiple reconstructions including involvement of four different  $\mu$ maps for AC allowed for intraindividual comparison of the AC-PET data and systematic evaluation of each features impact on PET quantification.

## Introduction Study 2

Hybrid imaging with simultaneous positron emission tomography and magnetic resonance (PET/MR) has demonstrated to be a powerful diagnostic modality for various applications in [Delso et al. 2011; Quick et al. 2013; Beyer et al. 2016]. While MRI provides excellent soft tissue contrast and various tissue parameters such as diffusion and perfusion, PET provides diagnostic information about tissue function and allows for accurate quantification of radiotracer distribution in the human brain and entire body [Drzezga et al. 2012; Wiesmüller et al. 2013].

Simultaneous image acquisition in PET/MR requires the use of radiofrequency (RF) coils for MRI signal detection that are optimized regarding their PET transparency. Conventional RF coils for MR-only use are often not well suited for the operation in integrated PET/MR systems, since the RF coil casing and contained electronic components are located in the field-of-view of the PET detector during independent PET and MRI data acquisition [Quick 2014]. This causes photon attenuation, which may introduce a bias in tracer activity quantification with PET [Iaguru et al. 2015; Keereman et al. 2013; MacDonald et al. 2011].

While any RF coil for use in PET/MR in general shall be optimized for PET transparency [Delso et al. 2010], i.e. provide lowest possible photon attenuation, additional methods for attenuation correction (AC) are warranted to provide accurate tracer activity quantification with PET [MacDonald et al. 2011; Tellmann et al. 2011; Paulus et al. 2012; Paulus et al. Paulus et al. 2013; Oehmigen et al. 2016; Dregerly et al 2015; Aklan et al. 2013]. In former stand-alone PET systems, AC was achieved by a transmission scan with  $^{68}\text{Ge}$  rod sources that provided a spatial distribution of linear attenuation coefficients (LAC) across the patient tissues [Carney et al. 2006]. In PET/computed tomography (CT) hybrid imaging, AC is performed by using the CT transmission data to calculate the attenuation in human tissues [Carney et al. 2006; Kinahan et al. 1998]. In PET/MR, attenuation correction of patient tissues and hardware components such as RF coils has to be solved in different ways since transmission data either from  $^{68}\text{Ge}$  rod sources or from CT is not available [Delso et al. 2010].

Several approaches for attenuation correction in PET/MR have been established. Patient tissues are attenuation corrected by using MR-based VIBE (volume interpolated breath hold examination) sequences with Dixon fat/water separation to generate  $\mu$ maps of the patient tissues [Martinez-Möller et al. 2009; Schulz et al. 2011]. This is the base for 4-compartment tissue segmentation into background air, fat, lung, and soft tissue [Martinez-Möller et al. 2009]. In addition, further MR sequences such as ultrashort TE (UTE)

[Keereman et al. 2010; Navalpakkam et al. 2013] and zero echo time (ZTE) [Delso et al. 2015] are used to provide cortical bone segmentation of the skull in PET/MR neuroimaging. Also, atlas-based methods are used for bone segmentation in whole-body PET/MR applications [Paulus et al. 2015; Koesters et al. 2016].

For attenuation correction of hardware components such as RF coils or the patient table, CT-based  $\mu$ maps of the hardware components are joined with the patient  $\mu$ map before PET data reconstruction. The hardware component  $\mu$ maps are based on CT transmission scans of the RF coils and provide the spatial distribution of attenuation factors in a 3D model of the respective hardware component [Paulus et al. 2012; Paulus et al. 2013; Carney et al. 2006; Paulus et al. 2016]. Due to the patient table position, the position of rigid RF coils (e.g. RF head coil, RF spine array coil) during a PET/MR examination is known and the template-based AC using the CT-derived  $\mu$ map can be performed during the PET data reconstruction process [Paulus et al. 2016].

Among the wealth of MR imaging (MRI) and MR spectroscopy (MRS) methods,  $^{13}\text{C}$  NMR is the method of choice for studying brain and cancer metabolism [Rodrigues et al. 2013; Cho et al. 2017]. Complementing structural proton ( $^1\text{H}$ ) MR imaging,  $^{13}\text{C}$  carbon MRS provides additional diagnostic criteria for tumor characterization and patient stratification [Cho et al. 2017; Gordon et al. 2015]. The combination of integrated PET/MR with  $^{13}\text{C}$  C MRS and MRI potentially offers simultaneous dual-modality metabolic imaging [Hansen et al. 2016]. Due to the inherently low natural abundance of endogenous  $^{13}\text{C}$  C, however, hyperpolarization techniques are needed to increase the  $^{13}\text{C}$  C signal in MRI and MRS to clinically usable levels [Månsson et al. 2006]. Hyperpolarization of  $^{13}\text{C}$  is only recently available at selected sites. The combination of  $^{13}\text{C}$  hyperpolarization and PET/MR hybrid imaging is of high potential interest in multi-modal, multi-parametric neuroimaging, but due to technical hurdles, this has not been fully realized in clinical applications yet [Gordon et al. 2015; Hansen et al. 2016]. One missing link before clinical application on humans is the fact, that no radiofrequency (RF) head coil for  $^{13}\text{C}/^1\text{H}$  MR signal reception for use in PET/MR is available today.

In this study, a new dual-tuned  $^{13}\text{C}/^1\text{H}$  RF head coil was designed to be used in integrated PET/MR hybrid neuroimaging. For attenuation correction of the RF head coil, CT-based attenuation templates were acquired and implemented into the PET data reconstruction process. Systematic evaluation of the RF coil and its attenuation correction was then performed in phantom and patient examinations.

## Introduction Study 3

Integrated whole-body positron emission tomography/magnetic resonance (PET/MR) hybrid imaging combines excellent soft tissue contrast and various functional imaging parameters provided by MR with high sensitivity and quantification of radiotracer metabolism provided by PET. While the initial physical and technical challenges have been solved and sequential and integrated PET/MR systems are now commercially available [Zaidi et al. 2011; Delso et al. 2011; Quick et al. 2013; Jaguru et al. 2015], the broader evaluation of PET/MR in various clinical applications now is under way [Bailey, Antoch et al. 2015; Bailey, Pichler, et al. 2015].

One of the clinical oncologic applications of integrated PET/MR hybrid imaging which has recently gained high interest is breast cancer assessment by combining the diagnostic advantages of MR imaging and PET [Tabouret-Viaud et al. 2015]. Recent clinical studies have investigated the potential of PET/MR for breast cancer metastasis screening and staging in whole-body examinations [Pujara et al. 2016; Catalano et al. 2015; Sawicki et al. 2016] or in dedicated local breast tumor staging examinations [Taneja et al. 2014; Grueneisen et al. 2015]. While whole-body PET/MR imaging studies for breast cancer metastasis screening make use of a combination of multiple vendor-provided radiofrequency (RF) coils for whole-body MR signal detection (e.g. head/neck RF coils, spine RF coils, several body RF coils), the dedicated examination and staging of local breast tumors, on the other hand, requires dedicated RF breast coils for MR signal detection. Such breast RF coils, in the context of PET/MR hybrid imaging, need to fulfill specific requirements in terms of low attenuation of PET signals and appropriate attenuation correction to provide artifact free PET images and, furthermore, accurate PET activity quantification of local breast tumors.

Multichannel RF receiver coils are a technical precondition for high-resolution high-quality MR imaging and are well established in clinical MR imaging. In PET/MR imaging, however, the RF receiver coils are located in the field-of-view (FOV) of the PET detector during simultaneous PET and MR data acquisition and, consequently, attenuate the number of true annihilation events and lead to inaccurate PET activity quantification results if used without appropriate methods for attenuation correction (AC). Thus, beyond providing excellent signal-to-noise-ratio (SNR) and signal homogeneity for high quality MR imaging, an additional design parameter for PET/MR hybrid imaging is that all RF receiver coils and hardware components have to be optimized for PET-transparency [Delso et al. 2010; Tellmann et al. 2011; MacDonald et al. 2011; Paulus et al. 2012]. Furthermore, all residual hardware component attenuation and scatter needs to be corrected by applying appropriate

AC methods to allow for reliable and accurate PET activity quantification [Paulus et al. 2013]. These statements regarding RF coils and their attenuation correction are generally applicable to all current PET/MR systems, the Ingenuity TF PET/MR system (Philips) [Zaidi et al. 2011], the Biograph mMR (Siemens) [Delso et al. 2011], and the Signa PET/MR (GE) [Grant et al. 2016].

Attenuation correction and scatter correction in PET/MR is performed twofold. Attenuation and scatter due to the patient tissues is corrected by using MR imaging with, for example, a Dixon-based sequence and subsequent tissue class segmentation with assignment of different linear attenuation coefficients (LAC) to individual tissue classes [Martinez-Möller et al. 2009; Beyer et al. 2016]. This method for patient tissue AC in PET/MR can be considered established standard in all current PET/MR systems [Zaidi et al. 2011; Delso et al. 2001; Grant et al. 2016; Beyer et al. 2016; Quick 2014]. Beyond this clinical standard, the use of ultrashort echo time (UTE) sequences has been proposed to additionally provide bone information for brain imaging studies [Larsson et al. 2013; Navalpakkam et al. 2013]. Another recent study has suggested a model-based approach to add the attenuation properties of major bones to the Dixon soft tissue attenuation map in whole-body PET/MR examinations [Paulus et al. 2015].

Hardware components such as the system's patient table and RF coils needed for MR signal reception are not visible in MR images [Paulus et al 2012]. Consequently, attenuation and scatter from these structures cannot be derived from the MR imaging data available in PET/MR. Predefined attenuation maps (templates) for rigid RF coils thus are usually added to the patient attenuation map before the PET reconstruction. These templates are based on CT transmission scans of the RF coils and provide an exact 3D representation of the spatial distribution of attenuation factors in a virtual model of the respective hardware component. By automatically linking the current patient table position during a patient examination to the known position of the RF coil on the patient table, template-based AC can be performed during the PET data reconstruction process [Delso et al. 2010; Paulus et al 2012]. This method of hardware component attenuation and scatter correction of RF coils today can be considered as an established standard for most of the RF coils that are provided for the currently available PET/MR systems by all three vendors.

As mentioned above, local breast cancer tumor staging with PET/MR requires dedicated RF coils designed and tested for the combined modality imaging use. This also requires the breast RF coil being attenuation corrected with an appropriate attenuation map. In an initial study, Aklan et al. have successfully integrated a 4-channel RF breast coil with an appropriate CT-based attenuation template into the concept of simultaneous PET/MR hybrid imaging to enable accurate PET/MR hybrid imaging and PET activity quantification of local breast cancer [Aklan et al. 2013]. Following this strategy, Dregely et al. in another

initial study have evaluated an early 16-channel prototype RF breast coil with AC, providing a higher number of RF receiver channels for improved MR imaging performance [Dregerly et al. 2015].

As a further development of the prototype RF breast coil and work presented by Dregely et al. [Dregerly et al. 2015] in the present study we describe the design, hardware attenuation correction, its PET/MR system implementation, and first clinical evaluation of the final product version of a 16-channel RF breast array coil. The RF coil is designed for optimized MR imaging performance and maximized PET transparency. A dedicated 3D attenuation template model for the new RF breast coil was generated by CT imaging and by subsequent conversion of the Hounsfield attenuation values to LAC. In this work a dedicated RF coil holder was designed to ensure accurate repositioning of the breast RF coil at a defined position on the PET/MR system patient table to accurately match the position of the RF coil with its 3D AC template model. Repositioning accuracy was determined in repeated measurements using MR-visible markers. Phantom experiments in MR and PET imaging provide a systematic evaluation of the RF coil performance parameters. An initial clinical study on a small group of ten patients with local breast cancer lesions serves as in vivo validation of the phantom results.

# Materials and Methods

## Material and Methods Study 1

### *PET/MR hybrid system*

The patient measurements were performed on an integrated PET/MR whole-body hybrid imaging system (Biograph mMR; Siemens Healthcare GmbH, Erlangen, Germany). The PET detector is fully integrated into the 3-Tesla MRI system, which allows for simultaneous PET and MR data acquisition [Delso et al. 2011; Quick 2014; Delso et al. 2010]. The current version of the PET/MR operating system at the time of this study is syngo MR E11P (Siemens Healthcare GmbH, Erlangen, Germany).

For whole-body imaging, several RF receiver coils were used. The 24-channel RF spine array coil, which is located on the patient table, the 16-channel RF head/neck coil and also three to four flexible 6-channel RF body matrix coils were used for signal reception, which are placed onto the patient's body.

### *Patient Measurements*

The study was conducted in accordance with all guidelines set by the approving institutional review board. Written informed consent was obtained before scanning of the patients. Fifty-one patients (31 female and 20 male, mean age  $57 \text{ y} \pm 14 \text{ y}$ ; mean BMI  $25.3 \pm 4.2$ ) were included into this study. All patients were injected with 18-Fluorodesoxyglucose ( $^{18}\text{F}$ -FDG) ( $235 \text{ MBq} \pm 49 \text{ MBq}$ ) as radiotracer and underwent a whole-body PET/MR examination ( $140 \text{ min} \pm 45 \text{ min}$  after injection) subsequent to clinical indicated PET/CT. All relevant patient data are provided in Table 1. A range of four to six bed positions for the whole-body examinations was chosen, depending on the individual patient size, and to cover the patient body from head to upper thigh. Patients with a broad range of oncologic indications for whole-body PET/MR hybrid imaging were included into this study. The indications for PET/MR included: lymphoma (23), bronchial carcinoma (17), cervix carcinoma (6), mamma carcinoma (5).

## **Hardware Component Attenuation Correction**

Photon attenuation by rigid hardware components (patient table, RF spine array coil, RF head/neck coil) is automatically involved in the AC by the PET/MR system using an established method [Quick 2014] by the vendor. Hardware component AC is based on 3-dimensional CT-based attenuation templates of the respective hardware component and RF coils [Quick 2014; Paulus et al. 2013; Oehmigen et al. 2016; Aklan et al. 2013]. The AC templates are automatically used during the PET data reconstruction process to perform attenuation correction of all associated hardware components [Quick 2014; Paulus et al. 2013]. Automatic attenuation correction of flexible RF body coils is still a challenging task since both the individual position and geometry of flexible RF coils during an examination are not fully known [Paulus et al. 2012]. Consequently, automatic registration of CT-based attenuation templates is not straightforward [Kartmann et al. 2013].

It has been shown, however, that the attenuation bias due to flexible RF coils is in the range of only few percent [Paulus et al. 2012; Kartmann et al. 2013] and, thus, the flexible RF coils are not considered in hardware component AC. In this study the potential quantitative impact of flexible RF coils on attenuation correction as confounding factor has been eliminated by study design. This was achieved by multiple reconstruction of each patient's PET data set, each time with applying another AC method. Thus, the relative impact of RF coils on the different PET data reconstructions was identical for all reconstructions.

**Table 1: Patient data**

No.	Age	Sex	BMI	Height (cm)	Weight (kg)	MBq	Scan start [min p.i.]
#1	62	f	24.1	163	64	179	81
#2	66	f	33.7	168	95	272	175
#3	56	m	28.1	177	88	243	137
#4	52	m	31.2	187	109	283	190
#5	66	m	23	178	73	255	241
#6	53	f	29.4	165	80	205	154
#7	76	f	17.7	168	50	288	170
#8	64	f	27.5	163	73	180	92
#9	70	f	20.7	158	52	202	112
#10	41	f	23.7	163	63	184	102
#11	54	m	22.5	174	68	280	117
#12	77	m	29.3	178	93	242	123
#13	70	m	23.5	182	78	313	159
#14	52	m	28.1	183	94	347	111
#15	63	f	27	169	77	218	115
#16	28	f	22.3	160	57	222	59
#17	63	f	30.9	165	84	212	162
#18	36	f	20.1	153	47	153	106
#19	38	f	33.3	176	103	242	92
#20	52	f	23.4	160	60	188	257
#21	29	f	23.5	165	64	175	61
#22	45	m	23.1	180	75	320	162
#23	67	m	25.2	178	80	320	125
#24	72	m	24.2	170	70	231	148
#25	49	m	28.4	178	90	280	167
#26	45	f	23.4	168	66	203	158
#27	58	f	25.5	168	72	275	120
#28	72	f	26.8	164	72	250	131
#29	77	f	23	168	65	217	179
#30	58	m	24.3	178	77	304	139
#31	65	f	17.3	170	50	145	160
#32	72	f	24.8	163	66	218	166
#33	50	f	21.9	164	59	139	63
#34	22	f	17.8	167	50	220	130
#35	31	f	16.4	171	48	208	59
#36	64	f	29.4	164	79	190	96
#37	55	m	26.9	183	90	284	165
#38	31	m	35.8	183	120	312	134
#39	62	f	30.5	168	86	261	170
#40	70	f	21	158	53	194	141
#41	75	m	24.9	178	79	308	134
#42	54	m	20.7	176	64	242	130
#43	75	f	26.1	175	80	202	111
#44	49	m	30.6	187	107	284	217
#45	48	m	24.8	168	70	210	204
#46	57	f	27.1	163	72	210	152
#47	63	f	24.8	168	70	194	155
#48	75	f	27.1	155	65	231	202
#49	48	f	24.4	167	68	199	80
#50	62	m	25.7	186	89	275	222
#51	68	f	31.9	168	90	188	121
<b>Mean ±SD</b>	<b>57 y ±14 y</b>	<b>31 f 20 m</b>	<b>25.3 ±4.2</b>	<b>170 cm ±8 cm</b>	<b>74 kg ±16 kg</b>	<b>235 MBq ±49 MBq</b>	<b>140 min ±45 min</b>

## Soft Tissue Attenuation Correction

Although in the following mostly the term “attenuation correction” is used, all attenuation  $\mu$ maps are applied to perform both, image-based attenuation correction and scatter correction. The patient-specific tissue attenuation correction and scatter correction associated with the new system product software syngo MR E11P as evaluated in this study is based on a high-resolution, Dixon protocol of the VIBE (volumetric interpolated breath-hold examination) sequence with CAIPIRINHA parallel imaging acceleration [Breuer et al. 2005] that provides higher spatial resolution than previous AC sequence implementations. The CAIPIRINHA Dixon-VIBE is a 3D sequence that is acquired in transaxial orientation. Reconstruction of MR-based  $\mu$ maps for attenuation and scatter correction is performed in coronal orientation. The Dixon-VIBE soft tissue AC sequence protocol used for the attenuation correction in this implementation uses the following scan parameters: parallel imaging acceleration factor  $R=5$ ; matrix  $390 \times 240$  with  $1.3 \times 1.3 \text{ mm}^2$  in-plane pixel size, 136 slices each 3.0 mm, flip angle =  $10^\circ$ , TR 3.8 ms, TE1/2 = 1.2/2.4 ms, TA 10.6 sec. The MR-based image information of the patient provided by the Dixon-VIBE sequence is segmented into four different compartments that are all assigned with a specific linear attenuation coefficient (LAC) for soft tissue ( $0.1 \text{ cm}^{-1}$  LAC), fat ( $0.0854 \text{ cm}^{-1}$  LAC), lung ( $0.0224 \text{ cm}^{-1}$  LAC) and air ( $0.0 \text{ cm}^{-1}$  LAC). This sequence providing four distinctions for attenuation correction in the following is referred to as 4-compartment  $\mu$ map and serves as a reference in this study.

## Attenuation Correction of Bone

The 4-compartment Dixon-VIBE sequence does not provide attenuation information of bone tissue [Martinez-Möller et al. 2009]. Bones are segmented and substituted with the LAC of soft tissue. This may lead to systematic local underestimation of the real attenuation in bony tissue regions [Beyer et al. 2016; Samarin et al. 2012]. A new feature of the syngo MR E11P software (Siemens Healthcare GmbH) now reconstructs bone data with its own tissue class as 5<sup>th</sup> compartment from the high-resolution CAIPIRINHA Dixon-VIBE sequence. The bone data is reconstructed applying a model-based bone segmentation algorithm (Siemens Healthcare GmbH) [Paulus et al. 2015; Koesters et al. 2016; Rausch et al. 2017]. The new bone-model method generates a  $\mu$ map based on the standard 4-compartment Dixon AC. Bone information is added to this  $\mu$ map using a model-based bone segmentation algorithm that applies continuous LACs for bone. The model-based method assigns continuous LAC to bone from  $0.1 \text{ cm}^{-1}$  up to  $0.2485 \text{ cm}^{-1}$ . More detailed information on the bone-model is provided in the work by Paulus et al. [Paulus et al. 2015].

The offline generated skeleton model consists of the major bones including the skull, the spine, the pelvis and both upper femur bones (Figure 1). The bone model is registered by non-rigid registration to the individual MR-based Dixon-VIBE images of the patient. The segmentation, masking, registration and matching process of the bone mask to the given MR images is performed in two steps. First, MR imaging-based landmarks define the patient bones and set them into a relation to the bone mask. Secondly, a deformable 3D registration adapts the bone mask in size and shape more precisely to the individual bone information of the patient [Paulus et al. 2015]. The segmentation from the CAIPIRINHA Dixon-VIBE sequence protocol with added bone model providing a fifth tissue class for attenuation correction of bone in the following is referred to as 5-compartment  $\mu$ map.

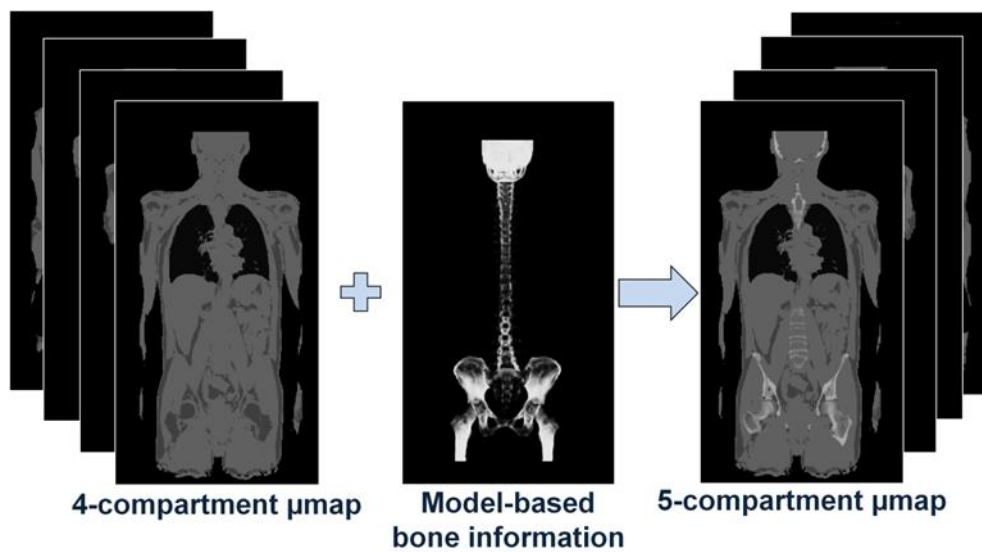


**Figure 1:** Schematic representation of adding bone information to the MR-based  $\mu$ map representing soft tissues. The standard Dixon MR sequence-based 4-compartment  $\mu$ map provides tissue class segmentation for fat, soft tissue, lung tissue and background air. A model-based atlas additionally provides continuous LAC values for bone to the 4-compartment  $\mu$ map. Based on the patients individual MR-data, a model-based skeleton of the major bones (skull, spine, pelvis, and both femurs) is adapted and added to the 4-compartment  $\mu$ map.

### Truncation Correction

The currently established MR-based patient tissue attenuation correction techniques are limited by the fact that the transaxial FOV in MR imaging is limited. All body parts exceeding this limited FOV, as for example the arms will be truncated from the MR-based  $\mu$ map. A fully MR-based method for truncation correction of the peripheral body regions is the  $B_0$  homogenization using gradient enhancement (HUGE) technique as proposed by Blumhagen et al. [Blumhagen et al. 2013; Blumhagen et al. 2014]. In the present work, the most recent product implementation of the HUGE technique is used, featuring a moving table acquisition for providing up to 60 cm left-to-right seamless MR-imaging coverage for the left and right arm of the patient under investigation. The truncation corrected areas of the right and left side of the patient from the HUGE sequence are merged with the 4-compartment reference  $\mu$ map and, thus, provide attenuation correction of the center body-regions, as well as the peripheral regions along the patients arms (Figure 2). In the context of this study, PET-based contour detection with MLAA was deactivated for all patient examinations and PET data reconstructions. Thus, the impact of MR-based truncation correction using the HUGE method on PET-quantification could be systematically investigated [Lindemann et al. 2017].

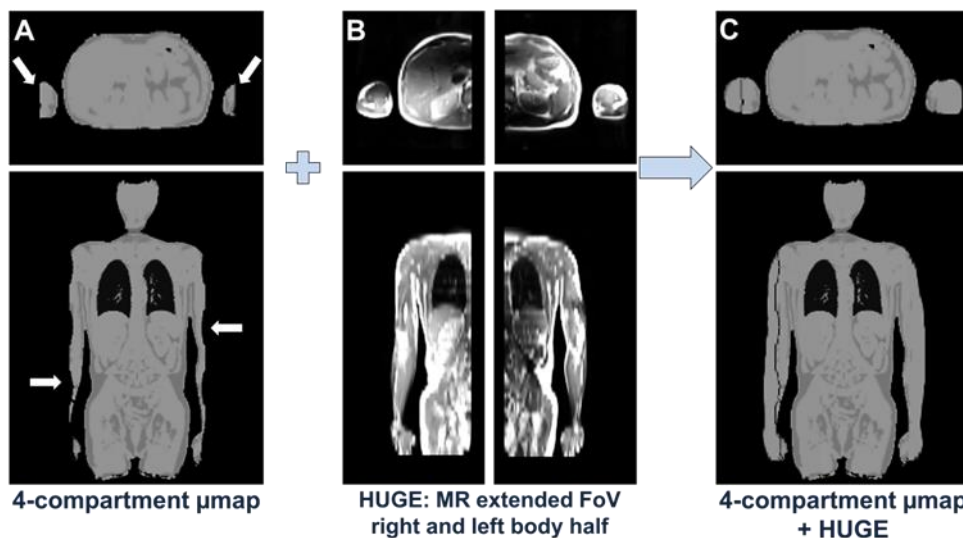


**Figure 2:** Schematic representation of MR-based truncation correction with the HUGE method. The standard 4-compartment  $\mu$ map shows geometric distortions and MR signal truncation in peripheral regions, i.e. along the patient's arms (A). Applying the HUGE method (two measurements for left and right arm) provides non-truncated MR-data from peripheral regions (B). Thus, HUGE increases the MR-based field of view in left-right direction and can be used to restore the, otherwise, truncated regions along the arms (C).

### ***PET Data Reconstruction***

The PET data of the patients were reconstructed iteratively using a 3-dimensional ordinary Poisson ordered-subsets expectation maximization (3D OP-OSEM) with three subsets and 21 iterations. The PET/MR imaging matrix is scaled to  $344 \times 344$  with a reconstructed pixel size of  $2.09 \times 2.09 \text{ mm}^2$ . Depending on the size of the overall FoV in longitudinal direction (z-direction), the number of the bed positions defines the overall number of reconstructed transaxial PET slices. For three bed positions, 321 transaxial slices were reconstructed; for four bed positions 418, and for five bed positions 515 slices were reconstructed. Each slice has a reconstructed thickness of 2.03 mm. The PET images were smoothed with a Gaussian filter having a full width at half maximum of 4 mm.

### ***PET Quantification***

To systematically evaluate the impact of the new attenuation correction methods on PET quantification in this study, four different  $\mu$ maps were generated offline for each patient. The 4-compartment- $\mu$ map (Dixon-VIBE) serves as reference (Fig. 3A) and was compared individually to the 5-compartment- $\mu$ map including bone (Fig. 3B), to the 4-compartment- $\mu$ map with HUGE truncation correction (Fig. 3C), and to the 5-compartment- $\mu$ map with HUGE (Fig. 3D). The default AC setting in the product protocols features the 5-compartment- $\mu$ map with the HUGE option. The other settings can be achieved by retrospective reconstructions with modified settings.

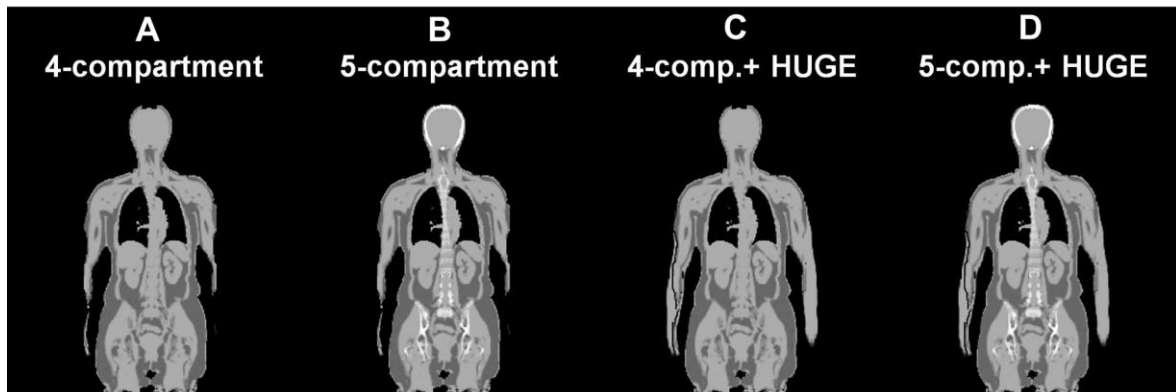


**Figure 3:** Four different  $\mu$ maps for attenuation correction of PET data were generated for each patient. The Dixon-sequence MR-based 4-compartment- $\mu$ map serves as reference. For the 5-compartment- $\mu$ map, additional bone segmentation is added by applying the bone model. Applying the HUGE method provides truncation correction. The combined 5-compartment- $\mu$ map plus HUGE merges all tissue attenuation information (truncation and bone) to a single human-tissue  $\mu$ map.

To create four comparable AC PET datasets of each patient, the PET rawdata and the different  $\mu$ maps were retrospectively reconstructed using the PET/MR system provided

reconstruction tool 'RetroRecon' (Siemens Healthcare GmbH). For each patient, the non-AC whole-body PET data was reconstructed four times using each of the four different  $\mu$ maps.

The resulting four AC PET image datasets of all 51 patients were evaluated and rated by an experienced radiologist (ten years of PET/CT and PET/MR reading) and an experienced nuclear medicine specialist (eight years of PET/CT and PET/MR reading) in consensus. Image reading consisted of identifying the primary tumor or lesion and up to two further lesions with focal increased  $^{18}\text{F}$ -FDG -uptake per patient, depicting volume-of-interest (VOI) and computing the  $\text{SUV}_{\text{max}}$  in the PET data sets of each patient. For each patient, the identical PET data set, each time reconstructed with each of the four different attenuation correction maps, were examined by readers. The VOIs placed in the first reconstructed PET data set served as a reference for the other three reconstructions of the same PET data set. Placement of VOIs was done with the help of a syngo.via workstation (Siemens Healthcare GmbH), to ensure accurate and identical placement of all VOIs in all four PET data reconstructions.

Furthermore, potential artifacts such as bone model misplacements or signal inconsistencies or signal dropouts on the 5-compartment and HUGE  $\mu$ map were noted. To visualize activity differences between the four reconstructed AC PET datasets, the images resulting from the AC PET data using new features (bone model and HUGE) were mathematically subtracted and then divided by the images from PET data that were reconstructed by using the 4-compartment  $\mu$ map serving as reference.

$$\text{Eq. 4} \quad \textit{relative difference maps} = \frac{\textit{SUV}_{\textit{new features}} - \textit{SUV}_{\textit{4compartment}}}{\textit{SUV}_{\textit{4compartment}}}$$

The calculation and visualization of the relative difference maps between the four AC PET data sets was performed with MATLAB 2013b (The MathWorks Inc., Natick, Massachusetts, United States) Also, the graphical visualization of the  $\text{SUV}_{\text{max}}$  gain or loss for each lesion was performed with MATLAB.

## Materials and Methods Study 2

### *PET/MR hybrid system*

All phantom and patient measurements were performed on an integrated 3-Tesla (3T) PET/MR whole-body hybrid system (Biograph mMR; Siemens Healthcare GmbH, Erlangen, Germany), which allows for simultaneous PET and MR imaging [Delso et al. 2011; Quick 2014].

### *PET/MR dual-tuned head imaging RF coil*

Basis for the development of a dual-tuned  $^{13}\text{C}/^1\text{H}$  RF head coil for use in integrated PET/MR was a product 3T dual-tuned RF head coil for MR-only use (Rapid Biomedical GmbH, Rimpfing, Germany). The MR-only RF coil underwent several design optimizations to reduce PET signal attenuation and, thus, to increase its PET transparency for use in PET/MR. Major changes in the RF coil design were the following. The 16-rung birdcage antenna length was increased from 209 mm to 265 mm. This maximizes the length of the birdcage part of the RF coil to match the length of the integrated PET detector (259 mm) [Delso et al. 2011; Quick 2014]. Increasing the length of the birdcage resonator required a retuning of both  $^1\text{H}$  and  $^{13}\text{C}$  resonance frequencies. Due to quadrature polarization, the RF coil is optimized for RF signal transmission and reception for both nuclei. The RF coil is dual-tuned to the Larmor frequencies of  $^1\text{H}$  123 MHz and  $^{13}\text{C}$  31 MHz at 3 Tesla, serving as volume RF coil for the two MR nuclei. All electronic components and connecting cables were positioned outside of the FOV of the PET detector, since solder and copper are strong attenuating materials. Instead of using copper tubes with 0.5 mm wall thickness as for the 16 rungs of the MR-only birdcage, circuit boards with a 35  $\mu\text{m}$  copper layer were used as resonators in the redesigned PET/MR RF head coil (Figure 4). The wall thickness of the RF coil casing was reduced to minimize the attenuation of the photons. The outer end-ring of the birdcage antenna, which is located near to the patient shoulders, was designed thinner than in the MR-only product version of the RF coil. The coil casing was designed to fit at a defined position on the patient table of the PET/MR system. This is a prerequisite for accurate attenuation correction applying CT-based 3D attenuation templates, which can only be achieved when the hardware  $\mu\text{map}$  during the PET data reconstruction and the RF head coil on the patient table during PET data acquisition exactly match in their positions [Quick 2014; Paulus et al. 2012; Paulus et al. 2013; Oehmigen et al. 2016].

The dual-tuned  $^{13}\text{C}/^1\text{H}$  birdcage resonator is equipped with filters and decoupling mechanisms for enabling wideband alternating-phase low-power technique for zero-residual splitting (WALTZ) decoupling [Widmaier et al. 1998]. Dual-tuned RF coils equipped

with spin decoupling when using WALTZ sequences in principle enables increasing the signal-to-noise in NMR spectra while reducing the specific absorption rate (SAR) [Widmaier et al. 1998].

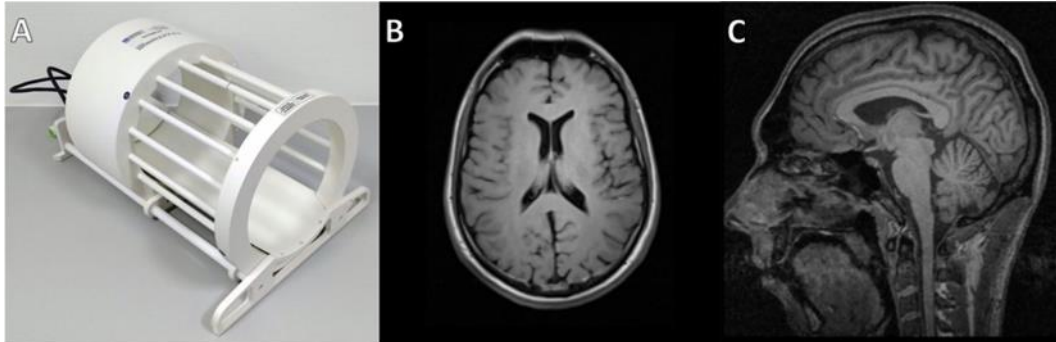


**Figure 4:** Dual-Tuned  $^{13}\text{C}/^1\text{H}$  radiofrequency head coil that was designed for use in PET/MR hybrid imaging. (A). T1 transversal dark fluid (FLAIR)  $^1\text{H}$  MR image of a healthy volunteer in transversal orientation (B). T1 MPRAGE in sagittal orientation (C).

### **Phantom measurements**

Phantom experiments were performed to evaluate functionality and accuracy of attenuation correction and to provide a means for systematic quantification of PET signal attenuation parameters. A cylindrically shaped phantom (volume 9.48 l) was used. The phantom is equipped with a handlebar for transport and can additionally be filled with radiotracer by ports on the top lid, thus providing a homogeneous large-volume emission source.

The PET/MR hybrid system provides a dedicated phantom holder for the cylindrical phantom. The phantom holder enables the phantom to be fixed facing the head end of the patient table. This mounting holds the phantom in a free-floating position several centimeters above the head end of the patient table in co-axial orientation to the table. The height of the phantom floating over the table can be chosen such that the RF head coil can be placed on the table and surrounding the phantom. Alternatively, the RF coil can be removed without repositioning the phantom. Thus, the phantom can be used as homogeneous and large-volume PET emission source, enabling difference measurements with and without the RF head coil in place.

To serve as PET emission source in this study, the phantom was filled with  $^{18}\text{F}$  radiotracer for all following phantom scans with an initial activity concentration of 13 kBq/ml, resulting in a total activity of 124 MBq for the whole phantom. The phantom was centered with its longitudinal axis along the longitudinal axis of the RF coil (Figure 2A). The scan time for one measurement was 30 min. The rather high phantom activity and rather long acquisition time in the phantom experiments were chosen such that the difference measurements with and without RF coil in place provide sufficient PET signal statistics and

homogeneity to accurately evaluate the attenuating effects of the RF coil hardware. PET data was recorded in list-mode.

Two phantom measurements were executed to obtain difference measurements (Figure 5). Both sets of experiments were time- and decay-corrected to compensate the different measurement starting points and for tracer decay over time.

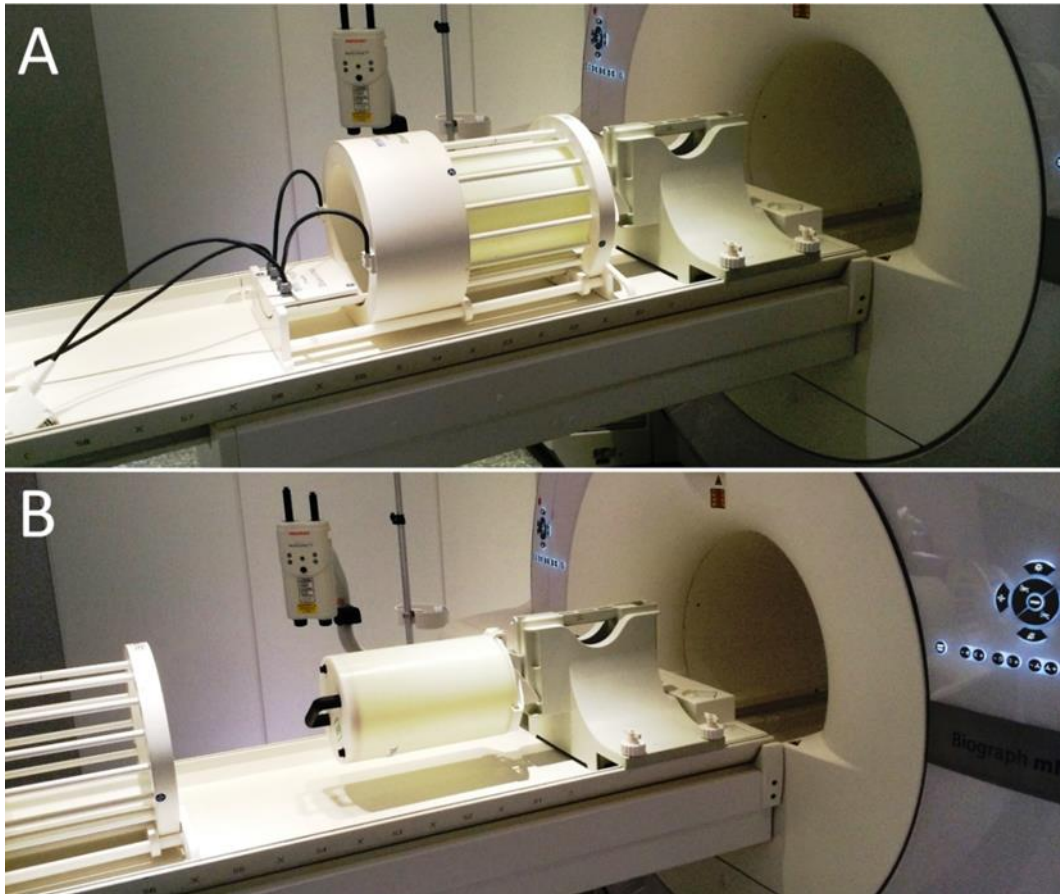


**Figure 5:** Phantom experiment to measure PET signal attenuation caused by the RF coil being placed in the field-of-view of the PET detector. Two measurements were performed: with RF head coil (A) and without RF coil placed around the active transmission phantom (B). Thus, difference maps can be acquired to determine the spatial distribution of PET signal attenuation caused by the RF coil across the homogeneous phantom volume. During the phantom experiments, the centers of the RF coil and phantom were centered to the middle of the PET detector.

### **Attenuation Correction**

An established method for the attenuation correction of human tissues in PET/MR is based on MR measurements [Beyer et al. 2016; Quick 2014]. Based on a Dixon-VIBE sequence, fat and water signal images are acquired to segment the patient tissue into four different classes: fat, soft tissue, lung and air. The MR parameters for the Dixon-VIBE sequence used in this study are as follows: image matrix  $192 \times 192$ ; spatial in-plane resolution

2.6 × 2.6 mm<sup>2</sup>; slice thickness 3.12 mm; TR 3.6 ms, TE1 1.23 ms and TE2 2.46 ms; flip angle 10°, acquisition time 19 sec/bed position.

For attenuation and scatter correction of hardware components and RF coils in PET/MR, the method of using different CT-based attenuation templates has been established [Delso et al. 2011; Quick 2014; Paulus et al. 2016]. During the phantom experiments in this study, the MR-based Dixon VIBE images of the phantom only serve as the basis for position detection of the phantom during the experiments. This position was then used as a marker to accurately co-register the CT-based  $\mu$ map template for attenuation correction of the phantom during PET data reconstruction. Thus, the Dixon MR data was only used for position detection; the CT-data was used for attenuation correction of the phantom as described below. The MR-based data was not directly used for attenuation correction of the phantom since the phantom casing and other attenuating parts of the phantom do not provide MR signal and, thus, cannot be accurately corrected [Ziegler et al. 2015].

The CT imaging for the RF head coil (Figure 6A) and the phantom (Figure 6B) was performed on a dual source CT scanner (SOMATOM Definition Flash, Siemens Healthcare GmbH, Erlangen, Germany). The following parameters were used: tube voltage 140 keV, tube current 500 mA, matrix size of 512 × 512 pixels, voxel size 0.3 × 0.3 × 0.6 mm<sup>3</sup> and a B30f-smooth convolution kernel. The CT data with an energy window level for the photons of 140 keV was converted to the PET energy level of 511 keV with a bilinear conversion function [Carney et al. 2006; Ziegler et al. 2015].

This conversion from Hounsfield units (HU) to linear attenuation coefficients (LAC) and the following steps such as signal thresholding, artifact removal, and subsequent Gauss filtering were performed with MatLab 2013b (MATrix LABoratory, MathWorks, Massachusetts, USA) using a custom-written program. The following image processing steps were performed to exactly match the CT-based model with the fixed position of the RF head coil on the patient table. A signal threshold was applied to CT data to reduce CT streak artifacts around highly attenuating components. To match the high spatial resolution of the CT data with the lower spatial resolution of the PET detector (4.0 - 6.0 mm), a Gaussian filter was applied. For registration and matching of the  $\mu$ map with the exact position of the RF coil on the patient table Vinci (Vinci Version 4.63, Max-Planck-Institute for Metabolism Research, Cologne, Germany) was used.

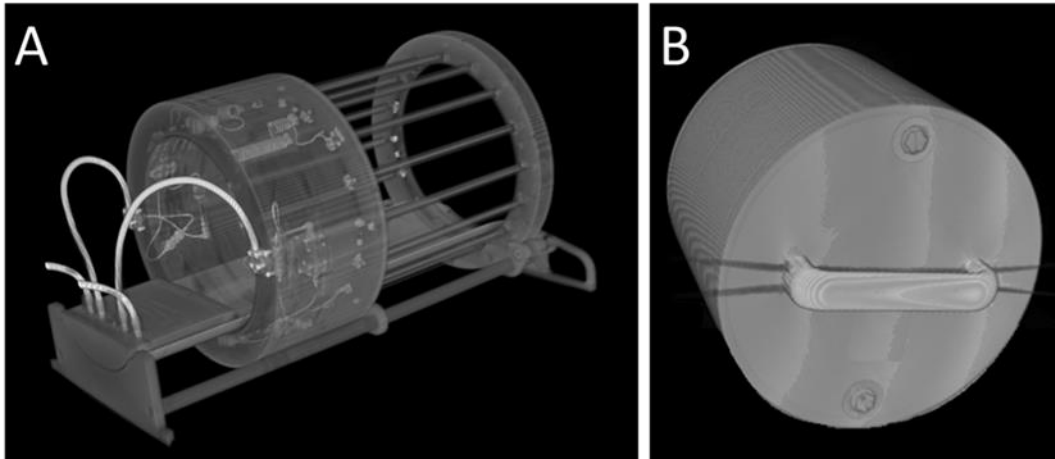


**Figure 6:** A CT-template of the dual-tuned head coil (here as 3D rendering) shows that the most-attenuating electronic components are located in the wider casing to the left which is positioned outside of the PET detector (A) during PET/MR imaging. The CT-based attenuation template of the cylindrical water transmission phantom was applied in all phantom measurements for AC of the phantom (B).

All post-processing and data reconstructions of the PET data along with the AC  $\mu$ maps of the table, the cylindrical phantom and the custom  $\mu$ map of the RF head coil were performed offline (Figure 4A) using a specialized vendor-provided software (e7 tools, Siemens Molecular Imaging, Knoxville, USA).

The PET data imaging matrix was  $344 \times 344 \times 127$  with a voxel size of  $2.08 \times 2.08 \times 2.03 \text{ mm}^3$ . These parameters follow the standard 3-dimensional ordinary Poisson ordered-subsets expectation maximization (3D OP-OSEM) with three subsets and 21 iterations reconstruction parameters of the PET/MR hybrid system. For a full reconstruction of the PET data, the hardware AC map of the patient table is added. Furthermore, the CT-based 3D template model of the phantom is added (Figure 6B). The CT-based  $\mu$ map of the RF head coil is added as a custom  $\mu$ map. The real position of the RF coil on the patient table is mechanically fixed. Hence, the  $\mu$ map position during the PET data reconstruction process is linked with the known position of the RF coil on the patient table, which is a precondition to obtain accurate results in attenuation correction.

The reconstruction of the second setup contains the CT-based  $\mu$ map of the phantom and the automatically added patient table. Since the RF coil was removed in this case (Fig. 7A), its  $\mu$ map is not used for the attenuation calculation (Figure 7B). The resulting  $\mu$ maps of the two reconstructed data sets are then evaluated in terms of their difference, since any signal level changes should result from the presence of the local RF coil due to the otherwise unchanged setup.

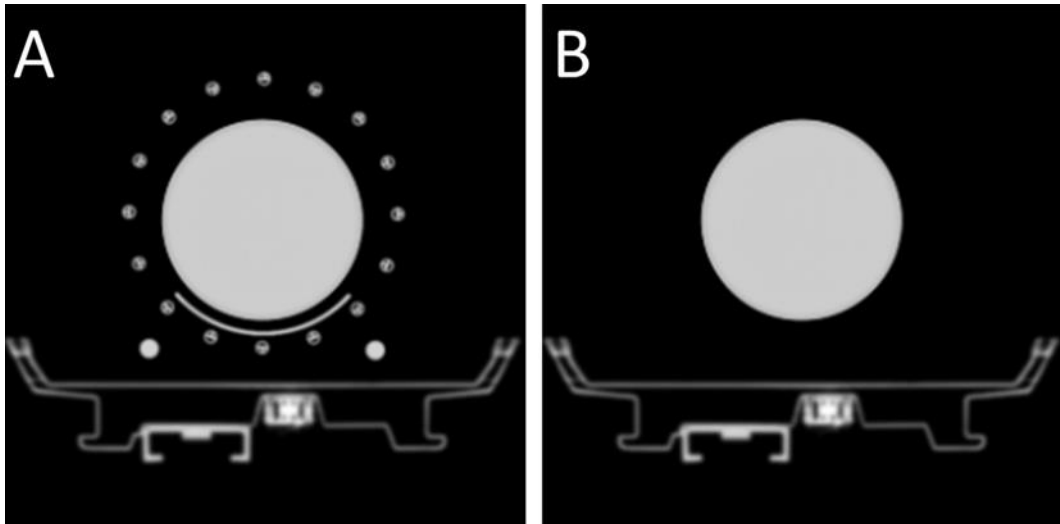


**Figure 7:** Combined hardware  $\mu$ maps for attenuation correction in the phantom experiments. CT-based  $\mu$ map of the RF head coil combined with CT-based  $\mu$ map of the water phantom and patient table (A). To provide a reference for difference measurements, a setup is measured where the RF coil is removed but the patient table and the phantom are attenuation corrected (B).

### **Patient measurements**

Seven patients were examined with the dual-tuned quadrature driven  $^{13}\text{C}/^1\text{H}$  head coil. Six patients underwent a hybrid PET/MR  $^1\text{H}$  examination, whereas patient #7 was scanned with the  $^{13}\text{C}$  option. PET/MR hybrid imaging using  $^1\text{H}$  MR and  $^{18}\text{F}$ -FDG as PET-radiotracer was performed on six patients (4 male, 2 female; 68 years  $\pm$ 6 years; 168 cm  $\pm$ 16 cm; 71 kg  $\pm$ 11 kg; 285 MBq  $\pm$ 50 MBq; 3 h 16 min post injection  $\pm$ 46 min). The patient characteristics are provided in Table 2.

For simultaneous PET and MR imaging two sequences were acquired: first, a Dixon-VIBE sequence with subsequent tissue segmentation provides the soft tissue  $\mu$ map for attenuation correction of the head region; second, a transversal T2-weighted TIRM dark fluid sequence (FLAIR) provides anatomical  $^1\text{H}$  MR imaging with higher spatial resolution. The two MR sequences had following parameters Dixon-VIBE: FOV 500  $\times$  500 mm<sup>2</sup>, image matrix 192  $\times$  192; spatial resolution 2.6  $\times$  2.6 mm<sup>2</sup>; slice thickness 3.12 mm; TR 3.6 ms, TE1 1.23 ms and TE2 2.46 ms; flip angle 10°. The parameters of the FLAIR sequence were: TR 4480 ms, TE 60 ms, TA 45 sec, slice thickness 2.0 mm, FOV 340  $\times$  340 mm<sup>2</sup>, matrix 256  $\times$  256, FA 89°, acceleration factor 3 (GRAPPA).

To enable PET difference measurements, patient measurements were performed twice; each PET/MR measurement lasted 3 minutes. Accordingly, the first measurement was performed with the RF coil mounted at the head end of the patient table, surrounding the head of the patient. Subsequently, the RF coil was removed from the patient table and thus from the FOV of the PET detector to provide a second PET measurement without

attenuation due to the RF coil. In this case, the built-in RF transmit/receive body coil of the PET/MR served as receiver coil for the MR sequences. For this second measurement, the head of the patient rested on a low attenuating pillow to achieve a similar position as in the first measurement when using the RF head coil. Thus, it was ensured that differences in the head positions between the two exams are minimized. Residual spatial differences (shifts or rotations) of the PET data sets were compensated by co registration using Vinci (Vinci Version 4.63, Max-Planck-Institute for Metabolism Research, Cologne, Germany). The comparison between the two setups was computed using a customized program, written in MatLab to depict the relative difference, caused by the attenuating RF coil.

Attenuation correction in the first setting with the RF head coil in place was performed using a three-component AC map during PET data reconstruction (Figure 8A). For the second patient setting without RF head coil in place, the AC map of the RF head coil was removed from the PET data reconstruction (Figure 8B).

**Table 2:** Patient data

Patient	Sex	Age [years]	Size [cm]	Weight [kg]	BMI [kg/m <sup>2</sup> ]	<sup>18</sup> F-FDG Activity [MBq]	time post injection [min]
#1	F	62	153	69	29,5	235	138
#2	F	75	168	60	21,3	284	144
#3	M	67	184	82	24,2	335	178
#4	M	64	180	79	24,4	299	137
#5	M	66	176	77	24,9	315	152
#6	M	75	181	77	23,5	278	231

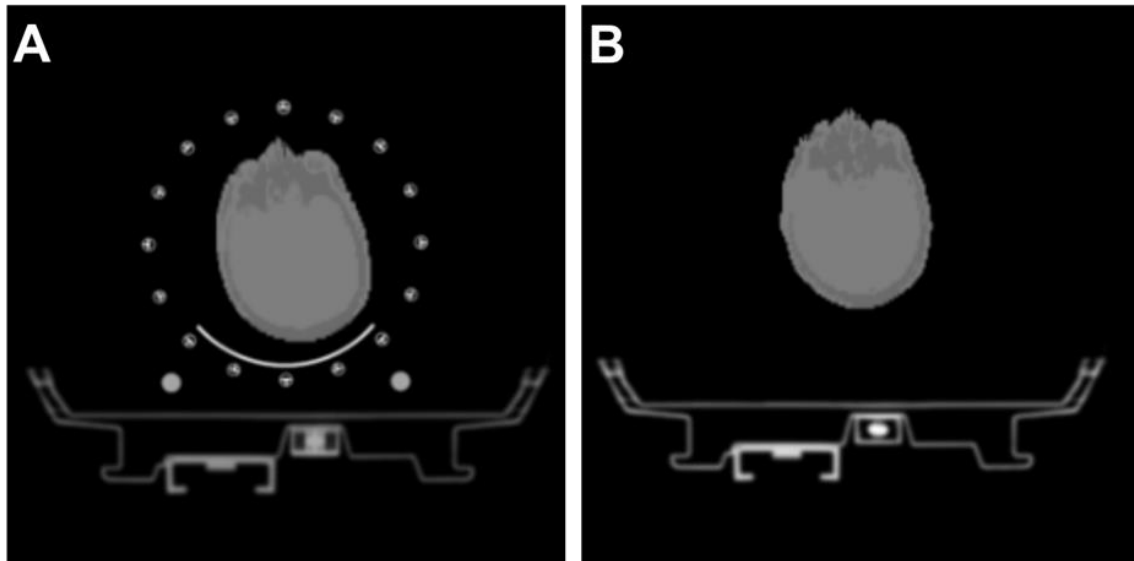


**Figure 8:** Attenuation correction  $\mu$ maps reflecting two setups for the patient measurements. The complete  $\mu$ map in (A) shows the experimental setting for patient measurements with the RF head coil in place. The  $\mu$ map in (B) shows the setting for the reference measurement without the RF coil.

The matched and co-registered patient PET data sets were reconstructed applying the individual  $\mu$ map, and the relative difference between the two PET data sets was calculated. The relative differences are a measure of the photon attenuation caused by the dual tuned RF head coil. Overall image quality of MR, PET, and PET/MR hybrid images was independently evaluated by two experienced readers (physicist and neurologist, each 20 years of MR and 8 years of PET/MR experience). In MR images, overall signal homogeneity, soft tissue contrast and image quality were subjectively rated. In PET images, signal homogeneity, and spatial detail of tracer distribution were subjectively rated. All MR and PET images were additionally inspected for artifacts.

The dual-tuned quadrature driven  $^{13}\text{C}/^1\text{H}$  RF head coil enables  $^{13}\text{C}$  MR imaging and MR spectroscopy. Therefore, one additional patient (patient #7) was scanned with the  $^{13}\text{C}$  option and a  $^{13}\text{C}$  spectrum of the whole brain was acquired using a free-induction decay (FID) sequence. A hard rectangular  $100\ \mu\text{s}$  excitation RF pulse of was used to achieve a flip angle of  $90^\circ$ . There was a  $100\ \mu\text{s}$  delay between excitation and acquisition, TR was chosen to be 1500 ms along with 206 averages, receiver bandwidth 5000 Hz, two-step phase cycling, resolution 2048 points, which resulted in an acquisition time of approximately 5 minutes. Dual-echo GRE shimming was used in order to optimize  $B_0$  homogeneity and the obtained peak line-width [McGinnity et al. 2016].

## Materials and Methods Study 3

### ***PET/MR hybrid system***

All phantom and patient measurements were performed on an integrated PET/MR whole-body hybrid imaging system (Biograph mMR; Siemens Healthcare GmbH, Erlangen, Germany), which allows for simultaneous PET and MR imaging. The PET detector consists of eight detector rings of 56 detector blocks each. One detector block is divided into 8 x 8 lutetium oxyorthosilicate (LSO) scintillator crystal elements read out by 3 x 3 avalanche photodiodes (APDs). The PET detector is fully integrated, therefore it is positioned between the gradient coil and the build-in transmit RF body coil of the MR system. The MR system contains an actively shielded 3.0 Tesla superconducting magnet with a total system length of 199 cm and a patient bore diameter of 60 cm. The gradient system for spatial encoding of the MR signals provides a maximum amplitude of 45 mT/m and a maximum slew rate of 200 T/m/s [Delso et al. 2011; Quick 2014].

### ***PET/MR breast imaging RF coil***

The 16-channel breast array RF coil in this work was developed in close collaboration with Rapid (Rapid Biomedical GmbH, Rimpar, Germany) and was designed for use in integrated whole-body PET/MR hybrid systems (Figure 9). This work reflects a further development of the 16-channel prototype RF breast coil and work presented by Dregely et al [Dregerly et al. 2015]. Our developments specifically include design changes of the coil housing, choice of different materials, relocation of electronic components outside of the PET-FOV, and development of a spacer frame to provide an accurate position of the RF coil on the patient table. These developments, which are described in the following in more detail, have led to the final product status of the 16-channel RF breast coil described in this work.

For optimized MR imaging performance, the individual RF coil loops are arranged in cylindrical shape such that seven RF loop elements per side cover the volume of each breast and provide homogeneous signal penetration depth into the breast volume. The eighth loop coil element on each side is placed in coronal orientation on top of the other RF coil elements within the coil housing to provide optimized signal penetration depth into the chest wall. The multi-channel RF setup allows for accelerated MR data acquisition using parallel imaging with the GRAPPA method [Griswold et al. 2002].

For optimized PET transparency the RF coil housing is constructed from low attenuating thin walled plastics (polyamide, PA2210 FR, manufacturer EOS) using large diameter radii in the housing design, thus inherently preventing high attenuation of PET signals. All stronger attenuating electronic RF components (pre-amplifiers, ceramic

capacitors, cable RF baluns, etc.) per design were located outside of the FOV of the PET detector. Although designed lightweight, the RF coil housing is rigid in its geometry and provides sufficient mechanical support for the patient lying head first in prone position on top of the RF breast coil. A plastic frame with 10 mm thickness was designed providing a defined and reproducible position of the RF breast coil on top of the PET/MR system patient table. This is a precondition to accurately match the position of the RF coil with the virtual position of its 3D attenuation template. Furthermore, the frame provides adjustable support for the patient forehead during the examination (Figure 9).

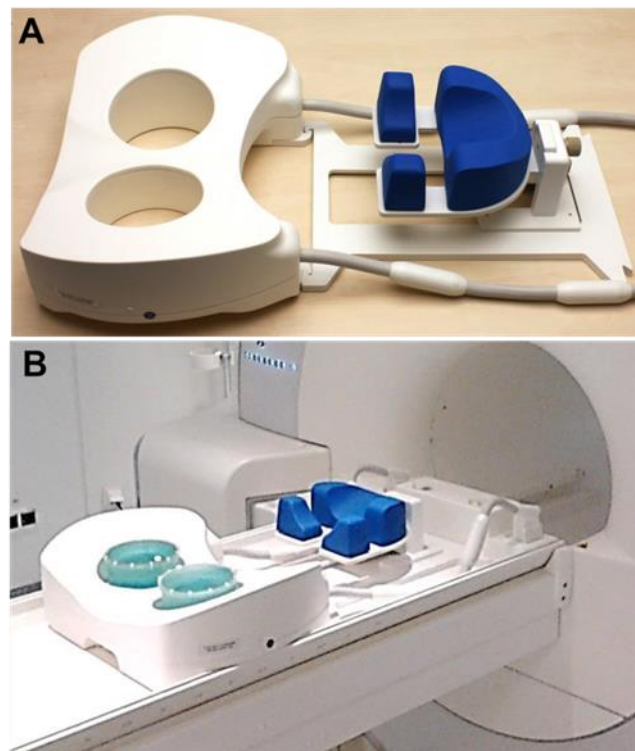


**Figure 9:** 16-channel RF coil designed for hybrid PET/MR breast imaging and the positioning frame to position the RF breast coil at a fixed position on the systems patient table (A). The frame also provides a head holder to support the forehead of the patients lying in prone position during the examination (A). The measurement setup with positioning device, breast RF coil and breast phantoms placed on the patient table of the hybrid PET/MR system (B).

### **Modular breast phantoms**

Modular breast phantoms were designed that allow for a systematic evaluation of MR, PET, and PET/MR imaging parameters [Aklan et al. 2013] (Figure 10). The two phantom domes simulate the shape of a female breast and are manufactured from polymethylmethacrylate (PMMA). The phantom domes are hollow and can be filled with MR signal-producing fluid (5 g NaCl per 1000 g distilled water and 3.75 g NiSO<sub>4</sub>), 1.31 l per phantom. For different

aspects of PET/MR performance tests, different modular inserts can be used (Figure 10) [Aklan et al. 2013].

MR-only measurements were performed using no inserts, which leads to homogenous MR images that can be used for signal-to-noise (SNR) evaluations (Figure 10A).

For evaluation of the spatial resolution in MR imaging, the breast phantoms were used with inserts produced from PMMA providing different high-resolution structures such as line patterns, hole arrays, line pair patterns and step wedges from 12 mm down to 0.2 mm spatial resolution [Aklan et al. 2013] (Figure 10B).

The combined PET/MR insert contains MR-visible structures and four glass spheres with different inner diameters of 10, 13, 17 and 22 mm, which can be filled with PET-visible radiotracer. The phantoms were filled with  $^{18}\text{F}$  radiotracer to achieve simultaneous PET/MR visibility of the phantom and the glass spheres simulating active lesions. The spheres were filled with an activity concentration of 46 kBq/ml and the background had a concentration level of activity of 5.75 kBq/ml, leading to a lesion-to-background ratio of 8:1 (Figure 10C).

For all PET quantification measurements involving phantoms, the two phantoms themselves were attenuation corrected by applying CT-based 3D template models and image registration in the PET data reconstruction as described below in more detail. The breast phantoms were designed with rather large volume (each 1.31 l) to also cover large volume breasts during the MR, PET, and PET/MR imaging experiments. This is important to assess the SNR and PET signal attenuation properties in the peripheral regions of the breast imaging volumes of the RF breast coil.

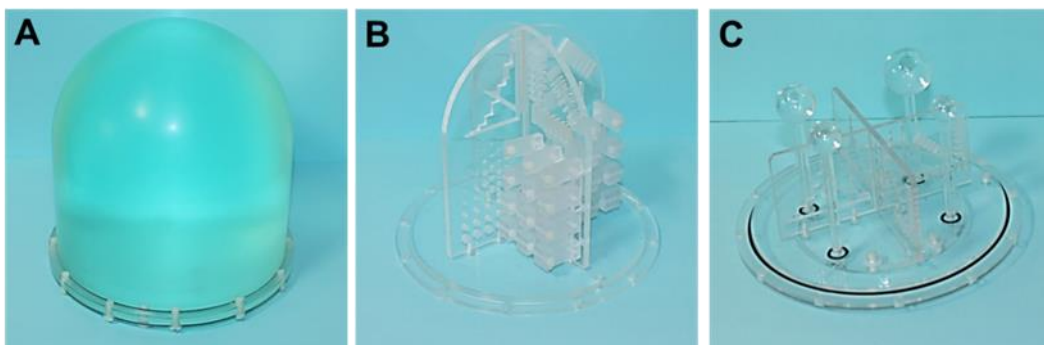


**Figure 10:** Modular breast phantom for evaluation of MR, PET and combined PET/MR imaging performance of the RF breast coil. (A) Dome-shaped phantom housing that can be filled with MR-visible phantom fluid and PET-visible radiotracer to provide a homogeneous PET/MR signal response across the phantom volume. (B) Insert with MR-visible structures for evaluation of high resolution MR imaging. (C) The insert for combined PET/MR imaging consist of high-resolution structures for MR imaging and four hollow glass spheres of different diameters, which can be filled separately with radioactive tracer.

### ***Attenuation and Scatter Correction***

The geometrically rigid design of the RF coil housing and its defined position on the PET/MR systems patient table provided by the positioning frame are preconditions for attenuation and scatter correction of hardware components using a CT-based template model of the RF coil during the PET data reconstruction process [Paulus et al. 2013; Aklan et al. 2013]. The positioning frame itself is placed outside the PET-FOV during single-station data acquisition and thus does not need to be corrected. To create an accurate and specific 3D AC template for the 16-channel PET/MR RF breast coil, CT scans were performed according to the established methods for 3D AC template generation including 3D CT imaging, signal thresholding, artifact removal, energy conversion from HU to LAC attenuation coefficients and subsequent Gauss filtering [Paulus et al. 2012; Paulus et al. 2013; Carney et al. 2006; Kartmann et al. 2013]. CT imaging was performed on a dual source CT scanner (SOMATOM Definition Flash, Siemens Healthcare GmbH) with following parameters: tube voltage 140 keV, tube current 500 mA, matrix size of  $512 \times 512$  pixels, voxel size  $0.3 \times 0.3 \times 0.6$  mm<sup>3</sup>. For converting CT data with an energy window level of 140 keV to the PET energy level of 511 keV, a bilinear conversion function was used [Paulus et al. 2013; Carney et al. 2006]. Thresholding of the 3D CT data was performed to remove CT beam hardening artifacts that otherwise assign AC values to air and will, thus, lead to systematic overcorrection. The last step in AC template generation was smoothing of the 3D CT data by applying a 4 mm Gauss filter [Paulus et al. 2013].

### ***Positioning accuracy***

To assess the positioning accuracy and reproducibility of the RF breast coil on the PET/MR systems patient table, markers were attached to the RF coil housing. Paulus et al. have suggested to use active <sup>68</sup>Ge rod sources as PET-visible coordinate system to determine the repositioning accuracy of hardware components in PET/M hybrid imaging [Paulus et al. 2014; Paulus et al. 2016]. In this study we used three MR-visible markers (cod liver oil capsule) firmly attached to the surface of the housing thus serving as MR-visible coordinate system (Figure 11).

The RF coil was placed on the PET/MR system table and fully removed and repositioned four times. The sequence for positioning measurement was a T1-weighted 3D fast low angle shot (FLASH), coronal slice orientation, FOV  $450 \times 170$  mm<sup>2</sup>, matrix size  $896 \times 336$ , 72 slices, slice thickness 1.0 mm, voxel size  $0.5 \times 0.5 \times 1.0$  mm<sup>3</sup>, TR 6.85 ms, TE 2.55 ms, flip angle 25°, six averages. Potential shifts in position of the three oil capsules for all three spatial dimensions (x, y, and z-direction) were determined by overlaying and measuring the resulting peak profiles of each oil capsule.

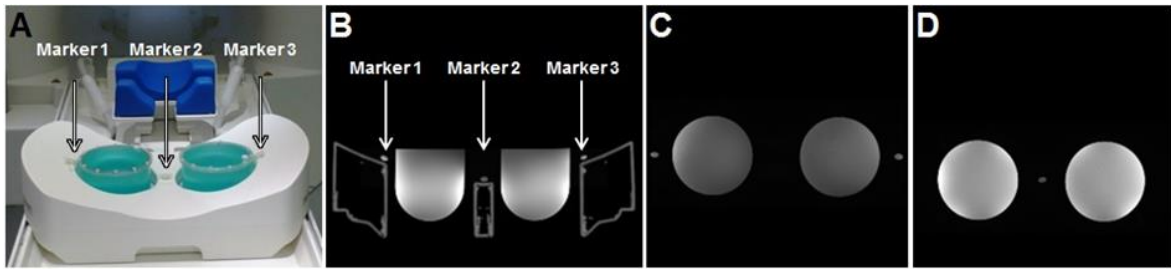


**Figure 11:** Measurement of the repeated positioning accuracy of the RF breast coil on the PET/MR systems patient table. The RF coil was marked with three cod liver oil capsules serving as MR-visible coordinate system (A). Image (B) shows the AC map of the RF coil overlaid with MR images providing the cod liver oil capsules as position markers as well as the two breast phantoms in axial orientation. This setup enables to quantify potential position shifts in x, y and z direction following repeated repositioning. Images (C-D) show the MR-markers and the two breast phantoms in two different coronal slices.

### **Phantom measurements**

MR-only SNR measurements were performed using the homogenous phantoms with no insert (Figure 10A) and the following MR imaging parameters: T1-weighted 3D fast low angle shot (FLASH), FOV  $400 \times 400 \text{ mm}^2$ , matrix size  $448 \times 448$ , 112 slices, slice thickness 1.5 mm, TR 6.04 ms, TE 2.46 ms, flip angle  $10^\circ$ . For high spatial resolution imaging, a T1 weighted 2D turbo spinecho (TSE) was acquired with FOV  $160 \times 160 \text{ mm}^2$ , matrix size  $512 \times 512$ , 20 slices with a slice thickness of 1 mm, TR 1780 ms, TE 15 ms, flip angle  $120^\circ$ . For SNR quantification, all phantom measurements with the FLASH sequence were acquired twice to create SNR maps across the entire phantom volume by using the difference method [Dietrich et al. 2007].

Evaluation of the spatial resolution in MR-only measurements was obtained with the modular high-resolution insert using the 2D TSE sequence described above.

To assess the attenuation due to the RF coil placed in the PET FOV and to evaluate and quantify the impact of the CT-based AC template model of the RF coil, PET phantom measurements were performed twice to result in difference measurements. 1. The RF coil with its frame was positioned on the PET/MR system table; the homogeneous breast phantoms were filled with radiotracer and acquired for 30 min in PET listmode data. 2. The RF coil was then removed without repositioning the phantoms and PET data were acquired once more. The second set of experiment was time-corrected considering the different starting points compensating the reduced activity due to decay of the radiotracer over time. The phantom difference measurements with and without RF coil in place provides quantification of the attenuation due to the RF coil. Furthermore, the difference measurements allow for validation of the hardware  $\mu$ map. The relatively long PET data acquisition times (30 min) and high activity concentration in phantom experiments using

homogeneous phantoms are needed to provide sufficient statistics to potentially assess even small attenuation differences of only few percent [Paulus et al. 2012; Kartmann et al. 2013]. Furthermore, as a necessity and for best possible accuracy in difference measurements, both breast phantoms have been included in CT-based AC to ensure AC of both, the phantom filling (water) and the phantom housing (Plexiglas). Here, MR-based AC alone is not sufficient since the phantom housing is not visible in MR imaging and thus not considered in MR-based AC, which would lead to a systematic attenuation bias in the experiments [Ziegler et al. 2013; Ziegler et al. 2015].

All PET data reconstructions using the generated AC map of the RF coil and of the breast phantoms were performed off-line with the PET/MR vendor's reconstruction software (e7 tools, Siemens Molecular Imaging, Knoxville, USA). Following image reconstruction, the PET imaging matrix was 344 x 344 x 127 with a voxel size of 2.08 x 2.08 x 2.03 mm<sup>3</sup>. The e7 software tools provides the hardware AC map of the PET/MR systems patient table, which is then added to the overall attenuation correction encompassing the patient table, the custom-generated CT-based AC template of the RF breast coil, and the MR-based AC of the patient tissues as provided by the Dixon VIBE sequence.

### ***Patient Measurements***

The study was conducted in accordance with all guidelines set by the approving institutional review board. Ten female patients (mean age 60 y  $\pm$ 20 y; mean BMI 26  $\pm$ 5), all diagnosed with local breast cancer, were imaged with the PET/MR system using the 16-channel RF breast coil and applying attenuation correction. The relevant patient statistics are provided in Table 3.

**Table 3:** Patient characteristics.

Patient	Age [years]	Size [cm]	Weight [kg]	BMI [kg/m <sup>2</sup> ]	<sup>18</sup> F-FDG Activity [MBq]	time post injection [min]	Type of malignancy
#1	69	150	60	26,7	110	89	Cancer, right breast with suspicion of contralateral, left sided breast cancer in the outer lower quadrant
#2	41	160	65	25,4	129	90	Breast Cancer in the outer lower quadrant.
#3	60	156	54	22,2	118	102	Multi centric breast cancer with lymph node metastases in the right axilla.
#4	76	166	78	28,3	135	63	Breast cancer in the upper outer quadrant with additional tumor in the axillar appendage
#5	52	165	80	29,4	141	101	Breast cancer; small seroma after lymphadenectomy left axilla.
#6	53	160	80	31,3	129	102	Quadrant exceeding, clip marked breast cancer left with multiple lymph node metastasis
#7	64	160	74	28,9	129	76	Breast cancer in the left outer lower quadrant with ipsilateral lymph node metastasis
#8	54	174	70	23,1	139	78	Quadrants exceeding breast cancer right in the outer quadrants with multiple lymph node metastases.
#9	80	165	67	24,6	135	78	Breast cancer in the upper left quadrant transition as well as a suspicion of tumor intramammilar
#10	42	160	53	20,7	137	54	Breast cancer in the left outer quadrant transition with cutaneous and interstitial edema

For high quality diagnostic MR imaging the following MR sequences were acquired in parallel to simultaneous PET data acquisition: 1. 3D Dixon-VIBE for patient tissue AC, 2. 2D T2-weighted TIRM, 3. 2D T2-weighted TSE, 4. 3D T1-weighted FLASH for dynamic contrast agent acquisition. Detailed MR imaging parameters are provided in Table 4.

**Table 4:** MR imaging sequence parameters of the diagnostic MR imaging protocol in patients. The table provides the values for the non-interpolated imaging matrix. Each of the five post-contrast injection phases in the T1-weighted dynamic FLASH sequence was acquired within 1 min 30 sec.

	Dixon VIBE	2D T2-weighted TIRM	2D T2-weighted TSE	3D T1-weighted FLASH dynamic
TR [ms]	3.6	4480.0	5420.0	7.1
TE [ms]	1.23; 2.46	50.0	77.0	2.7
TA [min]	0:19	0:45	2:21	1:30*6 = 9:00
Slice [mm]	3.12	2.0	2.0	2.0
FoV [mm <sup>2</sup> ]	500*500	340*340	340*340	400*400
Matrix	192*192	256* 256	640* 640	896*896
Flip angle	10°	89°	150°	25°
Acceleration	1	3	3	2

VIBE (volumetric interpolated breath-hold examination); TIRM (turbo inversion recovery magnitude); TSE (turbo-spin echo); FLASH (fast low-angle shot)

Patient tissue attenuation correction was performed with MR-based image segmentation from a Dixon-VIBE sequence [Martinez-Möller et al. 2009] as implemented by the vendor. In all patient examinations the MLAA option (maximum likelihood reconstruction of attenuation and activity) [Nuyts et al. 2013] was deactivated. The MLAA option derives patient contours from PET images to complete the potentially truncated MR-based AC map of the patient tissues. In this study we decided to deactivate the MLAA option to explicitly investigate the impact of the RF coil attenuation correction on PET quantification.

Hardware component attenuation and scatter correction of the patient table was performed automatically by the PET/MR system using an inherent attenuation template of this system hardware component [Quick 2014]. Difference images with and without attenuation correction of the RF breast coil were retrospectively reconstructed off-line by using the e7 PET reconstruction software. Quantification of lesion activity was performed by placing volumes of interest (VOI) across individual lesions and subsequent measurements of the maximum standard uptake values ( $SUV_{max}$ ).

Overall image quality of MR, PET and PET/MR hybrid images was evaluated by two experienced readers (one radiologist, ten years of MR and five years of PET/MR experience; one physicist, 20 years of MR and six years of PET/MR experience).

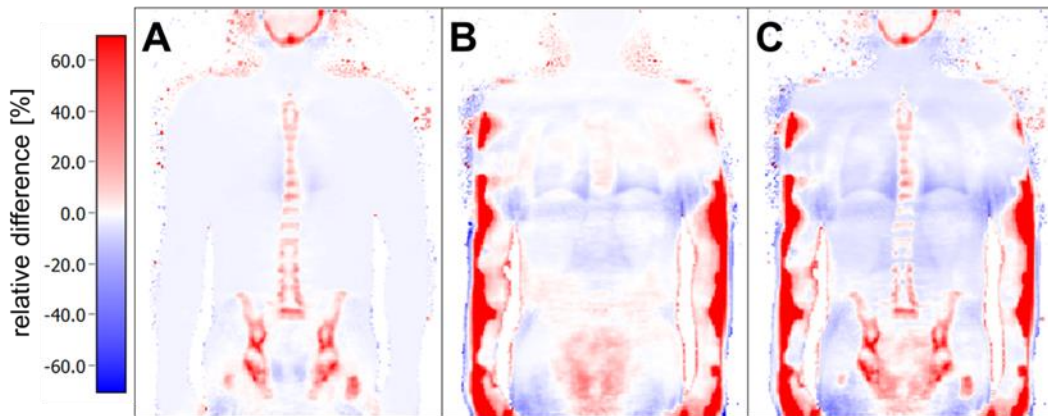
# Results

## Results Study 1

All 51 patients could be successfully examined with whole-body PET/MR and all  $\mu$ maps with the new features bone model and HUGE truncation correction of all patients could be successfully calculated.

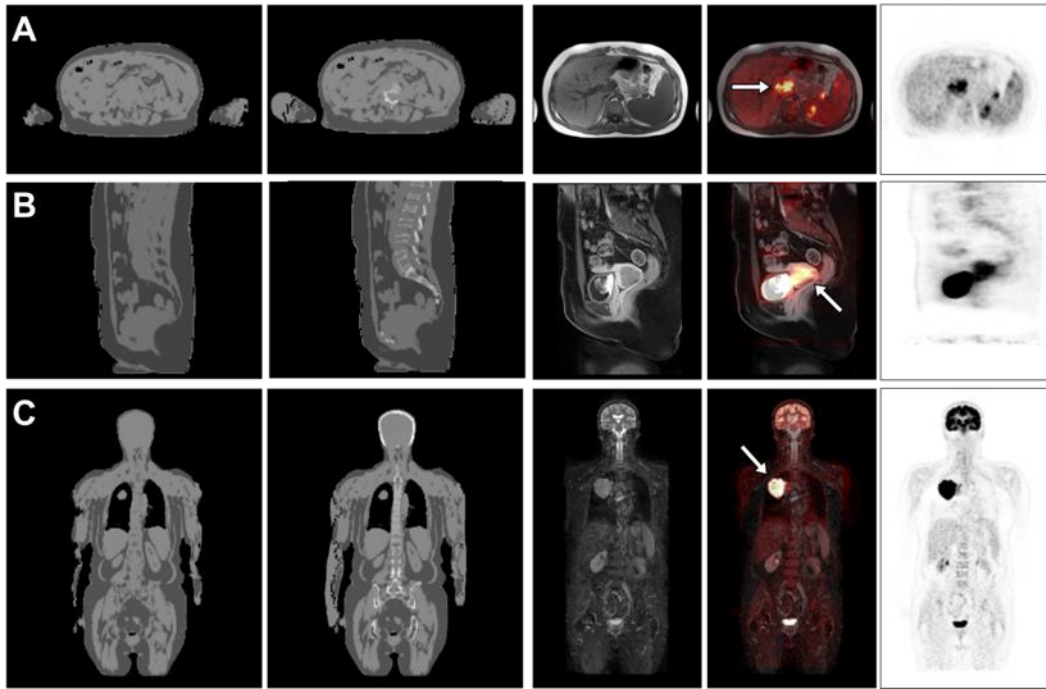
Calculated difference maps provide visual assessment of the quantitative impact of different  $\mu$ maps that were compared to the 4-compartment standard Dixon-VIBE  $\mu$ map serving as reference (Figure 12). Figure 12 for one patient data set exemplarily shows the quantitative impact of adding bone and HUGE truncation correction to the standard  $\mu$ map. Red regions along the arms and along the major bones indicate increased attenuation correction values in these body regions. Blue regions in the thorax and pelvic region, on the other hand, indicate the relative impact of improved scatter correction by a more consistent attenuation map.

In the 51 patients an overall number of 99 tumors and lesions could be well identified in all 204 (4\*51) reconstructed whole-body PET data sets, independent of the specific  $\mu$ map that has been used for attenuation correction of the PET data. None of the lesions was missed in any of the three AC PET data sets when compared to the PET data set reconstructed by Dixon standard AC. No additional lesions were found in any of the three AC PET data sets.



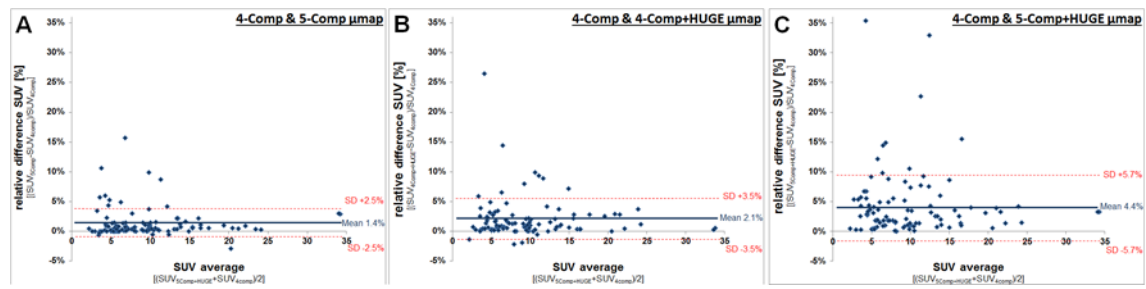
**Figure 12:** Calculated difference maps in coronal orientation providing the relative difference between new  $\mu$ map features (bone and truncation correction) compared to the reference MR-based  $\mu$ maps. The maps were calculated exemplarily for patient #22, lesions are not present in the selected images. The color bars provide the quantitative bias (in %) of relative undercorrection (red) or overcorrection (blue) when compared to the reference 4-compartment  $\mu$ map. (A) The relative difference between the 4- and 5-compartment  $\mu$ maps shows bone areas in red color, indicating higher correction factors in the bony regions. (B) Applying the HUGE method for truncation correction, adds red regions of higher relative attenuation correction factors along the arms to the difference maps. (C) Adding bone and truncation correction to the  $\mu$ map shows bony regions and arms in red, which were previously undercorrected. The blue regions in the thorax and pelvic region indicate the relative impact of improved scatter correction.

Figure 13 exemplarily shows three cases from the patient database and the respective setup with 4-compartment- $\mu$ map, 5-compartment- $\mu$ map with truncation correction, and MR and PET image data, respectively. The three Bland-Altman plots in Figure 14 show the relation between two  $\mu$ maps each; where on the x-axis the mean value of the two  $SUV_{max}$  of each PET active lesion is depicted. The y-axis of each correlation graph shows the relative difference of identical (congruent) lesions with the compared  $\mu$ map method: Fig. 14A 5-compartment with bone, Fig. 14B 4-compartment with HUGE truncation correction, Fig. 14C 5-compartment with HUGE truncation correction.



**Figure 13:** Exemplary patient cases to demonstrate (from left to right) reference 4-compartment and 5-compartment  $\mu$ maps plus HUGE truncation correction, MR, PET/MR, and according PET image data. (A) In patient #9 diagnosed with lymph-node-carcinoma, the measured  $SUV_{max}$  of the main lesion increases from 13.7 up to 14.1 (+2.9 %) in this example when comparing the PET data reconstructed with the 4-compartment- $\mu$ map to the PET data reconstructed with the 5-compartment- $\mu$ map plus HUGE truncation correction. (B) The  $SUV_{max}$  of the cervix-carcinoma in patient #19 increases from 14.3 up to 15.6 (+9.1 %) when comparing PET data reconstructed with both different  $\mu$ maps. (C) The  $SUV_{max}$  of the bronchial carcinoma in patient #17 increases from 33.7 up to 34.8 (+3.3 %) when using both  $\mu$ maps for PET data reconstruction.

Figure 14A depicts the influence of additional bone information; the mean  $SUV_{max}$  of all 99 lesions increases by 1.4 %  $\pm$ 2.5 % when comparing the 4-compartment- $\mu$ map with the 5-compartment- $\mu$ map. In figure 14B, the y-axis shows the relative difference when using the 4-compartment- $\mu$ map+HUGE. The mean  $SUV_{max}$  of all 99 lesions increases by 2.1 %  $\pm$ 3.5 % when comparing the 4-compartment- $\mu$ map with the 4-compartment- $\mu$ map+HUGE. In figure 14C, the  $SUV_{max}$  of the 4-compartment- $\mu$ map and the 5-compartment- $\mu$ map+HUGE is depicted. The mean  $SUV_{max}$  of all 99 lesions increases by 4.4 %  $\pm$ 5.7 % in total when using all additional information compared to the 4-compartment- $\mu$ map.



**Figure 14:** The three Bland-Altman plots correlate the measured  $SUV_{max}$  values of all 99 detected lesions each by comparing two different  $\mu$ map reconstructions. The x-axis provides mean  $SUV_{max}$  values from the  $\mu$ map with the new feature with the 4-compartment  $\mu$ map serving as reference. (A) Relative difference of  $SUV_{max}$  values of congruent lesions reconstructed with the 5-compartment  $\mu$ map including bone vs. the 4-compartment standard  $\mu$ map. (B) Relative difference of  $SUV_{max}$  values of congruent lesions reconstructed with the 4-compartment  $\mu$ map including HUGE truncation correction vs. the 4-compartment standard  $\mu$ map. (C) The relative difference of  $SUV_{max}$  values of all lesions for the 5-compartment  $\mu$ map plus HUGE truncation correction vs. the 4-compartment standard  $\mu$ map. An overall trend towards higher  $SUV_{max}$  due to adding bone and HUGE truncation correction to the  $\mu$ maps can be observed.

Table 5 provides clustered results of all 99 lesions. Lesions in this table were grouped according to their location in respective body regions. While the overall quantitative impact on the sum of all 99 lesions on average was small, single lesions showed a significant increase of  $SUV_{max}$ , depending on their respective location. The highest increase of  $SUV_{max}$  by adding bone AC information on average is achieved in bone lesions with +4.3 %. The lowest increase can be observed in lesions located in the abdominal region with an average gain of +0.1 %. The highest  $SUV_{max}$  gain in a local lesion when adding the bone model to the  $\mu$ map was measured in a bone lesion located in the os ischii with +15.7 %.

The highest increase of  $SUV_{max}$  by adding the HUGE AC information in average was found in the pelvic region with +4.2 %, the lowest increase in  $SUV_{max}$  was found in lesion in the head region, with an average gain of +1.2 %. For an individual lesion, the highest  $SUV_{max}$  increase by +26.5 % was found for an iliac lymph node by adding HUGE truncation correction. This lymph node located in the pelvic region also showed the highest overall increase when adding bone and HUGE with a  $SUV_{max}$  maximum increase of +35.4 % (Table 5). The pelvic region also showed the highest average gain of  $SUV_{max}$  with +6.7 %, whereas the abdominal region showed the lowest average gain with +2.8 %.

Location	No.	4-comp vs. 5-comp				4-comp vs. 4-comp+HUGE				4-comp vs. 5-comp+HUGE						
		Mean value rel. Diff. [%] 4-comp vs. 5-comp	Min. Diff. [%]	Max. Diff. [%]	Regression gradient	Correlation Coefficient coefficient of determination	Mean value rel. Diff. [%] 4-comp vs. 4-comp+HUGE	Min. Diff. [%]	Max. Diff. [%]	Regression gradient	Correlation Coefficient coefficient of determination	Mean value rel. Diff. [%] 4-comp vs. 5-comp+HUGE	Min. Diff. [%]	Max. Diff. [%]	Regression gradient	Correlation Coefficient coefficient of determination
<b>Head-neck region</b> (including thyroid lesion, axilla & supraclavicular lymph nodes etc.)	25	0.65 ± 1.01	-0.58	4.39	1.0096	0.9999 0.9997	1.20 ± 2.12	-1.38	9.86	1.0130	0.9990 0.9980	2.97 ± 4.39	0.10	22.68	1.0253	0.9959 0.9917
<b>Thorax region</b> (including bronchial carcinoma, mammary carcinoma, mediastinal lymph nodes etc.)	35	1.04 ± 1.41	0.0	6.04	1.0228	0.9998 0.9997	1.99 ± 3.02	-1.88	14.43	1.0103	0.9994 0.9987	4.51 ± 5.98	0.0	32.93	1.0350	0.9967 0.9934
<b>Abdominal region</b> (including liver and kidney lesions, abdominal lymph nodes etc.)	13	0.12 ± 0.93	-2.86	1.08	0.9882	0.9997 0.9993	2.29 ± 1.86	0.67	7.99	1.0148	0.9996 0.9992	2.75 ± 1.92	0.67	8.32	1.0192	0.9995 0.9990
<b>Pelvic region</b> (including cervixcarcinoma, rectal lymph nodes etc.)	16	2.37 ± 2.74	-0.56	10.58	0.9994	0.9994 0.9989	4.21 ± 6.13	0.2	26.46	0.9991	0.9979 0.9958	6.70 ± 8.04	0.40	35.38	1.0020	0.9970 0.9940
<b>Bone lesions</b> (including vertebral body lesions, pelvic lesions etc.)	10	4.34 ± 5.07	0.0	15.71	1.1184	0.9908 0.9816	1.29 ± 2.14	-2.14	5.96	0.9763	0.9988 0.9976	6.06 ± 4.9	0.38	14.92	1.0930	0.9910 0.9821
<b>Total</b>	<b>No.</b> 99	<b>Mean ± SD</b> <b>1.37 % ± 2.51 %</b>					<b>Mean ± SD</b> <b>2.12 % ± 3.52 %</b>					<b>Mean ± SD</b> <b>4.40 % ± 5.74 %</b>				

**Table 5:** Quantitative results of all 99 identified lesions that were clustered according to their location in respective body regions. The three columns provide the measured relative differences of PET data reconstructed with different  $\mu$ maps (4-compartment plus bone, 4-compartment plus HUGE, 5-compartment plus HUGE). The 4-compartment  $\mu$ map here served as reference. Note that, overall, only few percent relative differences were found for all lesions. However, large deviations up to 35 % were found for single lesions, depending on their location and on the respective attenuation correction method. The regression-curve gradient showed an increase of  $SUV_{max}$  in most body regions and lesions, furthermore, the correlation coefficient ( $r$ ) and the coefficient of determination ( $r^2$ ) are indicators for excellent correlation between the attenuation correction methods.

## Results Study 2

### ***Phantom measurements***

Figure 15 shows the relative PET difference maps of the cylindrical emission phantom in all three spatial directions. Differences between the two PET scans are visualized according to the following definition:

$$\text{Eq. 5} \quad \textit{relative difference maps} = \frac{PET_{with\ coil} - PET_{without\ coil}}{PET_{without\ coil}}$$

Figure 15A depicts the relative difference between the PET measurement where the RF coil is placed in the PET FOV and the corresponding case without any RF coil (reference scan). The mean difference in relative activity is  $+8.82\% \pm 0.38\%$ , reflecting the overall attenuation caused by the RF head coil. The local differences across the phantom volume range from 1% up to 25%. The highest local difference is found in the lower region of the RF coil close to the patient table where the head-neck support cradle causes highest attenuation. The open coil space near the upper birdcage rungs causes less attenuation in the upper regions of the phantom volume.

Figure 15B shows the relative difference results of the two PET measurements with and without the RF coil in place, after applying the attenuation correction  $\mu$ map of the RF coil. Thus, Figure 15B shows the attenuation correction influence of the CT-based  $\mu$ map of the RF coil. The white, light red and light blue colors in the difference maps indicate a successful attenuation correction. Light red regions show a slight under-correction, light blue areas indicate a slight over-correction mostly caused by statistical noise.

Figure 15C shows the measured mean value of 75 ROIs in z-direction over 150 mm of the phantom (stack of green ROIs in coronal view). The non-attenuated-corrected ROI (red graph) varies around  $+8.82\% \pm 0.38\%$ . The AC ROI (blue graph) varies around  $0.96\% \pm 0.29\%$  which demonstrates successful attenuation correction.

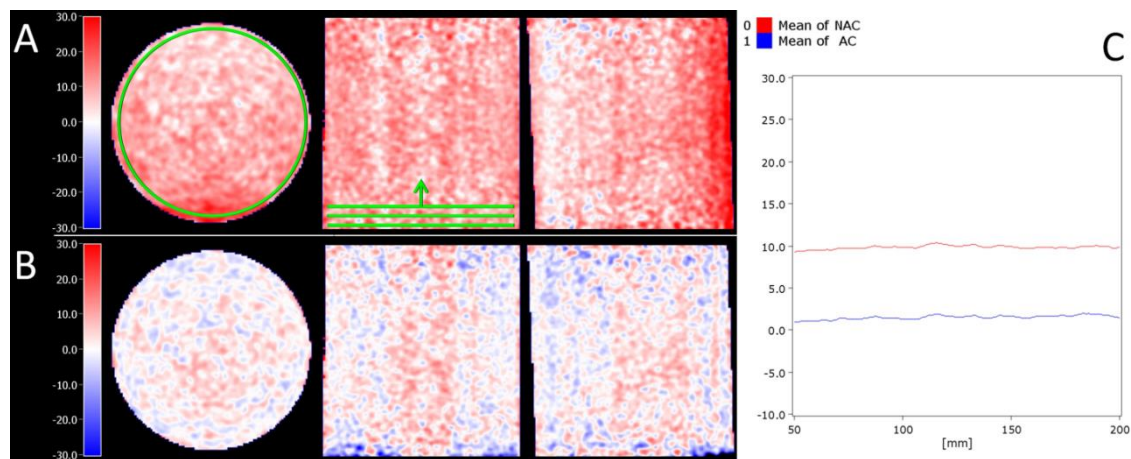


**Figure 15:** Relative difference maps comparing two phantom measurements with/without RF coil placed in the field-of-view of the PET detector during PET data acquisition (A). Local attenuation caused by the RF coil in the phantom is up to 25 % (red areas in lower phantom region (A)). Applying CT-based attenuation correction of the RF coil results in a reduced quantification bias, thus reducing the differences to the PET measurement without RF coil to almost zero (B). The graph in (C) provides mean difference values in % for (A) and (B). The mean difference value was measured in a large region of interest (ROI, green circle in (A)) in 75 slices along the longitudinal direction of the phantom (z-direction). The mean attenuation value caused by the RF coil is 8.8 % (red line), which decreases to a mean value of 0.96 % after applying attenuation correction for the RF coil (blue line).

### Patient measurements

Example MR, PET and fused PET/MR images of three patients are shown in Figure 16. The PET images are attenuation corrected with the MR-based AC patient  $\mu$ map, the CT-based AC of the systems patient table, and the custom-built AC for the RF head coil (Fig. 16B). The fused PET/MR images show anatomical information from the MR images, along with the radiotracer distribution from the PET acquisition (Fig. 16C). Overall image quality of MR, PET and PET/MR hybrid images was rated good to excellent and of diagnostic quality. MR signal homogeneity and image contrast on FLAIR images was rated excellent, image quality was not hampered by noise, and no artifacts were detected. In PET images, signal homogeneity and spatial detail of tracer distribution were rated good and of diagnostic quality despite the fact that the PET/MR exams were started with a significant delay time (3h 16min post injection  $\pm$ 46 min).

Figure 17 shows the PET images and difference maps of three representative patients. In these measurements, the average difference across all six patient PET measurements without RF coil (reference, Fig. 17A) and patient scans with non-corrected RF coil attenuation (Fig. 17B) of all six patients was measured to 5.17 %  $\pm$ 0.81 % (MEAN  $\pm$ SD), which is also visually indicated in Fig. 17C by the light red color scale.

The difference maps in Figure 17D visually indicates that all relative differences are close to around zero percent (white), reflecting successful attenuation correction of the RF head coil. Measurements across the brain PET images of all six patients determined the mean differences to the reference scans after RF coil AC to  $-0.87\% \pm 0.65\%$ . Figure 17E shows the mean value of the relative differences measured in all brain volumes along the axial axis. The mean values in these ROIs in all patients show a  $5.17\% \pm 0.81\%$  difference between PET data acquired without RF coil (reference) and with RF coil (without AC) as red curve. Following AC of the RF head coil, the mean difference values are  $-0.87\% \pm 0.65\%$  (blue lines).

The  $^{13}\text{C}$  spectrum of the non-selective brain scan as acquired in patient #7, demonstrates the functionality of the dual tuned RF head coil (C) providing a  $^{13}\text{C}$  spectrum with high signal-to-noise and narrow peak line-width (Fig. 18).

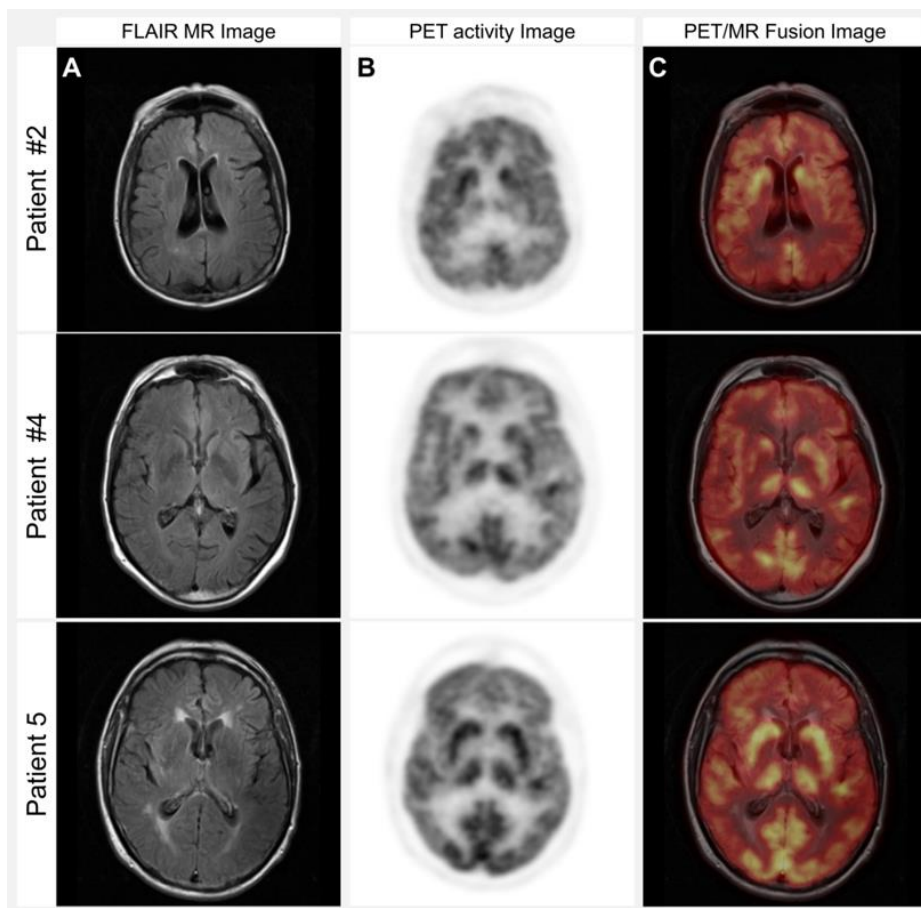


**Figure 16:** Examples for PET/MR hybrid imaging in three representative patients. Transversal view of MR images (FLAIR) (A) acquired with the  $^1\text{H}$  proton channel of the dual-tuned RF head coil. The MR images show good image quality and homogeneous signal distribution. Attenuation corrected PET-only images (B). Fused anatomical  $^1\text{H}$  MR and functional  $^{18}\text{F}$ -FDG PET images (C) showing excellent spatial coregistration.

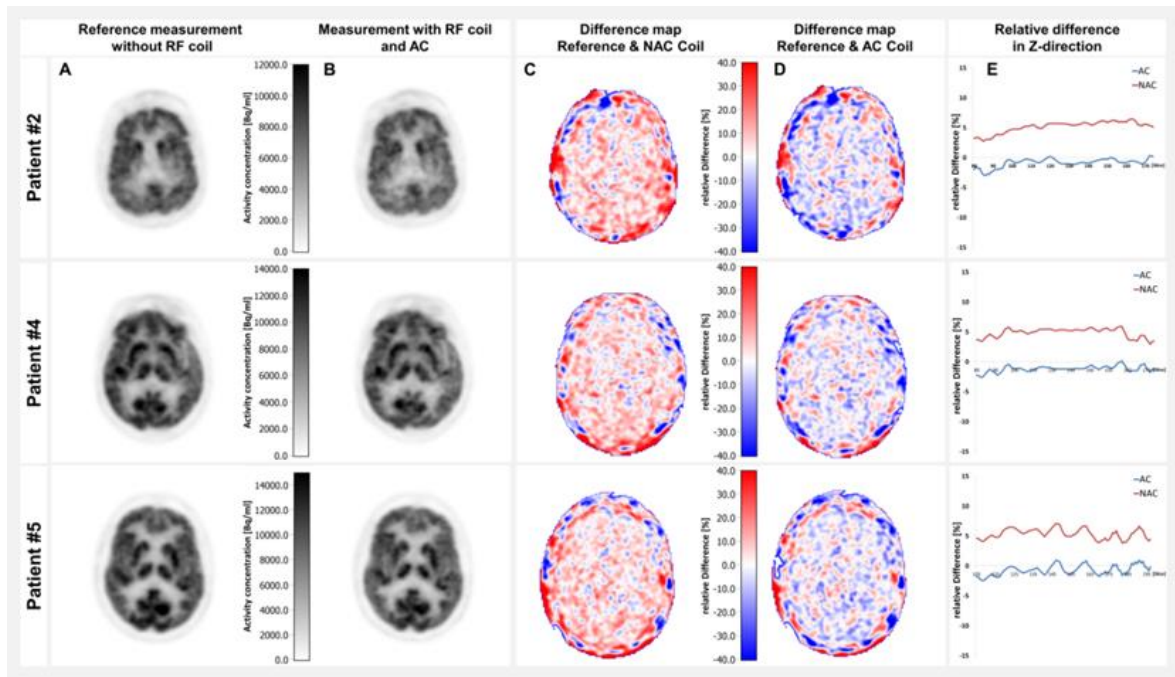


**Figure 17:** Impact of hardware component attenuation correction on PET quantification in patients. The PET images of three patient cases demonstrate the relative PET quantification bias caused by the RF head coil. Column (A) shows the transversal PET images of the reference measurement without RF coil serving as reference for quantification. Column (B) shows the PET images acquired with the RF head coil and after attenuation correction with the custom  $\mu$ map of the RF coil. Column (C) provides a relative difference map of the reference scan and the non-AC images, which shows a visual quantification bias around 10 % (light red color) and local visual differences up to 30 % (red color). Column (D) shows relative difference maps providing the difference between the references scan (PET images acquired without RF coil) and images acquired with the RF coil after attenuation correction. Averaged mean difference values across the transversal slices show a distribution around 0 % (white, light red and light blue color). The graphs in Column (E) show the averaged mean values of a stack of transversal slices in z-direction (feet-to-head direction), where a large ROI has been placed in each slice. The quantification bias for the non-AC images is around 5.1 % (red lines), while the bias is reduced to around -0.8 % following attenuation correction of the RF head coil (blue lines).

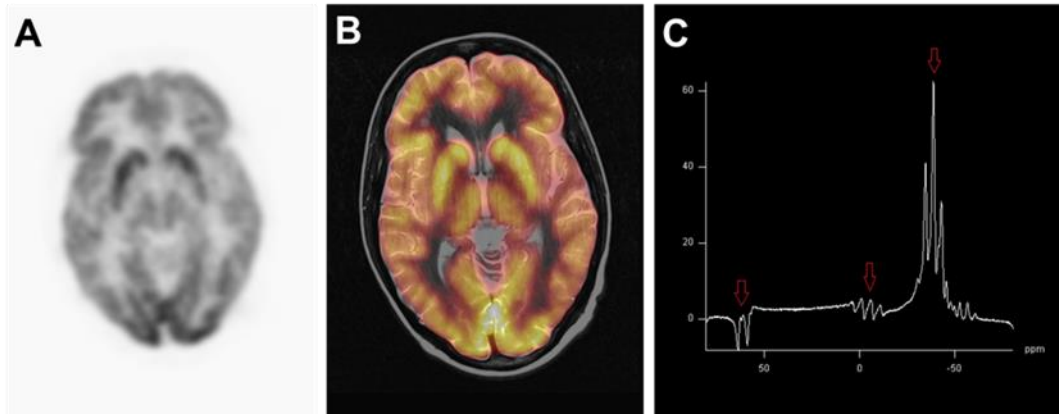


**Figure 18:** PET image of patient #7 (A) who was scanned with the  $^{13}\text{C}$  option of the double-tuned RF head coil. The fused PET/MR (B) image of the patient combines functional information provided by PET and anatomical information provided by MR (T2 TSE). The  $^{13}\text{C}$  spectrum of the non-selective brain scan, demonstrates the functionality of the dual tuned RF head coil (C) providing a  $^{13}\text{C}$  spectrum with high signal-to-noise and sharp peak line-width.

## Results Study 3

### ***Attenuation correction templates***

Figure 19 displays the resulting CT-based 3D attenuation correction template models for the RF coil and the two breast phantoms as well as the 3D template for the PET/MR system patient table. These 3D AC models were used for attenuation correction of the associated hardware components in the phantom and in the patient measurements.

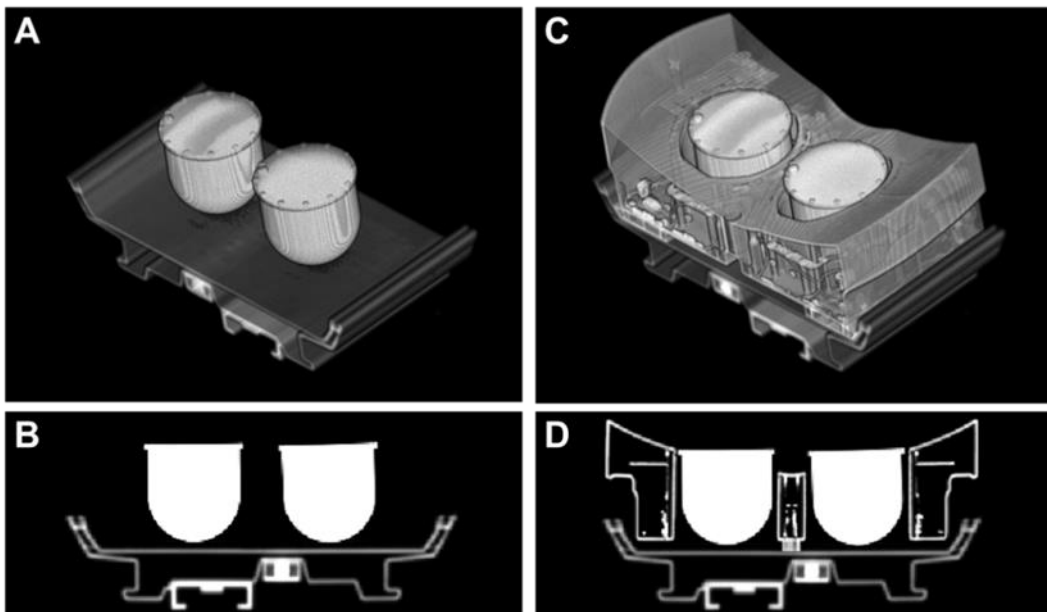


**Figure 19:** 3D CT-based template hardware component attenuation correction maps ( $\mu$ maps) of: (A and B) the patient table with two breast phantoms, and (C and D) with the 16-channel RF breast coil added. The 3D template model has been specifically generated for hardware component AC of the RF breast coil. Accurate positioning of the RF coil on the patient table using the positioning frame ensures perfect position match of RF coil and its AC template model. Note that the phantom holders are made from low attenuating Styrofoam and are, thus, not visible in images (A-D).

### ***Positioning accuracy***

The shape and rigid design of the RF breast coil housing in conjunction with the positioning frame ensured an accurate and reproducible repositioning of the RF coil with lower than 1 mm deviation in all three spatial dimensions as determined with repeated MR measurements using the cod liver oil capsules. Maximum deviations between the four repositioning measurements were determined to 0.8 mm in x-direction and 0.6 mm in z-direction. No deviation (0 mm) was detected in y-direction.

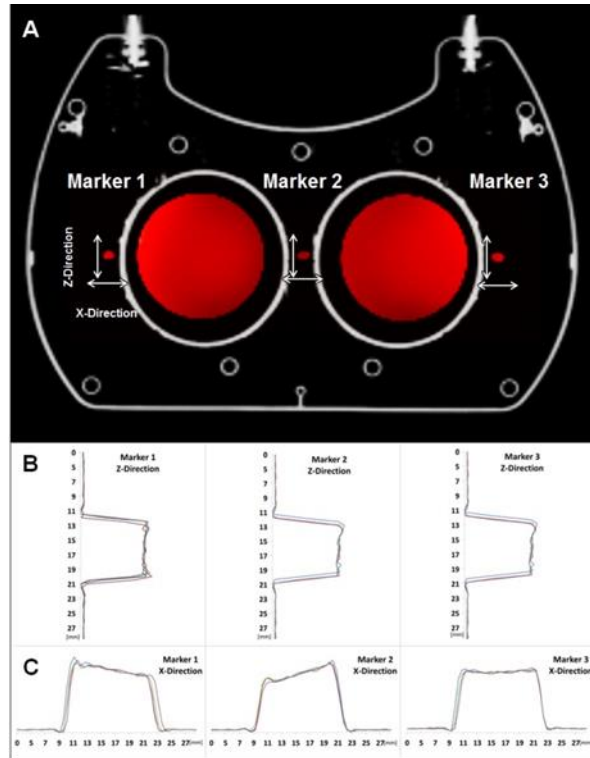


**Figure 20:** Image (A) shows the AC map of the RF coil fused with the MR-image, showing the two breast phantoms and the three MR-visible markers (red). The shift in z-direction was measured by placing line profiles and overlaying the individual peak profiles of each repeated measurement. Maximum difference between the profiles in z-direction was 0.6 mm (B). The maximum shift in x-direction was 0.8 mm (C).

## Phantom Measurements

### MR Imaging

For evaluation of the MR imaging performance the homogeneous breast phantoms were imaged twice with the clinical FLASH sequence to obtain SNR maps using the difference method [Dietrich et al. 2007]. The SNR maps quantify the signal penetration depth and signal homogeneity across the volume of the breast phantom for the MR imaging sequence used (Figure 21A, B). Highest signal is obtained at the midlevel of the phantom volume where the RF coil elements show maximum sensitivity and signal penetration depth.

Figure 21C-F shows the results of MR imaging with the high resolution 2D T1-weighted TSE sequence on the breast phantom with the insert featuring high-resolution structures. Water-filled structures are depicted bright while PMMA structures are displayed dark due to lack of MR signal. Fine structures down to 0.4 mm can be resolved for this combination of RF coil, breast phantom and MR imaging sequence.

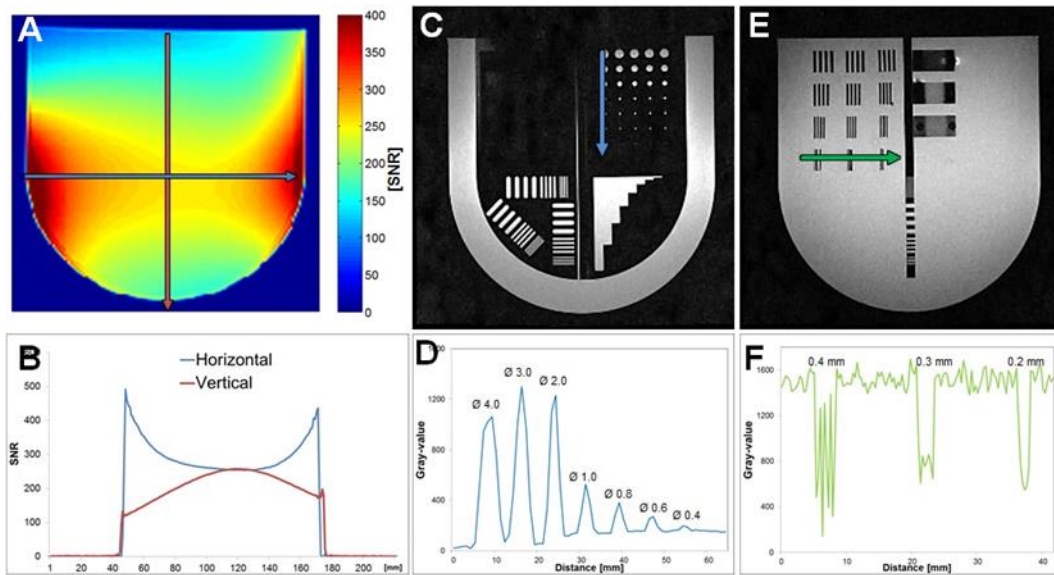


**Figure 21:** Quantitative MR-only measurements on the breast phantoms. SNR-scaled map for a central sagittal slice of one breast phantom that was generated for one phantom in axial view using the clinical FLASH sequence. (B) 1D profiles along the phantom region in vertical (red) and horizontal (blue) direction. (C) and (E) MR images were acquired with the high-resolution 2D TSE sequence. (D) A signal profile across bore holes with 4.0, 3.0, 2.0, 1.0, 0.8, 0.6, 0.4 mm diameter. (F) A signal profile across line pairs with 0.4, 0.3 and 0.2 mm providing visibility of structures down to 0.4 mm.

### PET Imaging

The relative difference images of the homogeneous breast phantoms in Figure 22 demonstrate the quantitative effect of placing the RF breast coil in the field-of-view of the PET detector.

In Figure 22A the relative difference between phantom PET measurements with and without the RF coil in place is shown. The mean difference in detected overall activity concentration across the phantom volumes is 13 % with local bias ranging from 0 % up to 24 % difference in peripheral phantom regions that are located closer to attenuating structures of the RF breast coil. Figure 22B shows the resulting difference between a measurement without and with RF coil in place, but this time after applying attenuation correction for the RF coil. Homogeneous greenish color across both breast phantoms indicates appropriate attenuation correction of the RF coil (Fig. 22B). The graphs in Figure 22C represent the overall difference bias across the breast phantom displayed along the z-direction. The upper curve shows the non-AC difference (12-14 %) values, while the lower curve shows the difference values following AC of the RF coil ( $\pm 0.5$  %).

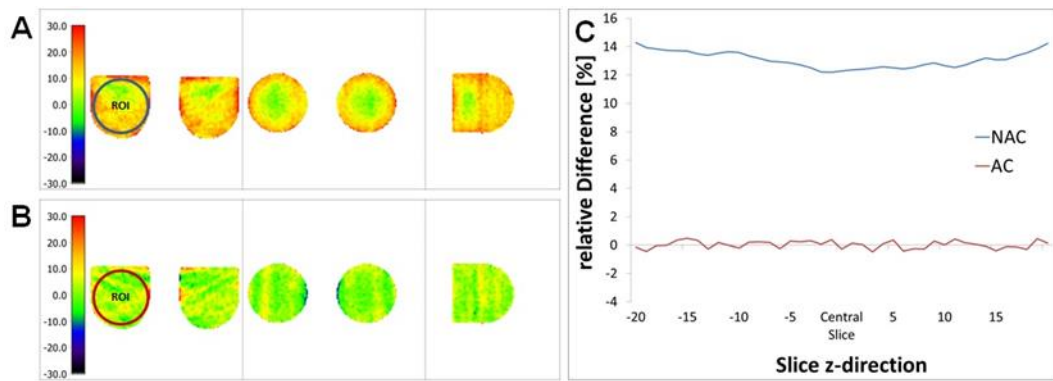


**Figure 22:** Difference PET images of the homogeneous breast phantoms in axial orientation. In (A) the breast phantoms were placed on the PET/MR system table, filled with activity and measured 1) without the RF breast coil, and 2) with the breast RF coil in place. (A) shows the resulting difference of both measurements indicating PET signal attenuation due to the RF coil components located in the PET field-of-view (yellow and red areas). (B) shows the resulting difference between an measurement without and with RF coil in place, but this time after applying attenuation correction for the RF coil. Homogeneous greenish color across both phantoms indicates appropriate attenuation correction of the RF coil (B). Result of an overview through 40 slices of the phantom in z-direction shows an average difference of 12-14 % without hardware component AC. Applying hardware component AC, the relative difference is reduced to  $\pm 0.5$  % (C).

### PET/MR Imaging

Figure 23 displays the results of the MR (Fig. 23A), PET (Fig. 23B), and PET/MR images (Fig. 23C) of the two breast phantoms in transversal (left), coronal (middle) and sagittal (right) orientation. In the MR-only image the glass spheres can be depicted as dark rims (Fig. 23A). The PET images show the tracer-filled glass spheres with a lesion-to-background activity ratio of 8:1 (Fig. 23B). PET/MR images show exact overlap of MR and PET image content in all three spatial dimensions (Fig. 23C).

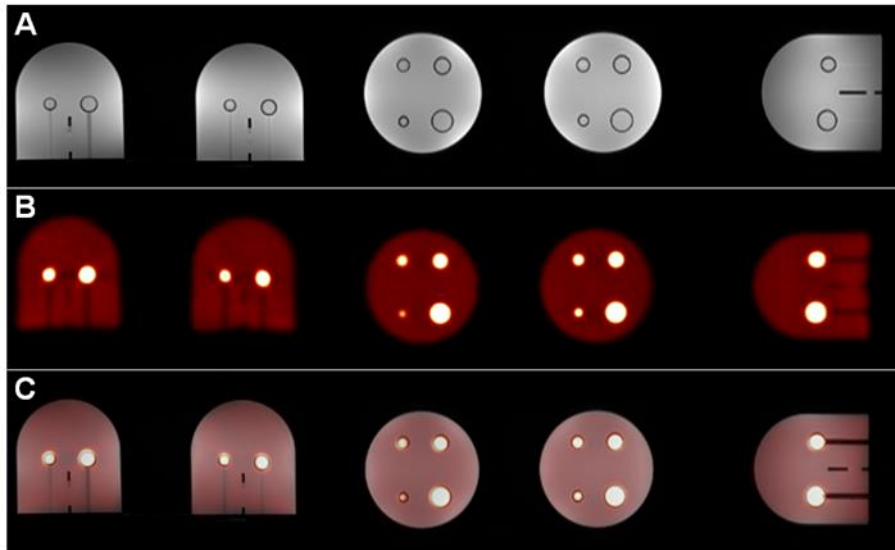


**Figure 23:** MR (A), PET (B) and PET/MR images (C) of the two breast phantoms in transversal (left), coronal (middle) and sagittal (right) orientation. In the MR-only image the glass spheres can be depicted as dark rims (A). The PET images show the tracer-filled glass spheres with a lesion-to-background activity ratio of 8:1 (B). PET/MR images show overlap of MR and PET image content (C) in all three spatial dimensions.

### **Patient Measurements**

All ten patients were successfully examined with PET/MR hybrid imaging using the 16-channel breast RF coil. All resulting MR, PET, and combined PET/MR images were rated with diagnostic image quality. Exemplarily for one patient, Figure 24A.1 and 24B.1 shows an example for a corrected patient PET data (Patient #7) with the components of the MR-based AC patient  $\mu$ map and the CT-based AC of the systems patient table. Figure 24A.2 and 24B.2 shows the overall resulting AC map consisting of three components: 1. the MR-based AC of the patient tissues provided by the Dixon-VIBE sequence, 2. the CT-based AC of the systems patient table, and 3. the AC for the RF breast coil developed in this work. Figures 25 and 26 show two example patient cases (Patient #4 and #10, respectively) of female patients presenting with PET-active breast cancer lesions.

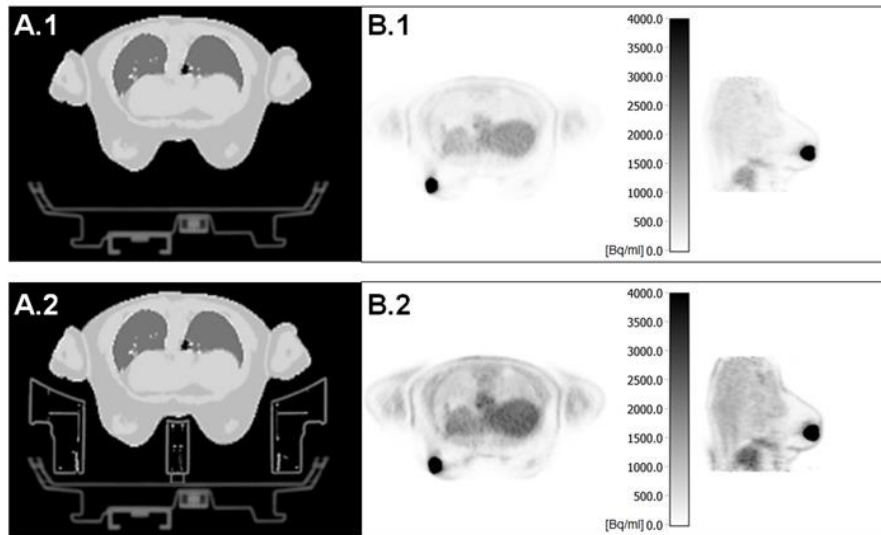


**Figure 24:** For an attenuation correction all  $\mu$ maps have to be fused. Without the CT-based hardware  $\mu$ map of the coil only the hardware  $\mu$ map of the patient table and the MR-based  $\mu$ map of the patient are included (A.1). For a complete AC the CT-based hardware  $\mu$ map is added (A.2). A PET image of a female patient (Patient #7) with a lesion without the customized CT-based  $\mu$ map AC (B.1) in comparison to the same patient data with full AC of the table, RF coil and MR-based patient  $\mu$ map (B.2).

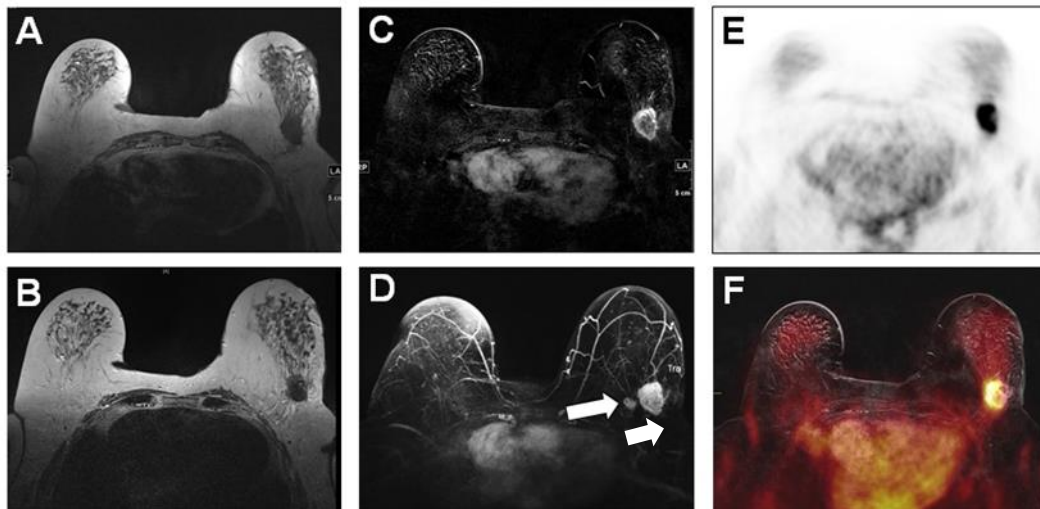


**Figure 25:** Example patient case of a 76 yrs. female (Patient #4) with initial diagnosis of invasive ductal carcinoma of the left breast. The T1-weighted (A), T2-weighted (B), and subtracted post-contrast T1-weighted image (C) clearly show the carcinoma in the left breast with fine detail. The subtracted post-contrast maximum-intensity-projection (MIP) in (D) shows the carcinoma and its vascularization. The thickness of the MIP (D) was chosen such that a second smaller tumor is also covered and visible in the left breast (arrow in (D)). The PET image (E) is attenuation corrected with all relevant  $\mu$ maps of the RF coil, patient tissues and PET/MR systems patient table. The PET/MR hybrid image (F) demonstrates exact fusion and display of the  $^{18}\text{F}$ -FDG -positive, carcinoma in the left upper outer quadrant.

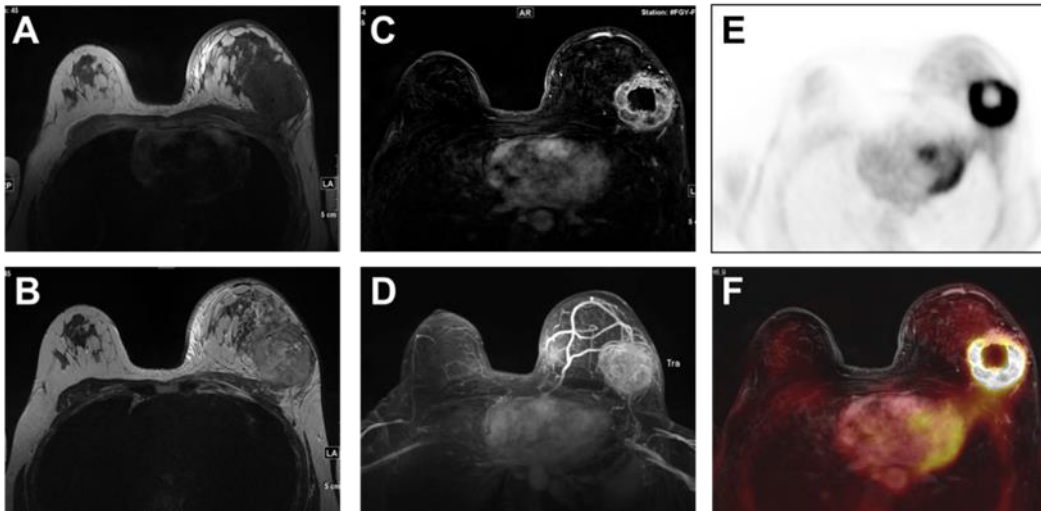


**Figure 26:** Example patient case of a 42 yrs female (Patient #10) with initial diagnosis of invasive ductal carcinoma of the left breast. The T1-weighted (A) and T2-weighted image (B) show a major diversification of the soft tissue in the left breast. The T1-weighted post-contrast subtraction image (C) and the MIP data (D) show the clear boundaries and vascularization of the tumor. The PET data (E) is attenuation corrected with all relevant  $\mu$ maps of the RF coil, patient tissues and PET/MR systems patient table. PET/MR hybrid imaging here shows a large, central necrotic PET-positive cancer in the outer quadrants of the left breast (F). Due to the massiv size of tumor tissue a donut-like shape of enhanced  $^{18}\text{F}$ -FDG -metabolism can be observed in the PET images (E and F). Only the outer parts of the tumor show enhanced metabolism, while the inner part is already necrotic. Perifocal edema and circular edema of the cutis is also noted leading to a size difference of both breasts.

MR Data acquisition was performed with the 16-channel PET/MR breast RF coil during simultaneous PET data acquisition. MR and PET image quality is excellent. All shown PET data was attenuation corrected with all AC map components shown in Figure 24.

Table 6 provides the evaluation of  $SUV_{max}$  values for all PET-active breast cancer lesions with and without applying AC of the RF coil. The overall mean increase difference in  $SUV_{max}$  for all eleven lesions is 11.8 %, respectively, when applying vs. not applying AC of the RF breast coil. This implies that applying the AC of the RF coil increases the measured SUV in breast lesions by 11.8 % which supports the phantom data where global (mean value) PET signal attenuation in the homogeneous breast phantoms due to the RF coil was determined to 12-14 %.

**Table 6:**  $SUV_{max}$  values of the patients

Patient	$SUV_{max}$		Difference $SUV_{max}$
	Non AC	AC	
1	11.695	12.095	3.3%
2	9.313	12.123	23.2%
3	8.094	9.475	14.6%
4	5.87	6.334	7.3%
	5.371	5.648	4.9%
5	9.374	9.979	6.1%
6	11.285	13.607	17.1%
7	16.616	20.603	19.4%
8	10.870	12.431	12.6%
9	3.369	4.115	18.1%
10	13.432	13.871	3.2%
<b>Mean Value</b>		<b>11.80%</b>	

Patient 4 has two separate lesions, which results in a total of eleven lesions

# Discussion and Conclusion

## Discussion and Conclusion Study 1

In this study, the impact of novel features in whole-body PET/MR attenuation correction on PET quantification was evaluated. Bone information and a method for truncation correction were both added to whole-body PET/MR attenuation correction. The impact on PET quantification was systematically investigated in a clinical study on 51 patients with 99 lesions. Four different attenuation correction maps were generated to reconstruct the non-AC PET data set of each patient four times. The widely used Dixon-based AC served as reference in this study and allowed for quantitative assessment of relative changes in lesion quantification.

Currently established methods for AC in whole-body PET/MR classify the attenuation of bone as soft tissue, thus leading to a systemic underestimation of the effective attenuation in bony regions [Beyer et al. 2016]. Applying the model-based method, the larger bones skull, spine, pelvis, and both upper femurs can be added [Paulus et al. 2015] to the patient  $\mu$ map. The addition of bone information does not require additional acquisition of MR data. Thus, acquisition time is not prolonged. The fast reconstruction time of a few seconds supports practicability in a clinical setting. The technique provided robust results, during the reconstruction of the  $\mu$ maps of all patients; no artifacts or misplacements of bone segments were observed. Accordingly, and intuitively, the  $SUV_{max}$  of bone lesions or lesions close to bone increases more than that of soft tissue lesions when adding bone attenuation to the  $\mu$ map. The results in this study have shown that consideration of the major bones in whole-body PET/MR AC provides reliable and accurate results for the vast majority of patient cases.

The current implementations of attenuation correction in PET/MR frequently show truncation of signal along the patient arms, thus leading to systemic underestimation of the effective attenuation along the body trunk [Beyer et al. 2016; Boellaard et al. 2015]. A widely used method for truncation correction in current PET/MR systems derives the outer contours of the patient from non-AC PET data to complement the truncated  $\mu$ maps [Nuyts et al. 2013]. In our study, we have applied the latest implementation of the MR-based HUGE method for truncation correction which has been suggested and evaluated earlier

[Blumhagen et al. 2013; Blumhagen et al. 2014]. The product version of HUGE in this study was combined with a continuously moving table strategy, thus providing improved and seamless contour detection for whole-body imaging. The HUGE algorithm only adds 2\* 65 seconds to the overall acquisition time of the whole-body PET/MR imaging protocol. Furthermore, applying the HUGE sequence does not add significant reconstruction time. In this study HUGE worked robustly and no signal voids or noticeable spatial deformations were observed in the 51 patients. The highest impact of HUGE on the  $SUV_{max}$  can be observed in the pelvic and thoracic region, due to the fact that the arms are fully depicted by the HUGE method. The effect of HUGE on the head neck region is negligible, due to the fact, that the truncated areas play a minor role in this body region.

Of note, the difference maps in Figure 12B, C also show blue regions in the body trunk, indicating a negative quantification bias in these regions when additionally applying HUGE truncation correction. This counterintuitive observation can be explained by the additional effect of HUGE on scatter correction. All  $\mu$ maps in PET/MR are used for both, attenuation correction and scatter correction. When applying truncation correction, tissue from the arms that attenuates and scatters PET signal is now considered in the  $\mu$ map and, thus, leads to a more consistent scatter scaling. Consequently, less scatter signal from the formerly truncated areas is detected in the body trunk, rendering blue regions in the difference maps (Figure 12B, C).

To put the results of the study in a clinical perspective it is important to note that none of the detected lesions was missed in any of the three AC PET data sets when compared to the PET data set reconstructed by Dixon standard AC. No additional lesions were found in any of the three AC PET data sets. Consequently, the visual impact of the new AC methods on reconstructed PET data sets was rather small but measurable. The overall and averaged quantitative impact of adding bone and truncation correction to the standard Dixon  $\mu$ map in whole-body PET/MR is reflected by the average gain of  $SUV_{max} + 4.4 \%$  for all 99 lesions measured. The majority of soft-tissue lesions are just slightly affected by the new features of attenuation correction (1.0 % - 2.0 %). This is an indicator for the overall efficiency and robustness of the 4-compartment MR-based AC for soft tissues, which can be considered as current standard for human  $\mu$ maps in PET/MR hybrid imaging. The true quantitative impact of improved attenuation correction can be appreciated, however, when evaluating single lesions that are located close to bone and/or close to truncations. In these cases, the difference can be relatively high, ranging from 10 % up to 35 % quantification bias, as measured for single lesions in this study. In these cases, accurate AC is very important. Also, accurate AC of all lesions, independent of their location within the body, is especially important for patients under treatment, where reproducible results in repeated PET/MR measurements is of high importance. The SUV in these cases

should be accurate, and ideally only depend on the treatment response, and not be variable due to AC and or different positioning of the patient in the PET/MR system.

This evaluation study did not concentrate on a specific patient collective; the only inclusion criteria were an indication for a whole-body PET/MR examination and injection with  $^{18}\text{F}$ -FDG radiotracer. It could be argued, that the number of included patients is rather small. However, with 51 patients and 99 lesions encompassing a broad range of body constitutions, patient sizes, and a variety of tumors and lesions, this first evaluation towards clinical practicability, robustness and quantification accuracy provides a solid basis for further application of the improved attenuation correction method in PET/MR. The study setup did not allow for an unbiased and independent comparison to another PET attenuation correction method. Such comparisons inherently would require a second patient scan introducing other dependencies and error sources such as scanning at different time points with quantitative effects on tracer distribution and, additionally would require different patient positioning. Instead, the Dixon-based AC method that is well established and evaluated in PET/MR [Beyer et al. 2016] served as intraindividual reference in this study. Fourfold repeated reconstruction of just one non-AC PET data set per patient, each time with using a different  $\mu\text{map}$ , allowed for a systematic and controlled evaluation of the novel  $\mu\text{map}$  features in relation to the established Dixon AC method.

## **Conclusion**

In summary, two novel features to improve the attenuation correction in whole-body PET/MR have been introduced and their individual impact on PET lesion quantification has been evaluated. Both features, bone correction and truncation correction, are fast and robust and thus are considered well applicable in a clinical setting. The study results demonstrate that the initial limitations of patient tissue AC in PET/MR are now overcome by additionally applying the two features for bone detection and truncation correction.

## Discussion and Conclusion Study 2

In this study a dual-tuned  $^{13}\text{C}/^1\text{H}$  RF head coil for integrated PET/MR neuroimaging was developed, implemented into a PET/MR system and evaluated. The RF head coil was designed for optimized PET transparency. Attenuation correction of the RF head coil was performed by generating and applying a dedicated 3D CT-based template  $\mu\text{map}$ . Attenuation correction was systematically evaluated in phantom experiments using a large-volume cylindrical emission phantom filled with  $^{18}\text{F}$ -FDG radiotracer. The PET/MR imaging performance and PET attenuation correction were then evaluated in six patients. The functionality of the dual-tuned  $^{13}\text{C}/^1\text{H}$  head coil was further demonstrated by generating  $^1\text{H}$  anatomical MR images and  $^{13}\text{C}$  MR spectroscopy of the brain for one patient.

The phantom measurements revealed that the RF head coil causes an overall attenuation of about  $+8.8\% \pm 0.38\%$ , reflecting the global attenuation caused by the RF head coil. The local differences across the phantom volume range from 1% up to 25%. The highest attenuation values were found in the lower region of RF coil close to the patient table where the head/neck support cradle attenuates photons the most. The open coil space near the upper birdcage rungs causes less attenuation in the upper regions of the phantom volume. The attenuation profile across the phantom volume as displayed on the resulting difference maps shows a rather homogeneous attenuation, reflecting the open birdcage design of the RF coil. Homogeneous and low-level attenuation of an RF coil can be seen as advantageous features and a precondition for subsequent attenuation correction [Quick 2014; Oehmigen et al. 2016; Paulus et al. 2016]. The overall attenuation caused by the RF head coil of 8.8% as measured in the phantom experiments can be considered as comparably low, when compared to the results of other studies. MacDonald et al. have determined the photon attenuation caused by a MR-only head RF coil to 20% [MacDonald et al. 2011]. Tellmann et al. in another study have investigated the attenuation caused by a dedicated PET/MR head RF coil. They have found an attenuation bias in the range of 13 - 19% [Tellmann et al. 2011]. The article by Paulus and Quick [Paulus et al. 2016] provides a comprehensive overview about numerous studies investigating the attenuation of several hardware components for use in PET/MR. No studies are available today specifically investigating dual-tuned RF head coils for PET/MR use.

Following attenuation correction by applying the CT-based AC template of the RF head coil, the phantom measurements revealed a measured difference across the phantom volume of  $0.96\% \pm 0.29\%$ , which is the measured difference between phantom measurement without RF coil and a second phantom measurement with RF coil and its attenuation correction. This rather low remaining quantification bias indicates successful

attenuation correction of the RF head coil and a successful implementation of the RF coil on the PET/MR system and in the PET data reconstruction process [Paulus et al. 2016].

The results of the patient measurements corroborate to a large extent the results of the phantom measurements. Anatomic MR images and PET images were all rated of high quality. Artefacts were neither observed in MR nor in PET images. Difference between a first set of PET measurements without RF coil and a second set of PET measurements with the RF coil in place showed a mean value of  $+5.1\% \pm 0.81\%$  for all six patients when no attenuation correction was applied. Following attenuation correction with the 3D RF head coil attenuation correction template, the mean difference between both measurements was reduced to difference values around  $-0.87\% \pm 0.65\%$ . As in the phantom experiments, this reduction of bias in the difference measurements indicates successful AC of the RF head coil. It has to be noted, however, that the difference maps in Figure 17 show local fluctuations (red and blue areas) due to short PET acquisition times (3 minutes) and a rather long delay between tracer injection and PET data acquisition (3 h 16 min post injection  $\pm 46$  min). A slight over-correction of the PET images can also be based on scatter correction for the  $\mu$ maps. Furthermore, two sequential patient measurements with and without the RF coil in place inevitably lead to a slight shift in the head position between the two measurements. For an accurate difference measurement, the two head scans need to be accurately coregistered.

The measurement of a non-selective  $^{13}\text{C}$  MR spectrum in a patient serves as a general demonstration that the dual-tuned RF head coil is also able to acquire  $^{13}\text{C}$  spectra with high signal-to-noise and sharp peak line-width. To unveil the full potential of PET/MR combined with  $^1\text{H}$  and  $^{13}\text{C}$  MRI/MRS in neuroimaging, however, further studies utilizing also  $^{13}\text{C}$  hyperpolarization are needed. The natural abundance of  $^{13}\text{C}$  is low; consequently, the SNR of  $^{13}\text{C}$  signal in MRI and MRS is rather low as well.  $^{13}\text{C}$  hyperpolarization can provide a strong boost of the  $^{13}\text{C}$  signal [Rodrigues et al. 2013; Cho et al. 2017; Månsson et al. 2006]. Thus, the full diagnostic potential for such a dual-tuned RF coil is provided in a setting where  $^{13}\text{C}$  hyperpolarization and a PET/MR system are available. This combination would allow for  $^1\text{H}$  high-resolution MRI and simultaneous PET/MR hybrid imaging in neuroimaging applications [Gordon et al. 2015]. In addition, the availability of hyperpolarized  $^{13}\text{C}$  MRI and MRS could provide important information on  $^{13}\text{C}$  tumour metabolism [Cho et al. 2017] adding important diagnostic information in neuro-oncologic applications.

Today, no dual-tuned RF head coil for PET/MR neuroimaging is available yet. In this context, the development of the dual-tuned RF head coil and the acquisition of a dedicated attenuation correction for this specific RF coil as presented in this study serves as an important step providing technical and methodological preconditions for multinuclear  $^{13}\text{C}/^1\text{H}$  PET/MR hybrid neuroimaging.

## **Conclusion**

A dual tuned  $^{13}\text{C}/^1\text{H}$  RF head coil was designed and evaluated regarding its potential use in integrated PET/MR hybrid imaging. An according CT-based attenuation correction template of the RF head coil was generated. Attenuation correction was evaluated in phantom experiments and in a patient study on six patients and provided accurate results for PET quantification. In conclusion, the dual-tuned RF head coil was successfully integrated into PET/MR hybrid imaging and can now be used for advanced  $^{13}\text{C}/^1\text{H}$  multinuclear hybrid neuroimaging in future studies.

## Discussion and Conclusion Study 3

A newly designed 16-channel RF breast array coil for integrated PET/MR imaging and staging of local breast cancer has been introduced. The RF coil design, hardware attenuation correction, PET/MR system implementation, and first clinical evaluation has been described in this work. The RF coil was designed for optimized MR imaging performance and maximized PET transparency. A dedicated 3D attenuation template model for the new RF breast coil was generated by CT imaging and subsequent conversion of the Hounsfield attenuation values to linear attenuation coefficients for PET. Automated attenuation correction of the hardware components was then implemented on an integrated PET/MR system (Siemens Biograph mMR) by using the 3D CT-based AC model of the RF coil during the PET reconstruction process. A repositioning frame ensures exact repositioning of the breast RF coil to exactly match its position on the PET/MR system table with the virtual position of the CT-based attenuation template model of the RF coil.

While attenuation correction of the patient tissues in PET/MR hybrid imaging is based on MR-sequences [Martinez-Möller et al. 2009; Quick 2014], the established method of choice for AC of hardware components, such as the systems patient table and various RF surface coils, is CT-based AC with using exact 3D template models of the hardware component to be corrected [Paulus et al. 2012; Quick 2014]. This method today can be considered as an established standard for most of the RF coils provided for all three vendors PET/MR systems [Zaidi et al. 2011; Delso et al. 2011; Grant et al. 2016; Quick 2014]. When additional RF coils or hardware components are to be integrated in PET/MR imaging, the following steps for CT-based template generation apply [Paulus et al. 2014; Paulus et al. 2016]. For generation of a CT-based AC model, the respective RF coil is scanned in a CT system; CT artefacts are removed by data masking and thresholding and the CT data is then smoothed by Gaussian filtering [Paulus et al. 2012; Kartmann et al. 2013]. In a next step, the AC values are converted from CT-based Hounsfield units (HU) to linear attenuation coefficients (LAC) of PET to match the energy level of attenuation from CT (140 keV) to PET (511 keV) [Paulus et al. 2013; Carney et al. 2006]. While the AC of patient tissues in PET/MR is MR-based, the described method for AC of hardware components in PET/MR hybrid imaging using CT-imaging is comparable to the method of AC in combined PET/CT systems [Carney et al. 2006].

A general precondition for 3D template-based AC of hardware components and RF coils is that the individual component to be corrected is rigid in its geometry and is stationary during the examination and that its position relative to the patient table is known [Quick 2014; Paulus et al. 2014; Paulus et al. 2016]. This precondition is fulfilled for the

patient tables, for the RF spine array coils, and for the RF head/neck coils in all three vendors PET/MR systems. With its rigid design, this precondition also is fulfilled for the accessory RF breast array coil that was designed and evaluated in this work. Exact repositioning of the RF coil, though, is another precondition for template model-based AC since the position of the RF coil and its attenuation template need to match for perfect AC. Otherwise, with shifted AC model and/or RF coil, local over- and under-correction will be the consequence when applying the AC model during the PET data reconstruction process [Paulus et al. 2012]. For this purpose, a positioning frame was designed in this study that ensures the exact repositioning of the breast RF coil on the PET/MR system table. The repositioning accuracy of the breast RF coil in this work was determined with MR-visible markers to better than 1 mm in all three spatial dimensions, which is considered sufficient to provide exact hardware component AC, given the 4 mm spatial resolution of PET imaging [Paulus et al. 2012; Kartmann et al. 2013; Paulus et al. 2014; Paulus et al. 2016].

As an alternative method for hardware component AC in PET/MR, the use of MR imaging with ultrashort echo time (UTE) sequences [Paulus et al. 2012] or the use of MR-visible markers [Kartmann et al. 2013] have been suggested. While UTE sequences have shown to provide rather insufficient imaging information and visualization for MR-based AC of RF coils [Paulus et al. 2012], MR-visible markers can only provide an indication of the position of an RF coil which then also would require an additional CT-model for AC to be matched to this position. Consequently, MR markers in this context only could provide an alternative to the positioning frame that ensures position match of RF coil and AC template model, not of the CT-based AC model itself [Kartmann et al. 2013].

Different groups [Delso et al. 2010; Tellmann et al. 2011; MacDonald et al. 2011; Paulus et al. 2012] have independently investigated the potential influence of RF head and surface RF body coils on PET signal attenuation. Results from these studies have shown that MR-only RF head coils attenuate the global count rate in PET data acquisition by up to 19 % [Delso et al. 2010; Tellmann et al. 2011; MacDonald et al. 2011], while the flexible surface RF body coils showed less but still non-negligible attenuation of PET signals in the range of 4 % - 10 % [Tellmann et al. 2011; Paulus et al. 2012; Kartmann et al. 2013]. All these studies have shown that the global attenuation value is only an average attenuation value, caused by the RF coils placed within the PET detector that can be further exceeded by higher local attenuation values close to the individual hardware components. All listed studies also discuss the use of CT-based  $\mu$ -maps for AC and demonstrate very good compensation of the hardware related attenuation for the RF head coils. Here, the rigid design and defined position of the RF coil relative to the patient table provide an ideal basis for CT-based AC [Delso et al. 2010; Tellmann et al. 2011; MacDonald et al. 2011].

Two previous studies have specifically investigated the use of dedicated RF coils and CT-based attenuation correction for local breast cancer lesion imaging in integrated PET/MR [Aklan et al. 2013; Dregerly et al. 2015]. While Aklan et al. introduced a 4-channel open design RF breast coil which was investigated to cause a global attenuation of 11 % when not applying AC [Aklan et al. 2013], Dregerly et al. investigated a prototype 16-channel RF breast coil that was designed to provide state-of-the-art 16-channel MR breast imaging performance during PET/MR hybrid imaging [Dregerly et al. 2015]. The RF coil in that study, however, was measured to cause a global attenuation of 22 % [26], reflecting the increased number of RF channels and associated components that potentially increase attenuation within the field-of-view of the PET detector when compared to the open-design 4-channel RF coil presented by Aklan [Aklan et al. 2013]. The further developed product 16-channel RF breast coil designed and evaluated in this present study was measured to provide a reduced global and mean value attenuation of only 13 % without applying attenuation correction. When compared to the global count attenuation biases reported above for other RF coil designs used in PET/MR hybrid imaging, e.g. head/neck RF coils causing 17 % [Aklan et al. 2013], 18 % [Tellmann et al. 2011], 19 % [MacDonald et al. 2011] of global attenuation, the 13 % level of global attenuation can be considered comparably small for a 16-channel RF breast coil with rigid housing that is designed to support the weight of a patient lying on top of the RF coil during imaging. Furthermore, the attenuation bias averaged across each transversal phantom slice and displayed along the z-direction as displayed in Figure 21 shows mean values for the bias within each slice in the range of 12-14 %, reflecting a rather homogeneous attenuation bias distribution. A low average global bias (12-14 %) and a homogeneous distribution across the imaging volume indicate a PET-transparent RF coil design by choice of materials and geometry. To achieve this goal, the design of the RF coil features large radii of the RF coil housing, low attenuating housing material, and electronic components and cables that are placed as much as possible outside of the FOV of the PET detector.

Local variation in phantom experiments was higher with an attenuation bias across the phantom volume ranging from 0 % in the middle of each phantom volume up to 24 % at the peripheral parts of the phantoms, when not applying attenuation correction. Following attenuation correction of the RF breast coil by applying the 3D CT-based AC model of the coil, the phantom evaluation confirmed very good correction with only small residual local bias across the breast phantoms ( $\pm 0.5$  %). The local and global attenuation bias across the imaging volumes of the RF breast coil, thus, could be successfully removed by applying the attenuation correction template for this RF coil, as shown in the phantom experiments (Fig. 22).

The phantom experiments, performed under controlled conditions, provide the range and spatial distribution of attenuation bias that can also be expected in PET/MR breast imaging of patients when using this specific RF breast coil. Different breast lesions at different locations within the breast will experience different amount of attenuation bias according to the range and spatial distribution of bias shown in the phantom experiments (i.e. 0 % to above 20 %) (Fig. 22). For each point in time (following radiotracer injection) and for each level of lesion activity in patient examinations using this RF coil we assume a percentage activity bias range and distribution as shown in the phantom experiments. Figure 22 in this context may be seen as a percentage bias “offset” across the breast imaging volume of this RF coil (for phantom and patient imaging) that can be set close to “zero” by using the generated CT-based AC template of this RF coil during attenuation correction. Consequently, the patient measurements without and with attenuation correction of the breast RF coil provided a mean difference value of  $SUV_{max}$  11.8 % averaged across all breast lesions, while the differences for individual breast lesions ranged from minimum 3.2 % to maximum 23.2 % (Table 6), indicating high agreement of phantom and patient measurements.

PET/MR hybrid imaging on patients with local breast cancer was successful in an initial series of ten patients and confirms all quantitative results and hybrid imaging aspects of the previous phantom measurements. In the patient study MR, PET, and PET/MR image quality was rated as excellent by two experienced readers. The RF coil provides homogeneous RF signal across the breast volumes. The bi-lateral multi-channel RF architecture allows for application of accelerated MR imaging protocols using parallel imaging with the GRAPPA method [Griswold et al. 2002]. All breast lesions were successfully detected and visualized with fine detail by MR and PET imaging (Figs. 25, 26). Quantitative measurements of  $SUV_{max}$  values in all  $^{18}F$ -FDG -active lesions without and with applying attenuation correction of the RF coil shows an increase of  $SUV_{max}$  when applying AC. This is well in the range of bias that was measured in the phantom experiments.

The number of ten patients for evaluation of the PET/MR imaging performance may be perceived as limitation of this study. However, the main focus of this study was the technical development of the RF coil, its appropriate CT-based template attenuation correction, PET/MR system implementation and systematic evaluation in controlled phantom experiments. The patient study in this context thus should be classified as first clinical proof of concept confirming the results of the phantom experiments and its clinical applicability on patients.

During the RF coil and attenuation template development process the e7 PET reconstruction tools provided by the PET/MR system vendor (Siemens) have been used for CT-based attenuation template generation and subsequent offline PET data reconstruction.

Following successful validation of the final 3D AC template for this RF breast coil in this study, PET data reconstruction with using the AC template was automated as it is standard for other RF coils on the currently available PET/MR systems by all three vendors. To achieve this, the final 3D AC template was loaded into the PET/MR system reconstruction computer and is automatically considered during PET data reconstruction whenever the RF coil plugs of the breast RF coil are connected to the PET/MR system table.

## **Conclusion**

The 16-channel RF breast coil and its attenuation correction are now tested for clinical use and can be applied in future clinical routine or research studies using PET/MR hybrid imaging for local breast tumor staging. The setting developed in this work can be seen as an advance since it provides the groundwork for high quality MR and PET imaging and, furthermore, exact PET activity quantification in PET/MR breast cancer lesion imaging.

# Summary

The combined positron-emission-tomography (PET) and magnet resonance (MR) imaging, called PET/MR hybrid imaging, conjuncts the advantages of both imaging modalities. It combines the specific metabolic information of PET with the high spatial resolution anatomical and functional images of MRI. A fundamental physical and technical challenge of PET/MR hybrid imaging is the attenuation correction (AC) of PET data. It is a prerequisite for artifact-free PET image quality and for an accurate PET quantification. The aim of this thesis was to develop and evaluate new AC methods for different clinical applications in PET/MR hybrid imaging.

In the first part of the thesis a new method for AC of patient tissues was systematically evaluated on n=50 PET/MR patients. Altogether 99 lesions were detected and the standardized uptake values (SUV) were determined. By applying the new AC methods, the measured mean SUV increased by 4.4 %. For lesions located near to bone structures, an increase of SUV of up to 35 % could be measured.

In the second study, a dual-tuned RF head coil for C<sup>13</sup> and H<sup>1</sup> PET/MR neuroimaging was investigated, and a CT-based 3D AC model of the radiofrequency (RF) coil was generated. Phantom experiments showed that the RF coil caused an overall attenuation of 9 % of the PET signal. By applying the AC model, the measured PET attenuation could be decreased to 0.5 % and could be validated by a patient study.

In the third study of the thesis, a 16-channel RF breast coil was optimized for PET/MR hybrid imaging and an according CT-based 3D AC model of the RF breast coil was generated. In phantom experiments, the RF breast coil caused an overall attenuation of 13 % of the PET signal. By applying the AC model, the measured PET signal loss decreased to 0.5 %, which was also validated in a patient study.

The methods developed and evaluated in this thesis lead to an improvement of attenuation correction and, furthermore, to an expansion of the diagnostic application spectrum of PET/MR hybrid imaging.

# Zusammenfassung

Die kombinierte Positron-Emissions-Tomographie (PET) und Magnetresonanztomographie (MRT), kurz PET/MR-Hybridbildgebung, vereint synergistisch die Vorteile beider bildgebenden Modalitäten. Sie kombiniert die hochspezifischen Stoffwechsellinformationen des PET mit hoch aufgelöster anatomischer und funktioneller Bildinformation des MRT. Eine grundlegende physikalisch/technische Herausforderung bei der PET/MR-Hybridbildgebung ist die Schwächungskorrektur (AC) von PET-Daten. Diese ist eine Voraussetzung für artefaktfreie PET-Bildqualität und für die akkurate Quantifizierung mittels PET. Das Ziel dieser Arbeit war es, neue AC-Methoden für verschiedene klinische Anwendungen in der PET/MR-Hybridbildgebung zu entwickeln und zu evaluieren.

Im ersten Teil der Arbeit wurde eine neue Methode zur AC von Patientengeweben an n=50 PET/MR-Patienten systematisch evaluiert. Es wurden insgesamt 99 Läsionen detektiert und deren Aktivität bestimmt (standardized uptake value, SUV). Durch die Verwendung der neuen AC-Methode stieg der gemessene durchschnittliche SUV-Wert, gemittelt über alle 99 Läsionen, um 4,4 % an. Für knochen nahe Tumore und Läsionen konnte ein Anstieg des SUV-Wertes von bis zu 35 % gemessen werden.

In der zweiten Studie wurde eine Zwei-Kern Hochfrequenz (HF)-Kopfspule für die C<sup>13</sup>- und H<sup>1</sup>-PET/MR-Neurobildgebung untersucht und es wurde ein CT-basiertes 3D AC-Modell für diese HF-Kopfspule erstellt. In Phantomexperimenten verursachte die HF-Spule eine globale Schwächung von PET-Signalen von 9 %. Durch Verwendung des AC-Modells konnte die gemessene PET-Signalschwächung auf 0,5 % reduziert und in einer Patientenstudie validiert werden.

In der dritten Studie wurde eine 16-Kanal HF-Brustspule für die PET/MR-Hybridbildgebung optimiert und es wurde ebenfalls ein CT-basiertes 3D AC-Modell für diese HF-Brustspule erstellt. In Phantommessungen verursachte die HF-Brustspule einen globalen PET-Signalverlust von 13 %. Durch Verwendung des AC-Modells konnte die gemessene PET-Signalschwächung auf 0,5 % reduziert und ebenfalls in einer Patientenstudie validiert werden.

Die entwickelten und evaluierten Methoden dieser Arbeit dienen jeweils der Verbesserung der Schwächungskorrektur und damit der Erweiterung des diagnostischen Einsatzspektrums der PET/MR-Hybridbildgebung.

# References

1. Aklan B, Paulus DH, Wenkel E, Braun H, Navalpakkam BK, Ziegler S, Geppert C, Sigmund EE, Melsaether A, Quick HH. (2013):  
Toward simultaneous PET/MR breast imaging: Systematic evaluation and integration of a radiofrequency breast coil. *Med Phys.* 2013;40:024301.
2. Allisy-Roberts PJ, Williams J. Farr's (2008):  
*Physics for Medical Imaging*. 2nd ed. Saunders Elsevier; 2008: 9.
3. Bailey DL, Antoch G, Bartenstein P, Barthel H, Beer AJ, Bisdas S, Bluemke DA, Boellaard R, Claussen CD, Franzius C, Hacker M, Hricak H, la Fougère C, Gückel B, Nekolla SG, Pichler BJ, Purz S, Quick HH, Sabri O, Sattler B, Schäfer J, Schmidt H, van den Hoff J, Voss S, Weber W, Wehrl HF, Beyer T. (2015):  
Combined PET/MR: The Real Work Has Just Started. Summary Report of the Third International Workshop on PET/MR Imaging; February 17-21, 2014, Tübingen, Germany. *Mol Imaging Biol.* 2015;17:297-312.
4. Bailey DL, Pichler BJ, Gückel B, Barthel H, Beer AJ, Bremerich J, Czernin J, Drzezga A, Franzius C, Goh V, Hartenbach M, Iida H, Kjaer A, la Fougère C, Ladefoged CN, Law I, Nikolaou K, Quick HH, Sabri O, Schäfer J, Schäfers M, Wehrl HF, Beyer T. (2015):  
Combined PET/MR: Multi-modality Multi-parametric Imaging Is Here: Summary Report of the 4th International Workshop on PET/MR Imaging; February 23-27, 2015, Tübingen, Germany. *Mol Imaging Biol.* 2015;17(5):595-608.
5. Bal G, Kehren F, Michel C, Watson C, Manthey D, Nuyts J. (2011):  
Clinical evaluation of MLAA for MR-PET. *J Nucl Med* May 2011 vol. 52 no. supplement 1 263.
6. Beyer T, Lassen ML, Boellaard R, Delso G, Yaqub M, Sattler B, Quick HH. (2016):  
Investigating the state-of-the-art in whole-body MR-based attenuation correction: an intra-individual, inter-system, inventory study on three clinical PET/MR systems. *MAGMA.* 2016 Feb;29(1):75-87.
7. Beyer T, Townsend DW, Brun T, Kinahan PE, Charron M, Roddy R, Jerin J, Young J, Byars L, Nutt R. (2000):  
A combined PET/CT scanner for clinical oncology. *J Nucl Med.* 2000 Aug;41(8):1369-1379.
8. Beyer T, Weigert M, Quick HH, Pietrzyk U, Vogt F, Palm C, Antoch G, Müller SP, Bockisch A. (2008):  
MR-based attenuation correction for torso-PET/MR imaging: pitfalls in mapping MR to CT data. *Eur J Nucl Med Mol Imaging.* 2008 Jun;35(6):1142-1146.
9. Bezrukov I, Schmidt H, Mantlik F, Schwenzler N, Brendle C, Schölkopf B, Pichler BJ. (2013):  
MR-based attenuation correction methods for improved PET quantification in lesions within bone and susceptibility artifact regions. *J Nucl Med.* 2013 Oct;54(10):1768-1774.
10. Blumhagen JO, Braun H, Ladebeck R, Fenchel M, Faul D, Scheffler K, Quick HH. (2014):  
Field of view extension and truncation correction for MR-based human attenuation correction in simultaneous MR/PET imaging. *Med Phys.* 2014 Feb;41(2):022303.
11. Blumhagen JO, Ralf Ladebeck R, Fenchel M, Scheffler K. (2013):  
MR-Based Field-of-View Extension in MR/PET: B0 Homogenization Using Gradient Enhancement (HUGE). *Magn Reson Med.* 2013 Oct;70(4):1047-1057.
12. Boellaard R, Quick HH. (2015):  
Current Image Acquisition Options in PET/MR. *Semin Nucl Med.* 2015 May;45(3):192-200.
13. Boellaard R, Rausch I, Beyer T, Delso G, Yaqub M, Quick HH, Sattler B. (2015):  
Quality control for quantitative multicenter whole-body PET/MR studies: A NEMA image quality phantom study with three current PET/MR systems. *Med Phys.* 2015 Oct;42(10):5961-5969.
14. Breuer FA, Blaimer M, Heidemann RM, Mueller MF, Griswold MA, Jakob PM. (2005):  
Controlled aliasing in parallel imaging results in higher acceleration (CAIPIRINHA) for multi-slice imaging. *Magn Reson Med.* 2005 Mar;53(3):684-691.

15. Buck AK, Reske SN. (2004):  
Cellular origin and molecular mechanisms of 18F-FDG uptake: is there a contribution of the endothelium?  
J Nucl Med. 2004 Mar;45(3):461-463
16. Cairns RA, Harris IS, Mak TW. (2011):  
Regulation of cancer cell metabolism. Nat Rev Cancer. 2011 Feb;11(2):85-95
17. Carney JP, Townsend DW, Rappoport V, Bendriem B. (2006):  
Method for transforming CT images for attenuation correction in PET/CT imaging. Med Phys. 2006;33:976-983.
18. Catalano OA, Nicolai E, Rosen BR, Luongo A, Catalano M, Iannace C, Guimaraes A, Vangel MG, Mahmood U, Soricelli A, Salvatore M. (2015):  
Comparison of CE-FDG-PET/CT with CE-FDG-PET/MR in the evaluation of osseous metastases in breast cancer patients. Br J Cancer. 2015 Apr 28;112(9):1452-60.
19. Catana C, Wu Y, Judenhofer MS, Qi J, Pichler BJ, Cherry SR. (2006):  
Simultaneous acquisition of multislice PET and MR images: initial results with a MR-compatible PET scanner. J Nucl Med. 2006 Dec;47(12):1968-1976.
20. Cho A, Lau JYC, Geraghty BJ, Cunningham CH, Keshari KR. (2017):  
Noninvasive Interrogation of Cancer Metabolism with Hyperpolarized 13C MRI. J Nucl Med. 2017 Aug;58(8):1201-1206.
21. Delso G, Fürst S, Jakoby B, Ladebeck R, Ganter C, Nekolla SG, Schwaiger M, Ziegler SI. (2011):  
Performance measurements of the Siemens mMR integrated whole-body PET/MR scanner. J Nucl Med. 2011;52:1914-1922.
22. Delso G, Fürst S, Jakoby B, Ladebeck R, Ganter C, Nekolla SG, Schwaiger M, Ziegler SI. (2010):  
Evaluation of the attenuation properties of MR equipment for its use in a whole-body PET/MR scanner. Phys Med Biol. 2010 Aug 7;55(15):4361-4374.
23. Delso G, Martinez-Möller A, Bundschuh RA, Nekolla SG, Ziegler SI. (2010):  
The effect of limited MR field of view in MR/PET attenuation correction. Med Phys. 2010 Jun;37(6):2804-2812.
24. Delso G, Wiesinger F, Sacolick LI, Kaushik SS, Shanbhag DD, Hüllner M, Veit-Haibach P. (2015):  
Clinical evaluation of zero-echo-time MR imaging for the segmentation of the skull. J Nucl Med. 2015 Mar;56(3):417-422.
25. Dietrich O, Raya JG, Reeder SB, Reiser MF, Schoenberg SO. (2007):  
Measurement of signal-to-noise ratios in MR images: influence of multichannel coils, parallel imaging, and reconstruction filters. J Magn Reson Imaging. 2007 ;26:375-385.
26. Dregely I, Lanz T, Metz S, Mueller MF, Kuschan M, Nimbalkar M, Bundschuh RA, Ziegler SI, Haase A, Nekolla SG, Schwaiger M. (2015):  
A 16-channel MR coil for simultaneous PET/MR imaging in breast cancer. Eur Radiol. 2015;25:1154-1161.
27. Drzezga A, Souvatzoglou M, Eiber M, Beer AJ, Fürst S, Martinez-Möller A, Nekolla SG, Ziegler S, Ganter C, Rummeny EJ, Schwaiger M. (2012):  
First clinical experience with integrated whole-body PET/MR: comparison to PET/CT in patients with oncologic diagnoses. J Nucl Med. 2012 Jun;53(6):845-855.
28. Gordon JW, Fain SB, Niles DJ, Ludwig KD, Johnson KM, Peterson ET. (2015):  
Simultaneous imaging of 13C metabolism and 1H structure: technical considerations and potential applications. NMR Biomed. 2015 May;28(5):576-582.
29. Grant AM, Deller TW, Khalighi MM, Maramraju SH, Delso G, Levin CS. (2016):  
NEMA NU 2-2012 performance studies for the SiPM-based ToF-PET component of the GE SIGNA PET/MR system. Med Phys. 2016 May;43(5):2334.
30. Griswold MA, Jakob PM, Heidemann RM. (2002):  
Generalized Autocalibrating Partially Parallel Acquisitions (GRAPPA). Magn Reson Med. 2002;47:1202-1210.
31. Grueneisen J, Nagarajah J, Buchbender C, Hoffmann O, Schaarschmidt BM, Poeppel T, Forsting M, Quick HH, Umutlu L, Kinner S. (2015):

- Positron Emission Tomography/Magnetic Resonance Imaging for Local Tumor Staging in Patients With Primary Breast Cancer: A Comparison With Positron Emission Tomography/Computed Tomography and Magnetic Resonance Imaging. *Invest Radiol.* 2015;50:505-513.
32. Haacke EM, Brown RW, Thompson MR, Venkatesan R. (1999):  
Magnetic resonance imaging: physical principles and sequence design. Wiley-Liss, New York, 1999
  33. Hansen AE, Andersen FL, Henriksen ST, Vignaud A, Ardenkjaer-Larsen JH, Højgaard L, Kjaer A, Klausen TL. (2016):  
Simultaneous PET/MRI with <sup>13</sup>C magnetic resonance spectroscopic imaging (hyperPET): phantom-based evaluation of PET quantification. *EJNMMI Phys.* 2016 Dec;3(1):7.
  34. Hendee WR, Ritenour ER. (2002):  
Medical Imaging in Physics. 4<sup>th</sup> ed. New York: Wiley-Liss; 2002
  35. Herzog H, Langen KJ, Weirich C, Rota Kops E, Kaffanke J, Tellmann L, Scheins J, Neuner I, Stoffels G, Fischer K, Caldeira L, Coenen HH, Shah NJ. (2011):  
High resolution Brain PET combined with simultaneous MRI. *Nuklearmedizin.* 2011;50(2):74-82.
  36. Hofmann M, Bezrukov I, Mantlik F, Aschoff P, Steinke F, Beyer T, Pichler BJ, Schölkopf B. (2011):  
MRI-based attenuation correction for whole-body PET/MRI: quantitative evaluation of segmentation- and atlas-based methods. *J Nucl Med.* 2011 Sep;52(9):1392-1399.
  37. Iagaru A, Mittra E, Minamimoto R, Jamali M, Levin C, Quon A, Gold G, Herfkens R, Vasanawala S, Gambhir SS, Zaharchuk G. (2015):  
Simultaneous whole-body time-of-flight 18F-FDG PET/MRI: a pilot study comparing SUVmax with PET/CT and assessment of MR image quality. *Clin Nucl Med.* 2015; 40:1-8.
  38. Kartmann R, Paulus DH, Braun H, Aklan B, Ziegler S, Navalpakkam BK, Lentschig M, Quick HH. (2013):  
Integrated PET/MR imaging: automatic attenuation correction of flexible RF coils. *Med Phys.* 2013 Aug;40(8):082301
  39. Keereman V, Fierens Y, Broux T, De Deene Y, Lonneux M, Vandenberghe S. (2010):  
MRI-based attenuation correction for PET/MRI using ultrashort echo time sequences. *J Nucl Med* 2010;51:812–818.
  40. Keereman V, Mollet P, Berker Y, Schulz V, Vandenberghe S. (2013):  
Challenges and current methods for attenuation correction in PET/MR. *MAGMA.* 2013 Feb;26(1):81-98.
  41. Kinahan PE, Hasegawa BH, Beyer T. (2003):  
X-Ray-Based Attenuation Correction for Positron Emission Tomography/Computed Tomography Scanners. *Semin Nucl Med.* 2003; 33:166–179.
  42. Kinahan PE, Townsend DW, Beyer T, Sashin D. (1998):  
Attenuation correction for a combined 3D PET/CT scanner. *Med Phys.* 1998 Oct;25(10):2046-2053.
  43. Koesters T, Friedman KP, Fenchel M, Zhan Y, Hermosillo G, Babb J, Jelescu IO, Faul D, Boada FE, Shepherd TM. (2016):  
Dixon Sequence with Superimposed Model-Based Bone Compartment Provides Highly Accurate PET/MR Attenuation Correction of the Brain. *J Nucl Med.* 2016 Jun;57(6):918-924.
  44. Kuwert T, Bockisch A. (2008):  
*Nuklearmedizin, 4., neu erstellte und erw. Aufl.* Thieme Verlag ,Stuttgart, 2008
  45. Larsson A, Johansson A, Axelsson J, Nyholm T, Asklund T, Riklund K, Karlsson M. (2013):  
Evaluation of an attenuation correction method for PET/MR imaging of the head based on substitute CT images. *MAGMA.* 2013 Feb;26(1):127-36.
  46. Lindemann ME, Oehmigen M, Blumhagen JO, Gratz M, Quick HH. (2017):  
MR-based truncation and attenuation correction in integrated PET/MR hybrid imaging using HUGE with continuous table motion. *Med Phys.* 2017 Sep;44(9):4559-4572.
  47. MacDonald LR, Kohlmyer S, Liu C, Lewellen TK, Kinahan PE. (2011):  
Effects of MR surface coils on PET quantification. *Med Phys.* 2011;38:2948-2956.

48. Månsson S, Johansson E, Magnusson P, Chai CM, Hansson G, Petersson JS, Ståhlberg F, Golman K. (2006):  
13C imaging-a new diagnostic platform. *Eur Radiol.* 2006 Jan;16(1):57-67.
49. Martinez-Möller A, Souvatzoglou M, Delso G, Bundschuh RA, Chefd'hotel C, Ziegler SI, Navab N, Schwaiger M, Nekolla SG. (2009):  
Tissue classification as a potential approach for attenuation correction in whole-body PET/MRI: evaluation with PET/CT data. *J Nucl Med.* 2009;50:520–526.
50. Colm McGinnity, Radhouene Neji, Jane MacKewn, James Stirling, Sami Jeljeli, Titus Lanz, Christian Geppert, Mark Oehmigen, Harald Quick, Gary Cook, Alexander Hammers (2016):  
In-vivo Simultaneous Brain 18F FDG PET Imaging and 13C MR Spectroscopy: Initial Experience. *Proc. Intl. Soc. Mag. Reson. Med.* 24 (2016).
51. Mayer-Kuckuk T. (1994)  
Kernphysik Eine Einführung. V6. Aufl. Vieweg+Teubner Verlag, 1994
52. Navalpakkam BK, Braun H, Kuwert T, Quick HH. (2013):  
Magnetic resonance-based attenuation correction for PET/MR hybrid imaging using continuous valued attenuation maps. *Invest Radiol.* 2013 May;48(5):323-332.
53. Nuyts J, Bal G, Kehren F, Fenchel M, Michel C, Watson C. (2013):  
Completion of a truncated attenuation image from the attenuated PET emission data. *IEEE Trans Med Imaging.* 2013 Feb;32(2):237-46.
54. Oehmigen M, Lindemann ME, Lanz T, Kinner S, Quick HH. (2016):  
Integrated PET/MR breast cancer imaging: Attenuation correction and implementation of a 16-channel RF coil. *Med Phys.* 2016 Aug;43(8):4808.
55. Paulus DH, Braun H, Aklan B, Quick HH. (2012):  
Simultaneous PET/MR imaging: MR-based attenuation correction of local radiofrequency surface coils. *Med Phys.* 2012; 39:4306-4315.
56. Paulus DH, Oehmigen M, Grüneisen J, Umutlu L, Quick HH. (2016):  
Whole-body hybrid imaging concept for the integration of PET/MR into radiation therapy treatment planning. *Phys Med Biol.* 2016 May 7;61(9):3504-3520.
57. Paulus DH, Quick HH, Geppert C, Fenchel M, Zhan Y, Hermsillo G, Faul D, Boada F, Friedman KP, Koesters T. (2015):  
Whole-Body PET/MR Imaging: Quantitative Evaluation of a Novel Model-Based MR Attenuation Correction Method Including Bone. *J Nucl Med.* 2015;56:1061-1066.
58. Paulus DH, Quick HH. (2016):  
Hybrid Positron Emission Tomography/Magnetic Resonance Imaging: Challenges, Methods, and State of the Art of Hardware Component Attenuation Correction. *Invest Radiol.* 2016 Oct;51(10):624-634.
59. Paulus DH, Tellmann L, Quick HH. (2013):  
Towards improved hardware component attenuation correction in PET/MR hybrid imaging. *Phys Med Biol.* 2013;58:8021-8040.
60. Paulus DH, Thorwarth D, Schmidt H, Quick HH. (2014):  
Towards integration of PET/MR hybrid imaging into radiation therapy treatment planning. *Med Phys.* 2014 Jul;41(7):072505.
61. Pichler, BJ, Judenhofer MS, Catana C, Walton JH, Kneilling M, Nutt RE, Siegel SB, Claussen CD, Cherry SR. (2006):  
Performance test of an LSO-APD detector in a 7-T MRI scanner for simultaneous PET/MRI. *J Nucl Med.* 2006 Apr;47(4):639-647.
62. Phelps, ME, Cherry SR, Dahlbom M. (2004):  
PET: Physics, instrumentation, and scanners. Springer New York.
63. Pujara AC, Raad RA, Ponzio F, Wassong C, Babb JS, Moy L, Melsaether AN. (2016):  
Standardized Uptake Values from PET/MRI in Metastatic Breast Cancer: An Organ-based Comparison With PET/CT. *Breast J.* 2016 May;22(3):264-273.

64. Quick HH, Ladebeck R, Georgi JC. (2011):  
Whole-body MR/PET hybrid imaging: Technical considerations, clinical workflow, and initial results,"  
MAGNETOM Flash. Pp 88-100 (2011).
65. Quick HH, von Gall C, Zeilinger M, Wiesmüller M, Braun H, Ziegler S, Kuwert T, Uder M, Dörfler A,  
Kalender WA, Lell M. (2013):  
Integrated whole-body PET/MR hybrid imaging: clinical experience. *Invest Radiol.* 2013;48:280-289.
66. Quick HH. (2014):  
Integrated PET/MR. *J Magn Reson Imaging.* 2014;39:243-258.
67. Rausch I, Rischka L, Ladefoged CN, Furtner J, Fenchel M, Hahn A, Lanzenberger R, Mayerhoefer ME,  
Traub-Weidinger T, Beyer T. (2017):  
PET/MRI for oncological brain imaging: A comparison of standard MR-based attenuation corrections with a  
novel, model-based approach for the Siemens mMR PET/MR system. *J Nucl Med.* 2017 Mar 2. pii:  
jnumed.116.186148.
68. Rodrigues TB, Valette J, Bouzier-Sore AK. (2013):  
(13)C NMR spectroscopy applications to brain energy metabolism. *Front Neuroenergetics.* 2013 Dec  
9;5:9.
69. Samarin A, Burger C, Wollenweber SD, Crook DW, Burger IA, Schmid DT, von Schulthess GK, Kuhn FP.  
(2012):  
PET/MR imaging of bone lesions – implications for PET quantification from imperfect attenuation  
correction. *Eur J Nucl Med Mol Imaging.* 2012 Jul;39(7):1154-1160.
70. Sawicki LM, Grueneisen J, Schaarschmidt BM, Buchbender C, Nagarajah J, Umutlu L, Antoch G, Kinner  
S. (2016):  
Evaluation of (18)F-FDG PET/MRI, (18)F-FDG PET/CT, MRI, and CT in whole-body staging of recurrent  
breast cancer. *Eur J Radiol.* 2016 Feb;85(2):459-65.
71. Schlemmer HPW, Pichler BJ, Schmand M, Burbar Z, Michel C, Ladebeck R, Jattke K, Townsend D,  
Nahmias C, Jacob PK, Heiss WD, Claussen CD. (2008):  
Simultaneous MR/PET imaging of the human brain: feasibility study. *Radiology* 2008; 248: 1028–1035.
72. Schulz V, Torres-Espallardo I, Renisch S, Hu Z, Ojha N, Börner P, Perkuhn M, Niendorf T, Schäfer WM,  
Brockmann H, Krohn T, Buhl A, Günther RW, Mottaghy FM, Krombach GA. (2011):  
Automatic, three-segment, MR-based attenuation correction for whole-body PET/MR data. *Eur J Nucl Med  
Mol Imaging.* 2011 Jan;38(1):138-152.
73. Tabouret-Viaud C, Botsikas D, Delattre BM, Mainta I, Amzalag G, Rager O, Vinh-Hung V, Miralbell R,  
Ratib O. (2015):  
PET/MR in Breast Cancer. *Semin Nucl Med.* 2015 Jul;45(4):304-321.
74. Taneja S, Jena A, Goel R, Sarin R, Kaul S. (2014):  
Simultaneous whole-body 18F-FDG PET-MRI in primary staging of breast cancer: A pilot study. *Eur J  
Radiol.* 2014 ;83:2231-2239
75. Tellmann L, Quick HH, Bockisch A, Herzog H, Beyer T. (2011):  
The effect of MR surface coils on PET quantification in whole-body PET/MR: Results from a pseudo-  
PET/MR phantom study. *Med Phys.* 2011;38:2795-2805.
76. Townsend DW. (2004):  
Physical principles and technology of clinical PET imaging. *Ann Acad Med Singapore.* 2004  
Mar;33(2):133-145.
77. Veit-Haibach P, Kuhn FP, Wiesinger F, Delso G, von Schuckthess G (2013):  
PET-MR imaging using a tri-modality PET/CT-MR system with a dedicated shuttle in clinical routine. *Magn  
Reson Mater Physics, Biol Med.* 2013;26(1):25-35
78. Widmaier S, Breuer J, Jung WI, Dietze GJ, Lutz O. (1998):  
31P/1H WALTZ-4 broadband decoupling at 1.5 T: different versions of the composite pulse and  
consequences when using a surface coil. *Magn Reson Imaging.* 1998 Sep;16(7):845-849.
79. Wiesmüller M, Quick HH, Navalpakkam B, Lell MM, Uder M, Ritt P, Schmidt D, Beck M, Kuwert T, von Gall  
CC. (2013):

Comparison of lesion detection and quantitation of tracer uptake between PET from a simultaneously acquiring whole-body PET/MR hybrid scanner and PET from PET/CT. *EJNMMI*. 2013 Jan;40(1):12-21.

80. Zaidi, H. (2007):  
Is MR-guided attenuation correction a viable option for dual-modality PET/MR imaging? *Radiology*. 2007 Sep;244(3):639-642.
81. Zaidi H, Ojha N, Morich M, Griesmer J, Hu Z, Maniawski P, Ratib O, Izquierdo-Garcia D, Fayad ZA, Shao L. (2011):  
Design and performance evaluation of a whole-body Ingenuity TF PET-MRI system. *Phys Med Biol*. 2011;21:3091–3106.
82. Ziegler S, Braun H, Ritt P, Hocke C, Kuwert T, Quick HH. (2013):  
Systematic evaluation of phantom fluids for simultaneous PET/MR hybrid imaging. *J Nucl Med*. 2013 Aug;54(8):1464-1471.
83. Ziegler S, Jakoby BW, Braun H, Paulus DH, Quick HH. (2015):  
NEMA image quality phantom measurements and attenuation correction in integrated PET/MR hybrid imaging. *EJNMMI Phys*. 2015 Dec;2(1):18.

## List of abbreviation

13C	13-Carbon	MRS	magnetic resonance spectroscopy
<sup>18</sup> F	18-Fluor	NAC	non attenuation corrected
<sup>18</sup> F-FDG	18-Fluorodesoxyglucose	NMR	nuclear magnetic resonance
1H	1-Hydrogen or proton	OP-OSEM	ordinary poisson ordered-subset expectation maximization
3D	three dimensional	PA	polyamide
3T / 7T	3 tesla / 7 tesla	PC	polycarbonate
<sup>68</sup> Ge/ <sup>68</sup> Ga	Germanium-68/ Gallium-68	PET	positron emission tomography
ABS	acrylonitrile-butadiene-styrene	PET/CT	positron emission tomography / computed tomography
AC	attenuation correction	PET/MR	positron emission tomography / magnetic resonance
APD	avalanche photo diode	PD	proton density
B <sub>0</sub>	static magnetic field	PMMA	polymethyl methacrylate
B <sub>1</sub>	magnetic field	PMT	photomultiplier tube
BGO	bismuth germanium oxide	POM	polyoxymethylene
BMI	body mass index	PS	polystyrene
Bq	Becquerel	PUR	polyurethane
Bq/ml	Becquerel per milliliter	PVC	polyvinyl chloride
CAD	Computer aided design	RF	radiofrequency
CNR	contrast to noise ratio	ROI	region of interest
CT	computed tomography	SD	standard deviation
EQ	equation	SNR	signal to noise ratio
FDG	fluorodeoxyglucose	SPECT	single photon emission computed tomography
FID	free induction decay	SUV	standardized uptake value
FLASH	fast low-angle shot	SUV <sub>max</sub>	maximal standardized uptake value
FoV	field of view	SUV <sub>mean</sub>	mean standardized uptake value
GRAPPA	generalized auto calibrating partial parallel acquisition	T1	spin-lattice relaxation time
GRE	gradient echo	T2	spin-spin relaxation time
HU	Hounsfield units	T2*	effective spin-spin relaxation
HUGE	homogenization using gradient enhancement	TE	echo time
keV	kilo electronvolt	TIRM	turbo inversion recovery magnitude
LAC	linear attenuation coefficient	TR	repetition time
LOR	line of response	TSE	turbo spin echo
LSO	lutetium oxyorthosilicate	μmap	attenuation correction map
mA	milliampere	UTE	ultrashort echo time
MBq	mega Becquerel	VIBE	volumetric interpolated breath-hold examination
MeV	mega electronvolt	VOI	volume of interest
MLAA	maximum likelihood estimation of activity and attenuation	WALTZ	wideband alternating-phase low-power technique for zero-residual splitting
MR	magnetic resonance	ZTE	zero echo time
MRI	magnet resonance imaging		

## Acknowledgments

First and foremost, I would like to thank Prof. Dr. rer. medic. Harald H. Quick. Since 2009, when I met him at the Erwin L. Hahn Institute for MRI, he was my supervisor for my Bachelor thesis, he gave me the opportunity to work as a PhD student and he showed me the exciting field of PET/MR hybrid imaging. I would like to thank him for his perpetual guidance, his constant support and readiness to help and discuss any matter with me.

I also like to thank the High Field and Hybrid MR Imaging group. Most notably is my colleague Maike Lindemann, who was my office buddy, my desk neighbor and my steady discussion partner.

I would like to thank the Department of Nuclear Medicine and the Department of Diagnostic and Interventional Radiology and Neuroradiology, University Hospital Essen, especially the radiographer team, who never were tired to help me with my measurements and experiments.

Thanks to our collaboration partner, Siemens Healthcare and Rapid Biomedical GmbH, with Dr. Titus Lanz. Thank you for the technical support, launching of new ideas, the good cooperation and the possibility to work and improve PET/MR imaging.

Last but not least, I would like to thank my friends and my family, particularly my parents and my sister, for supporting and guiding me through the years of developing this thesis. My special thanks go to my beloved wife Laura, who was always patient with me, supported me in every aspect and kept on encouraging me through the years. Her contribution helped me to finish this thesis.

## **Curriculum Vitae**

Der Lebenslauf ist in der Online-Version aus Gründen des Datenschutzes nicht enthalten.